Analysis of Background Light with the Optical Ground Station Oberpfaffenhofen for Satellite QKD Scenarios

Florian Tobias Schümann

Date of Submission:

29.06.2026

Referees:

Florian Moll, M. Sc.
Institute of Communications and Navigations
German Aerospace Center (DLR)

Prof. Dr. Michèle Heurs
Institute of Gravitational Physics
Leibniz University Hannover

Supervisor:

Stefanie Häusler, M. Sc.
Institute of Communications and Navigations
German Aerospace Center (DLR)

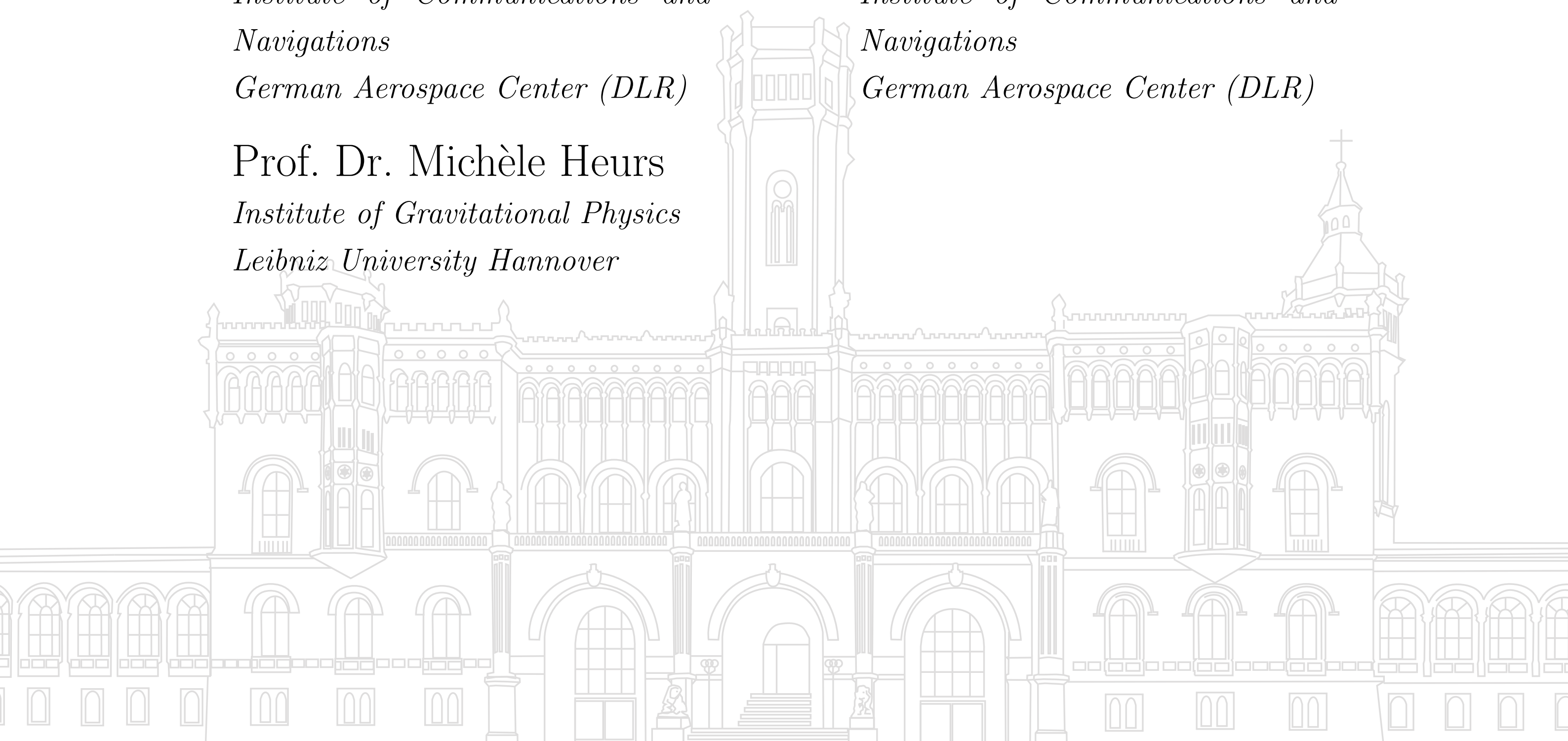

Diese Arbeit ist meinen Eltern gewidmet, die mir dies alles ermöglicht haben.

Declaration of authorship

I, Florian Tobias Schümann, hereby affirm on oath, that this thesis is my own unaided work. I have not adopted passages from other third parties without attribution and have indicated all the resources and sources used in my work. This thesis, in its current or similar form, has not been submitted to any other examination office.

Date

Signature

Abstract

Quantum key distribution (QKD) allows secure data transfer in a post-quantum era by exploiting the laws of quantum mechanics to generate a secure-key for data encryption. Satellite based QKD is the gateway to a global communication network due to its quadratic transmission loss scaling opposed to the exponential losses in fiber-based QKD. However, the free-space nature of satellite QKD imposes a new challenge due to the additional noise source of background light (BGL). BGL heavily influences the feasibility of a secure QKD protocol, and its impact has to be mitigated through temporal, spatial and spectral filtering techniques. To design optical systems for satellite QKD, the contributions of BGL must be characterized, but current observations of BGL in the C-band are limited to daytime measurements with collimator setups. These measurements are only translated to the receiving systems of QKD downlinks, Optical Ground Stations (OGSs), via theoretical models. This work presents an optical setup built and calibrated for BGL measurements in the C-band with single mode fiber (SMF) coupling during the day and night utilizing the Optical Ground Station Oberpfaffenhofen (OGSOP) designed for satellite QKD downlinks. The transmission loss of the optical system and the efficiency of the deployed Superconducting Nanowire Single Photon Detector (SNSPD) are determined and BGL measurement data in the C-band acquired during the day and night. In addition the measured BGL is compared with BGL simulations and prior measurements with collimator setups for verification. During the night, the measured BGL only raises slightly above the noise floor of the detector with larger radiances observed only close to the surface with up to $0.00023\,\mathrm{mW\,nm^{-1}\,m^{-2}\,sr^{-1}}$ and close to the full Moon with up to $0.0043\,\mathrm{mW\,nm^{-1}\,m^{-2}\,sr^{-1}}$. In daytime BGL measurements radiances between $1.09\,\mathrm{mW\,nm^{-1}\,m^{-2}\,sr^{-1}}$ and $4.17\,\mathrm{mW\,nm^{-1}\,m^{-2}\,sr^{-1}}$ were observed, exhibiting an offset from simulation tools. The results highlight the importance of system calibration for Optical Ground Station (OGS) based BGL measurements, while also providing insights into the magnitude of BGL usable for the system design in future satellite QKD missions.

Contents

List of Figures

List of Tables

List of Acronyms

AES Advanced Encryption Standard
AO adaptive optics
BGL background light
DCR dark count rate
DISORT Discrete Ordinate Radiative Transfer solver
FOV field-of-view
libRadtran library for radiative transfer
LIME Lunar Irradiance Model of the European Space Agency
MFD mode field diameter
MYSTIC Monte Carlo code for the physically correct tracing of photons in cloudy atmospheres
OGS Optical Ground Station
OGSOP Optical Ground Station Oberpfaffenhofen
QBER quantum bit error rate
QKD Quantum key distribution
RSA Rivest-Shamir-Adleman
RTE radiative transfer equation
SCPI Standard Commands for Programmable Instruments
SDE system detection efficiency
SKR secure key rate
SMF single mode fiber
SNSPD Superconducting Nanowire Single Photon Detector
SPAD Single Photon Avalanche Detector
TOA top of atmosphere

Chapter 1

Introduction

Throughout history, the secure transfer of information has consistently played a significant role. With the transition into a digitized world data is exchanged across the internet, e.g. when messages are sent, websites are visited, users are authenticated or payments are processed. To ensure a secure data transfer, private-key encryption such as the Advanced Encryption Standard (AES)[50] and public-key encryption such as the Rivest-Shamir-Adleman (RSA) cryptosystem[57] were invented to encrypt messages and authenticate users [23, 31].

As these algorithms rely on mathematical problems assumed to be computationally non trivial to solve, classical cryptography faces an imminent problem due to the uncertainty of the security of these algorithms. Due to the advancements in the development of classical algorithms and increasing computational power as well as the advancements in quantum research with quantum computers and quantum algorithms, the mathematical foundation of the classical algorithms is threatened [23, 53, 61]. Specifically, Shor's algorithm [64], a quantum algorithm, is capable of solving the prime factorization problem underlying prominent public-key encryption standards such as RSA with exponential speedup compared to known classical algorithms . While no such proven quantum algorithm for private-key encryption exists yet, an indirect threat is imposed on these systems too, as they rely on their private-key being shared in advance, often achieved by public-key encryption [16, 17, 23].

Quantum key distribution (QKD) was developed alongside post-quantum cryptography to ensure that secure data transfers and authentications can still be guaranteed in a post-quantum era. Instead of relying on mathematical problems and assumptions, QKD relies on the fundamental laws of quantum mechanics. A key is generated by encoding information in a quantum state and transmitting it over a quantum channel between the two participating parties. If a third party tries to intervene and access information of the quantum channel, their presence is inherently detectable due to their influence on the quantum states, which increases the quantum bit error rate (QBER). Although optical fibers are a common choice for providing the quantum channel, exponential transmission losses prohibit establishing global communication networks [17, 23, 61].

Satellite based QKD offers a solution to these limitations. Utilizing a satellite as a movable sender platform to exploit the quadratic losses of free-space propagation with an Optical Ground Station (OGS) receiver system on the ground, a global network can be established. However, realizing free-space QKD links introduces new challenges as additional noise is added to the quantum channel by background light (BGL). Contrary to classical communication, the signal strength in QKD cannot be increased, because the signal consists of ideally single photons or, in practice, weak coherent laser pulses mimicking a single quantum state. A sufficient signal-to-noise ratio is crucial, as a lower ratio increases the QBER. Any increase in the QBER, such as from BGL, must be attributed to the potential presence of an eavesdropper to ensure protocol security. If the QBER exceeds the protocol and system dependent threshold, the QKD protocol must be aborted, because an eavesdropper might have gained significant information. Therefore, mitigating the increase in QBER induced by BGL is essential. This can be achieved through various filtering techniques, including spatial, temporal and spectral filtering [5, 11, 17, 23, 25, 28, 37].

For ground and space system design, characterization and estimation of BGL contributions is critical for deploying effective countermeasures. State-of-the art BGL measurements have been conducted under daytime conditions with a collimator setup and were compared to simulations finding good agreements when certain simulation parameters were adjusted [28, 29]. However, the noise contributions of BGL during the day and night in satellite QKD setups involving an OGS have only been investigated theoretically, despite being crucial for system design. The Optical Ground Station Oberpfaffenhofen (OGSOP) offers a platform capable of engaging QKD downlinks[1] with Low Earth Orbit satellites. It features single mode fiber (SMF) coupling where a QKD receiver including a Superconducting Nanowire Single Photon Detector (SNSPD) can be connected to measure the quantum signal. This concept is currently followed in the satellite QKD missions QUBE and Eagle-1 [13, 55].

The research presented in this work aims to provide new insights into BGL measurement setups in the C-band for night and day measurements utilizing the OGSOP, as well as the calibration of the measurement setup regarding both the transmission loss and the SNSPD. Furthermore, measured BGL values will be provided to aid the system design for satellite QKD missions, and measured BGL results will be compared with simulations

[1] A downlink refers to the QKD scenario where the satellite acts as the transmitter of the quantum states while the OGS acts as the receiver.

to verify if the measurements fit the expectation. Therefore, this work will first built the necessary theoretical foundations in Chapter 2 to 5. Chapter 2 introduces the concept of classical cryptography highlighting its security concerns and why QKD is necessary in a post-quantum era. Afterwards, in Chapter 3, QKD is introduced, first in an ideal scenario to present the general concept, and second, in an experimental setting with the focus on single photon detection to build the foundation for the SNSPD calibration, the role of BGL and state of the art measurements. Chapter 4 provides the theoretical background for BGL simulations by deriving the radiative transfer equation (RTE) used to predict the transfer of BGL through the atmosphere, and presents the tools to solve the RTE. To compare the results of the BGL measurements with the simulation results and other setups, the measured count rates must first be converted to radiances. The formalism is given in Chapter 5, while the explicit routines are outlined in Section 7.3.
Chapters 6 to 8 outline the routines and measurement setups developed within the framework of this thesis. For the comparison of measured BGL with simulations, the existing tools from previous publications [28, 29] are expanded by testing an approach utilizing the Lunar Irradiance Model of the European Space Agency (LIME) to conduct BGL measurements during the night (see Chapter 6). Chapter 7 presents the optical setup used for the BGL measurements and introduces the routines for the transmission loss calibration and the performed measurement campaigns. The next chapter explains the optical setup, formalism and routine for the calibration of the fully recovered system detection efficiency (SDE)[2] of the SNSPD employed in the BGL measurement setup. Subsequently, all results of the transmission loss and SNSPD calibration measurements, and the BGL measurements, including the comparison with previous measurements and simulations, are presented and discussed in Chapter 9. Finally, Chapter 10 provides a conclusion and outlook for following experiments and future research based on the results of this work.

[2]The fully recovered SDE refers to the SDE with fully recovered detector bias.

Chapter 2

Classical cryptography

To understand the significance of quantum cryptography as a research domain, the core concept of classical cryptography has to be understood. Classical cryptography ensures a secure data transfer, preventing unauthorized parties from gaining information and allowing authorized parties to be identified. To achieve this, data is encrypted with a key before it is sent to a recipient. In the context of cryptography, implementations are categorized by the use of either a single key, known as symmetrical (private-key) encryption, or by multiple keys in an asymmetrical (public-key) encryption [23][31].

2.1 Private-key encryption

In private-key systems, also commonly referred to as symmetrical key system, a single key is employed for both encryption and decryption of messages. It is essential for the two parties involved, Alice (sender) and Bob (receiver)[1], to exchange the key via a secure channel such as a private meeting or a trusted courier. While private-key systems offer a high degree of security, they are not suited for managing large networks, due to requirement of keys need to be shared in advance. Reusing the same key creates vulnerabilities and enables Eve (an unauthorized party or eavesdropper) to derive the private-key by intercepting multiple messages. This renders the encryption process ineffective as Eve can subsequently decrypt the intercepted messages. Nevertheless, standards such as the Data Encryption Standard (DES) [51] or the modern AES [50] utilize private-keys and are widely employed in data encryption [23].

[1] Alice and Bob are commonly used to describe the sender and receiver in cryptography. Additionally, Eve is used as a synonym for an eavesdropper. This terminology will be adopted throughout the entire thesis.

2.2 Public-key encryption

In 1976, Whitfield Diffie and Martin Hellman introduced the concept of public-key cryptography [78], initiating a new chapter in the field of cryptography. Two years later, the first practical public-key cryptosystem, known as Rivest-Shamir-Adleman (RSA), was introduced [57].
In contrast to private-key systems, public-key cryptosystems, also commonly referred to as asymmetrical key systems, such as RSA utilize a pair of keys for the protocol. These keys are derived using of one-way functions. A one-way function describes any mathematical function for which it is computationally trivial to calculate $f(x)\ \forall\ x \in X$, whereas calculating the inverse $f^{-1}(y) = x$ is infeasible. For example, RSA leverages the integer factorization problem to generate a private key, which is linked to the public key shared with all other parties [31].

2.3 Security concerns and sustainability

The foundation of security in classical cryptography are the underlying mathematical problems. Tasks, such as the integer factorization and the discrete logarithm are widely assumed to be computationally difficult to solve. Nevertheless, concrete proofs cannot be provided [61]. Technological advances, resulting in increased computational power and the development of faster algorithms, pose a threat to these systems, questioning safety and viability in the future [23, 53].
In addition to conventional technological progress, the emergence of quantum computers and quantum algorithms imposes another level of threat. While the existence of fast classical algorithms remains unconfirmed, quantum algorithms such as Grover's algorithm [24] and Shor's algorithm [64] have been shown to speed up calculations posing a significant threat to current systems. Research indicates that the attacks on private-key systems via Grover's algorithm can be mitigated by increasing the key length, because the speed up scales with the square of the key length. However, Shor's algorithm breaks commonly used protocols such as RSA due a exponential speed up in computation time. In practice, private-key and public-key systems are frequently used in hybrid systems, combining the benefits of both approaches. As a result, breaking public-key systems indirectly affects private-key systems as well [16, 17]. To ensure that cryptography remains secure in the quantum era where quantum computers might exist, two distinct approaches are considered. Post-quantum cryptography focuses on research into quantum-safe approaches to classical cryptography. QKD offers a novel approach, promising a theoretical unconditional level of security based on the laws of quantum mechanics [53].

Chapter 3

Quantum Key Distribution

The Idea of QKD dates back to 1984, when Charles H. Bennett and Gilles Brassard presented their work *Quantum Cryptography: Public Key Distribution and Coin Tossing* at the International Conference on Computers, Systems & Signal Processing in Bangalore India. In their publication, Bennett and Brassard proposed to implementing cryptography using single photons by encoding information in their polarization states, creating the protocol now known as BB84 [8].
This chapter aims to elaborate the concepts of theoretical ideal and experimental QKD. It begins with the foundation of the unconditional security with the example of BB84 QKD, proceeds to discuss experimental realization strategies and challenges and concludes by examining the role of BGL and state-of-the art measurements.

3.1 Basics of QKD

QKD exploits multiple principles of quantum mechanics that, in most applications, are considered as limitations. In the context of QKD, however, these can be utilized to ensure cryptographic security. Specifically, they enable the detection of Eve, if she attempts to gather information from the quantum channel. The following principles form the foundation of the unconditional security offered by QKD [61].

1. Measurements on a quantum system cannot be conducted without disturbing its state.

2. An unknown quantum state cannot be cloned [79].

3. Bell inequalities are violated by measurements conducted on members of entangled pairs [18, 61].

Under these principles and within ideal circumstances, QKD provides unconditional security. The following sections discuss how such security can be established based on these principles (see Sections 3.1.1 and 3.1.2).

3.1.1 Unconditional security

QKD protocols are generally categorized as either prepare-and-measure or entanglement based protocols. Both differ primarily in the type of quantum state used to transmit the signal. In the latter the Bell inequalities play a major role in the detection of Eve [18]. In this thesis focuses on the more widely implemented prepare-and-measure protocols [65].
In prepare-and-measure protocols, two channels are utilized: an authenticated classical channel, used to communicate during the protocol and post-processing, and a quantum channel, used to transmit the quantum states prepared by Alice (see Figure 3.1).

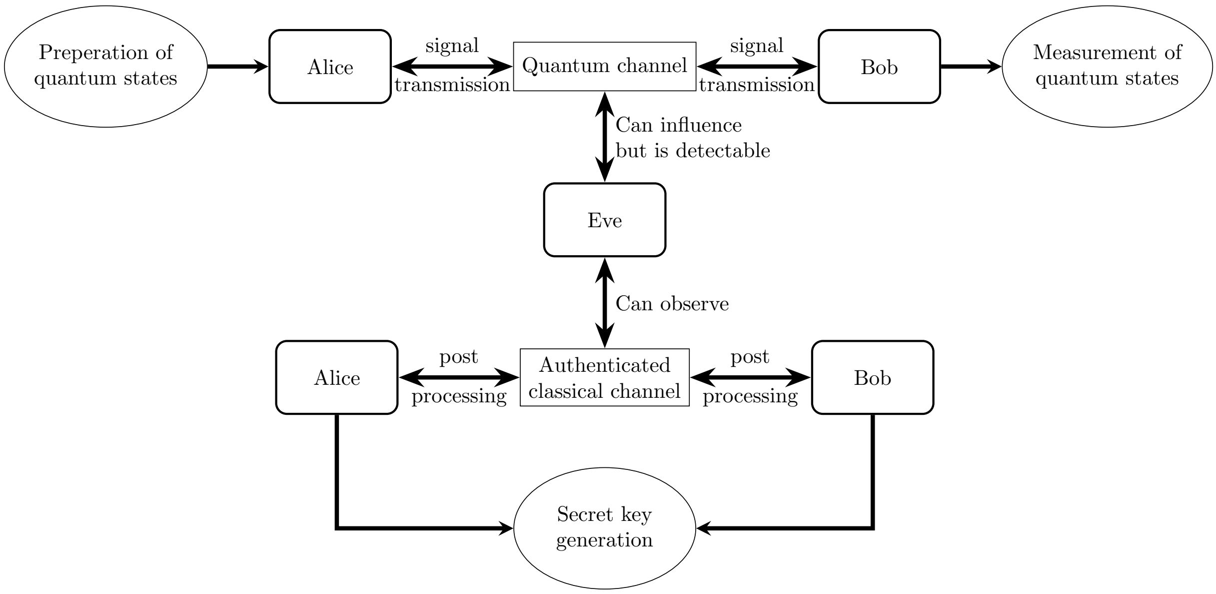

Figure 3.1: Schematic representation of prepare and measure protocols. Alice prepares quantum states which are transmitted via a quantum channel to Bob, who measures the received quantum states. During this process Eve could influence the quantum channel, but would be detectable in post-processing. During the protocol and in post-processing when the secret key is generated, Bob and Alice communicate via a authenticated classical channel. Eve can only observe this channel, but not interact. Inspired by [65].

Different prepare-and-measure protocols utilize various quantum states and different properties of light to encode information [65]. Continuous variable protocols employ coherent states and encode the information via the modulation of the quadrature components [34]. In contrast, discrete variable protocols employ Fock states (single photons), where information is encoded in e.g. phase, frequency or most prominently polarization [23].

To gain information Eve has to infer information from the quantum states without being detected by Alice and Bob. In an ideal scenario, Eve would intercept individual photons, create perfect copies for herself, and resend the original photons to Bob. This would allow her to retain the copies and measure them once Alice and Bob reveal which photons are used to generate the secure key. However, this eavesdropping strategy, commonly referred to as "intercept-and-resend" strategy, is precluded by the *No Cloning Theorem*, which states that no device can create a perfect copy of an arbitrary, unknown quantum state [23, 79].

In prepare-and-measure protocols, Alice and Bob select at least four different quantum states, which form two non-orthogonal bases for a two-level quantum system. Alice sends a random sequence of any of these states and Bob measures them in a randomly chosen basis. This process should yield an quantum bit error rate (QBER) of approximately 25%. If Eve tries to infer information about the sequence of photons, she must measure the photons directly, as she cannot create a perfect copy, and resend the photon to Bob. The fundamental principles of quantum mechanics dictates, that a measurement cannot be performed without disturbing the system. In 50% of the cases she might choose the correct bases, but in the other 50% of cases she will alter the original state due to her choosing the incorrect basis. This perturbation is unavoidable and will be detectable by Alice and Bob during post-processing by an increase in the QBER above the expected value. QKD, in contrast to classical cryptography, offers the unique benefit of directly identifying the presence of an eavesdropper who most likely would remain undetected in classical schemes. Upon detection of an eavesdropper, Alice and Bob can abandon and repeat the protocol until a secure key is established.[17, 23, 61].

3.1.2 Ideal BB84 protocol

BB84 was the first QKD protocol published and is categorized as a prepare-and-measure protocol that utilizes polarization as its discrete variable. The following explanation closely follows the original publication from Bennett and Brassard [8] and the notation from Dusek et al. [17]. BB84 can be split into the following steps

0. Choice of bases and bit mapping (Alice & Bob)
1. State preparation and transmission (Alice)
2. State measurement (Bob)
3. Post-processing (Alice & Bob)

Bases and Mapping Prior to the protocol's execution, Alice and Bob agree on their selection of non-orthogonal bases. Commonly, the horizontal ($|H\rangle$), the vertical ($|V\rangle$), the diagonal ($|D\rangle = \frac{1}{\sqrt{2}}(|H\rangle + |V\rangle)$) and the anti-diagonal ($|A\rangle = \frac{1}{\sqrt{2}}(|H\rangle - |V\rangle)$) polarization states are chosen. In addition to the selection, the polarization states must be mapped to classical bits (0 and 1). Each bases must represent both bit values. Following these rules, the mapping adopted in this thesis will be $|H\rangle \equiv 0, |V\rangle \equiv 1, |D\rangle \equiv 0$ and $|A\rangle \equiv 1$, consistent with the original protocol.
State preparation To initiate the protocol, for a set of N photons, Alice selects a bit to encode and chooses a random base and a corresponding polarization state p $\in \{|H\rangle, |V\rangle, |D\rangle, |A\rangle\}$. Similar to classical cryptosystems, the selection must be random. No deterministic pattern should underlie the choice of p. Ensuring true randomness is a delicate problem even with modern hardware, which inherently are deterministic. For further detail, refer for example to Section III D of the works of Nicolas Gisin [23]. Following preparation, Alice transmits the photons via a quantum channel to Bob. This channel may be an optical fiber, a free-space and line-of-sight link or a free-space satellite to OGS link [11, 23].
State measurement Bob receives the photons sent by Alice and chooses to measure in either of the two bases. The choice has to be random and independently of Alice. If the basis chosen coincides with Alice's basis a deterministic result is expected. Otherwise the result will be random [17].

$$\begin{aligned} &\text{Expected results depending on Bob's bases choice} \\ \langle H|V\rangle &= \langle A|D\rangle = 0 \\ \langle H|H\rangle &= \langle V|V\rangle = \langle D|D\rangle = \langle A|A\rangle = 1 \\ |\langle H|A\rangle|^2 &= |\langle H|D\rangle|^2 = |\langle V|D\rangle|^2 = |\langle V|A\rangle|^2 = \frac{1}{2} \end{aligned} \tag{3.1}$$

Post-processing Following the transmission of the signal Alice and Bob exchange certain information via the classical channel to distill the secure key.
In the first step, Alice and Bob disclose the bases chosen for each photon preparation and measurement respectively via a classical channel, without disclosing specific bit values or measurement outcomes. They proceed to discard any instances in which the bases do not correspond. In an ideal scenario, statistically, Alice and Bob are left with a sifted key of length N/2 [23].

To detect potential eavesdropping, Alice and Bob compare a random subset of their remaining bits. If these are all identical[1], they are left with a secure key consisting of the undisclosed bits (see the example protocol in Table 3.1). Conversely, any nonidentical bits indicate that Eve gained some information. To determine, whether the protocol has to be abandoned or if additional steps of post-processing can be applied, Alice and Bob calculate the QBER. The QBER describes the error of the sifted key and is calculated by dividing the number of erroneous bits by the total number of bits compared [23].
Each QKD protocol has specific theoretical and experimental limits, for which a secure key can be extracted. If the determined QBER is below those limits, a secure key can be extracted by applying error correction and privacy amplification techniques. These processes reduce the information Eve has gained below a significant level. For more details on this topic refer to e.g. Section II C 4 of Gisin [23] or section 7 of Dusek [17].

Quantum transmission										
Alice's choice of bit	1	1	0	1	0	0	0	1	0	1
Choice of bases	R	D	R	R	D	D	R	D	R	R
Bob's measurement bases	D	D	R	D	D	R	D	R	R	R
Received bit	0	1	0	1	0	0	1	1	0	1
Post-processing										
Shared bases by Bob	D	D	R	D	D	R	D	R	R	R
Alice's confirmation	-	✓	✓	-	✓	-	-	-	✓	✓
Shared bits by Bob	-	1	-	-	-	-	-	-	0	-
Confirmation of shared bits by Alice	-	✓	-	-	-	-	-	-	✓	-
Remaining secret bits			0		0					1

Table 3.1: The table represents the process of an ideal BB84 protocol in absence of an eavesdropper and imperfections in the experiment. After post-processing, the remaining secret bits already correspond to the secret key. In a realistic scenario effects such as e.g. missed detections would need to be taken into account in post-processing. This table was built in reference to the first table in [8].

[1] This assumption does only hold in an ideal scenario, as in real experiments, imperfections in the system will lead to erroneous bits.

3.2 Experimental QKD

In 1989, Charles Bennett and Gilles Brassard successfully demonstrated the transmission of a secure key over the distance of 30 cm using the setup shown in Figure 3.2. They were able to transmit 443 perfectly matching bits between Alice and Bob. Subsequent post-processing reduced the key to a length of 175 bits. However, this process minimized the expected knowledge of Eve to approximately 5×10^{-9} bits, marking the first experimental demonstration of QKD [6].
QKD systems have undergone steady improvements since this first demonstration. Various configurations regarding quantum channels and protocols have been explored, increasing both transmission distances and the secure key rate (SKR)[2]. Optical fiber-based approaches have been the subject of extensive research. Utilizing different protocols distances of e.g. 307 km with a SKR of 3.8 bits/s (2015) [32] or up to 833.8 km with a SKR of 0,014 bits/s [75][3] could be achieved. A demonstrated by e.g. Rossi et al. [59] free-space distances of 18 km in an urban environment could be achieved with SKR of 1 kbit/s. In the year 2025 Yang Li et al. demonstrated a secure communication over a distance exceeding 12.900 km on Earth using secure keys previously distributed via a satellite to multiple OGS [35].

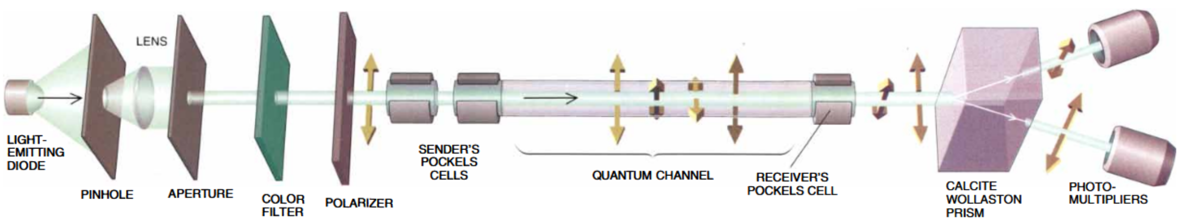

Figure 3.2: Using an LED as a source of faint light pulses in conjunction with pockel cells to alter the polarization state, this setup was the first to demonstrate QKD in an experiment spanning over a distance of 30 cm in free-space. The calcite crystal was utilized to split the polarization states. Taken from [7].

Overall, the field of experimental QKD is undergoing rapid and diverse development across multiple domains. A primary objective to enable long-distance QKD is maximizing the signal-to-noise ratio. In classical communication, one can typically increase the signal or decrease background noise to achieve a good signal-to-noise ratio. However, in QKD, it is not possible to enhance the signal due to the use of single photons or weak coherent

[2]The secret key rate (expressed in bits/s or bits) is a protocol and experiment specific parameter used for performance estimation. It defines the number of secret bits generated per second and often is given as a function of the QBER or overall system losses [4, 17]. Modelling of the SKR for BB84 can be found in e.g. [12] or [27].

[3]The paper examines performance over various distances. For shorter distances higher SKR were established.

pulses. Consequently, the only viable method to increase the signal-to-noise ratio is to minimize channel attenuation and background noise [11].

These constraints lead to a range of technical challenges that vary depending on the quantum channel and the chosen protocol. These technical challenges impose limitations on QKD, which can be categorized as in Section 6 in [17].

Operational range The range over which QKD is feasible is primarily limited by the attenuation of the quantum channel, which decreases the signal-to-noise ratio. Furthermore, the use of traditional amplifiers in QKD systems is not possible in QKD [17, 28]. Additionally, the impact of the DCR of the detection system and BGL increases with increasing transmission distance. As the rate of arriving signal photons decreases, the relative contribution of both noise sources to erroneous counts becomes significantly more detrimental to the key generation process. Combined with the chosen transmission wavelength, these factors constrain the selection of an optimal detector (see Section 3.2.1)[17].

Transmission rates Similar to the operational range, the use of weak laser pulses, ideally single-photons, constrains the achievable key generation rate. In this context, the dead time of the chosen detector may impose additional limits on the pulse repetition rate especially in fiber based QKD[17]. In free-space QKD this limitation is relaxed, as the main limiting factor is the transmission loss of the quantum channel [11].

Furthermore, the generation of the weak laser pulses is a challenge in itself [23, 61]. In the standard BB84 protocol, an average photon number higher than one will enable a new attacking strategy, commonly referred to as photon-number-splitting attack (PNS), compromising the security of the protocol [23, 61]. In this attack, Eve can intercept one photon of a multi-photon pulse, while the other photon reaches Bob unaltered. Due to the lack of a measurement, this attack could go undetected as Alice and Bob cannot know, when such pulses occur. To counteract this attacking strategy, the decoy-state BB84 protocol was introduced, which utilizes additional decoy pulses which are intentionally created with a photon number higher than one, to identify the presence of Eve [36, 39, 76].

The following sections focus on selected aspects of these challenges that align with the works of this thesis including the discussion of single-photon detection in Section 3.2.1, the comparison between fiber-based QKD and free-space QKD in section 3.2.2, and the role of BGL and state-of-the art measurements in Sections 3.2.3 and 3.2.4.

3.2.1 Single photon detection

The selection of optimal detectors and detection methods for QKD depends on various factors. Continuous variable protocols require homodyne detection methods (see Section II G.2 in [61]), whereas discrete variable protocols utilize photon-counting detectors. To achieve optimal results, tight constrains must be met (see Table 3.2). Satisfying all constraints simultaneously is hardly achievable. Consequently, a trade-off is typically required [23]. Most frequently, Single Photon Avalanche Detectors (SPADs) and Superconducting Nanowire Single Photon Detectors (SNSPDs) are implemented, as they offer a low cost, compact solution while maintaining high performance parameters. For long transmission distances transitioning to detectors such as the SNSPD is necessary [80].
SNSPDs provide extremely low dark count rates (DCRs) and minimal timing jitter[4], while exhibiting high detection efficiencies. One primary disadvantage is that additional loss is introduced, as SNSPDs are reliant on single mode fiber (SMF) coupling.
Contrary to most SPADs, SNSPDs require cryogenic cooling to almost absolute zero, rendering them larger in size [49]. In the following, the physics of single-photon detection using SNSPDs is explained. Unless stated otherwise, this explanation closely follows the work of Natarajan et al. [49]. More recent developments are described in e.g. [60].

Symbol	Property	Requirement
η_{det}	detector efficiency	high for desired spectral range to reduce the loss of signal photons
R_{dcr}	dark count rate	low to reduce noise
Δt	timing jitter	precise to monitor the arrival times of photons
τ_{rec}	recovery time or dead time	short to increase detection rates
-	system complexity	depending on system requirements

Table 3.2: Requirements and constrains on photon detector properties for QKD applications. The dead time describes the time at which no detection events can occur. However, SNSPD system do not posses a “real„ dead time, but a recovery time.

Superconductivity, exhibited by materials cooled below their characteristic critical temperature (T_C) [3], forms the foundation for the operation of SNSPDs. When cooled below its critical temperature T_C, a material undergoes a phase transition, resulting in the total

[4]Timing jitter describes the time difference between photon absorption and electrical signal output [49].

loss of electrical resistance [5]. This effect can be exploited to detect incoming radiation as schematically shown in Figure 3.3.

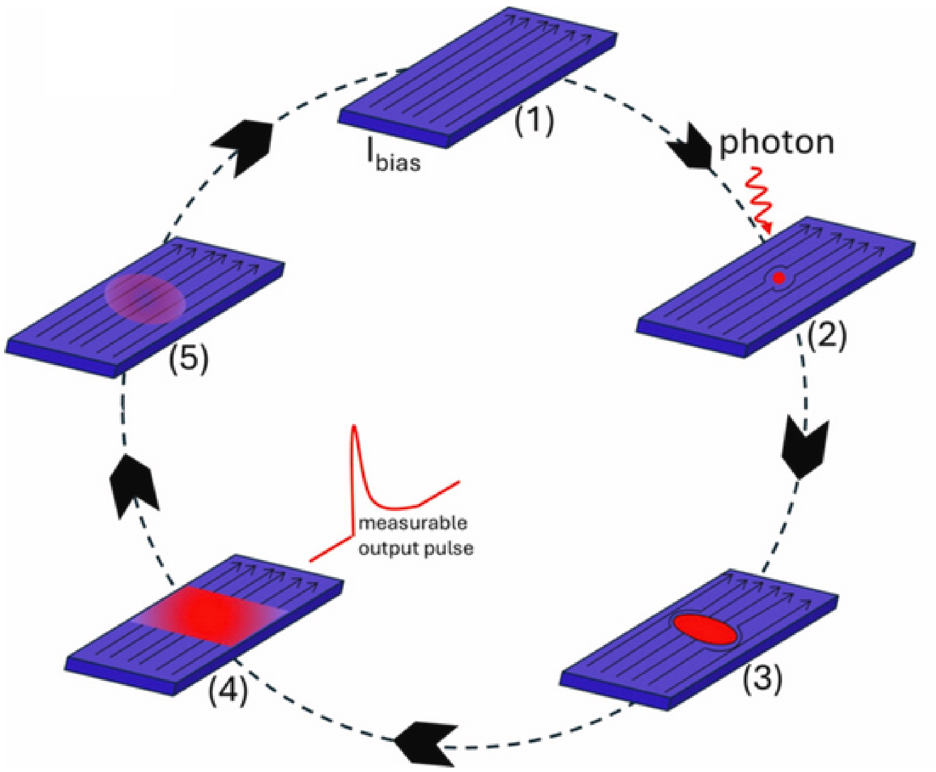

Figure 3.3: Phases during a detection cycle of a SNSPD. (1) A thin nanowire is biased with $I_{bias} < I_C$. (2) An incident photon creates a hotspot with finite resistance by breaking up cooper pairs. (3) The current is forced to flow around the hotspot increasing the current density in these regions. (4) The increased current density leads to the formation of a resistive barrier spanning the whole width of the nanowire detectable as a voltage pulse (5) The hotspot dissipates, recovering the superconductive state and bias current flow. Graphics taken from [60] Figure 1 a).

Inside a SNSPD thin nanowires with widths of a few nm are arranged in a meander (typically in order of µm × µm) atop of a substrate that acts as a heat sink. These nanowires are cooled until they reach their superconductive state and a bias current (I_{bias}) slightly below the critical current (I_C) is applied to the nanowire. Incoming radiation disrupts the state of superconductivity[6] by breaking up Cooper pairs within the superconductor, forming a localized resistive are known as a hotpot. The current is forced to flow around this resistive are, subsequently increasing the local current density around the hotspot until a resistive barrier is formed across the width of the nanowire. This sudden transition

[5]Additional phenomena occur, e.g. the Meissner-Ochsenfeld effect [3], though these are not directly relevant for the operating mechanism of a SNSPD.

[6]This effect was first demonstrated by L.R. Testardi in 1971 [71].

from zero to finite resistance results in a detectable voltage spike. Following the detection event, the energy dissipates through the substrate via various relaxation processes including e.g. electron-phonon interactions, returning to the current level to I_{bias}. During the recovery phase, the SNSPD is less sensitive to subsequent detections. This process is typically characterized by a time constant, the recovery time τ_{rec}.
Depending on the architecture of the SNSPD, ultra low DCRs, reduced recovery times and minimal timing jitter can be achieved through the correct choice of geometry, readout circuit design and bias current. The system detection efficiency (SDE) (η_{sde}) can reach values exceeding 98% [49, 60]. As defined in Equation 3.2, the SDE is the product of the coupling efficiency (η_{coup}), absorption efficiency (η_{abs}) and registering efficiency (η_{reg}). The detector efficiency η_{det} describes the efficiency with perfect coupling $\eta_{coup} = 1$. All parameters are device-dependent and are influenced by the meander geometry, material selection and the optical coupling onto the meander.

$$\eta_{sde} = \eta_{coup} \cdot \eta_{abs} \cdot \eta_{reg} \tag{3.2}$$

In operation, the SDE as well as the DCR increase with increasing I_{bias} (see Figure 3.4) [49]. Furthermore, the former depends on the arrival time between photons, which is directly related to photon rate of the incident photons by

$$\tau_{ph-ph} = \frac{1}{R_{ph}} \tag{3.3}$$

If photons arrive while the bias current is recovering, the SDE has not fully recovered to its original value ($\eta_{sde,0} \equiv$ fully recovered SDE). On time scales, where $\tau_{ph-ph} \sim \tau_{rec}$, this effect (see Figure 3.5) has to be taken into account (see Section 5.1). In case of low photon rates ($\tau_{ph-ph} >> \tau_{rec}$), a simple step function approach for the SDE might be taken [56]. In addition, the SDE can exhibit a polarization dependency depending on the meander geometry[7]. Due to the sub-wavelength dimensions of the nanowire, it can act as an optical grating. When the electrical field is aligned parallel to the nanowires, the SNSPD exhibits a maximum efficiency. Conversely, for perpendicular alignment the efficiency is minimized.

[7]The SNSPD system employed in the BGL measurement setup does exhibit a polarization dependency.

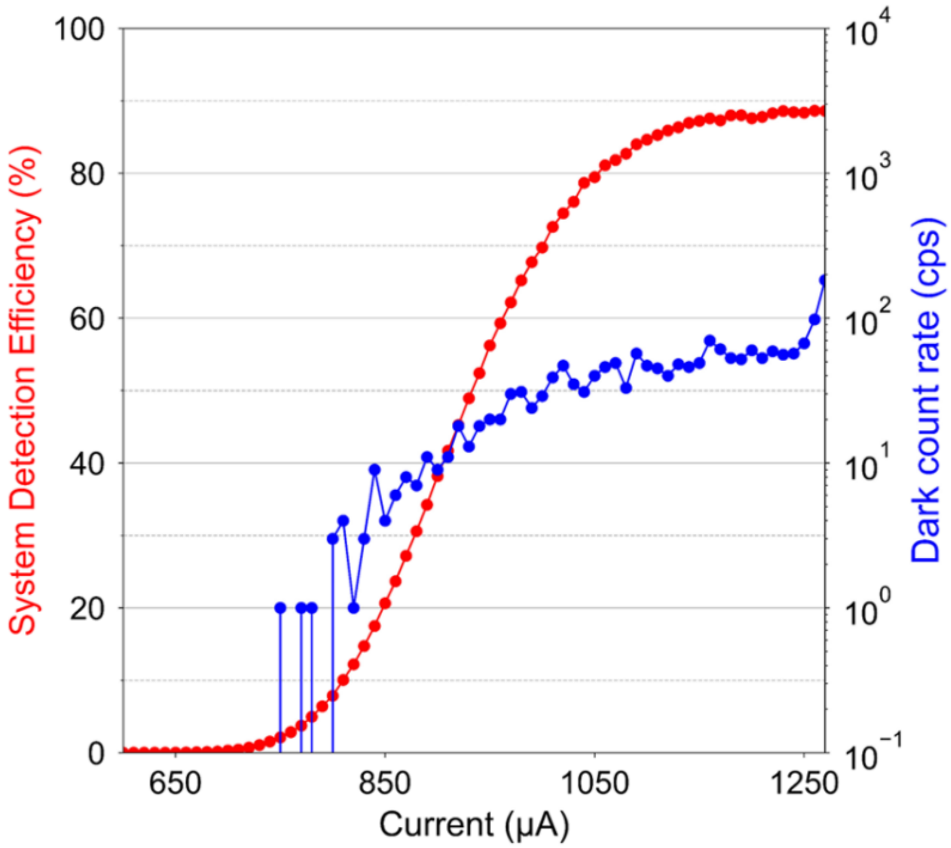

Figure 3.4: SDE and DCR for varying bias current measured at 1550 nm for a multipixel SNSPD. Graphics taken from [70] Figure 1 c).

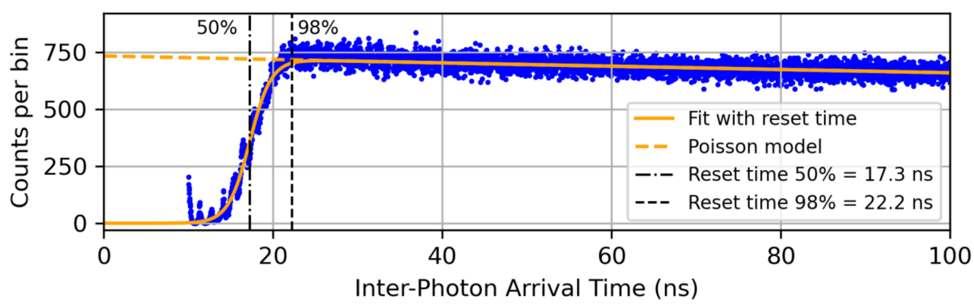

Figure 3.5: SNSPD counts measured under continuous illumination in dependency of the arrival times between photons fitted with a sigmoid function. In this thesis, the reset time is referred to as recovery time. Graphics taken from [56] Figure 2.

3.2.2 Fiber and free-space QKD

The most common implementations of Quantum key distribution (QKD) focus on fiber-based and free-space approaches. Both offer distinct individual advantages and disadvantages (see Table 3.4) [17, 23, 37, 61].

Fiber-based approach In fiber-based implementations SMFs are utilized to transmit the quantum states between Alice and Bob. Two wavelength bands are primarily considered when experiments are conducted with optical fibers, the NIR band and C-band. The trade-offs associated with choosing either one are summarized in Table 3.3. The main differences between them are the available detectors and the attenuation experienced in fibers. As the C-band is the standard telecommunication band, fibers with very low losses are available, giving the C-band a significant advantage for long distance applications. The drawback, however, is that the most efficient detectors, SNSPDs and InGaAs SPADs, require cryogenic cooling [23].

Optical fibers manufactured for the NIR band typically experience higher losses, but allow cheaper and less bulky Silicon SPADs to be used [23, 61]. One issue limiting the choice of protocols stems from the fact, that fibers induce disturbances to polarization states. Contributing effects include birefringence and polarization mode dispersion, which complicate the application of polarization encoding. Consequently, most fiber implementations feature phase encoding schemes [17].

	NIR band	C-band
Attenuation coefficient (α)	$2\,\mathrm{dB\,km^{-1}}$ [23]	$0.2\,\mathrm{dB\,km^{-1}}$ [61]
Detection	Si SPADs	InGaAs SPADs,SNSPDs
Challenges	polarization mode dispersion, birefringence	
Protocols	based on phase encoding	

Table 3.3: Wavelength constrains in fiber based QKD.

Free-space Approach Free-space QKD can further categorized into two distinct approaches: a terrestrial direct line-of-sight links or a satellite-based links can be established. The primary difference between these implementations is the duration and distance the signal spends within the atmosphere. While for a line-of-sight approach the signal travels through the atmosphere across the entire path, the atmospheric portion for a satellite link is small compared to the overall propagation distance as most of it is within the vacuum of space. Line-of-sight implementations are considerably more limited in range than satellite links, which offer potential to establish a global quantum communication network [27].

In the atmosphere, the transmission is affected by a multitude of effects. These effects include various scattering processes - such as Rayleigh scattering scattering, Mie scattering, aerosol scattering - as well as absorption by molecules and aerosols, which are highly dependent on the constituents of the atmosphere at the location of interest. The Earth's atmosphere features certain transmission windows (see Figure 3.6) at 850 nm, 1064 nm and 1550 nm respectively, which can be utilized for optical communication protocols such as QKD [22].

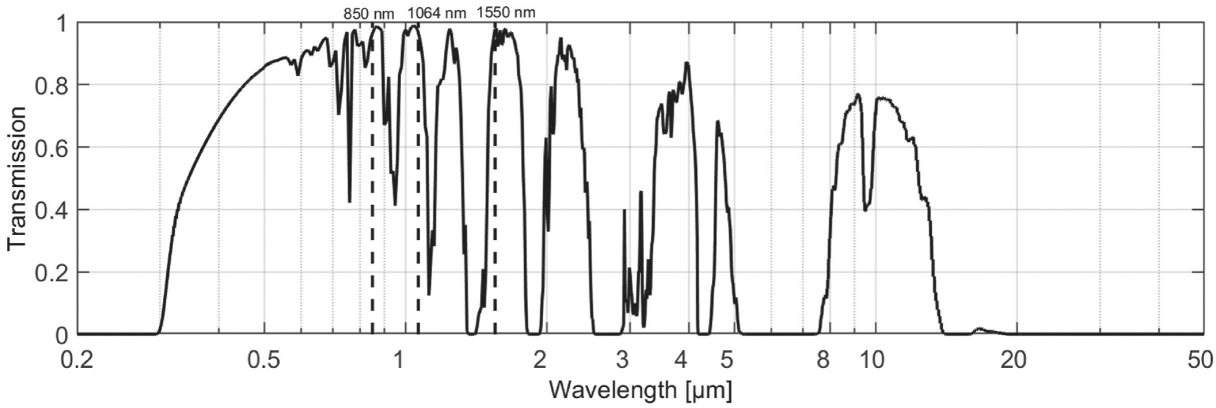

Figure 3.6: Transmissivity from sea level to space at zenith position. Marked are the three important transmission windows, 850 nm, 1064 nm and 1550 nm. Graphics taken from [22] Figure 2.

For free-space experiments, the NIR band is preferred due to the easier setup, but the C-band offers significant reduction in noise due to its compatibility with standard telecommunication equipment and less impact by the solar irradiance (see Figure 3.7). In addition, Rayleigh scattering scales according to $1/\lambda^4$, further reducing the noise contributions at longer wavelengths [66].

In free-space based implementations the main limiting factors stem from atmospheric turbulence, which induces beam wander and beam broadening. In most cases, the latter is the dominant effect and beam wander can be neglected. The impact of beam broadening in satellite links is highly dependent on the configuration of transmitter and receiver. In case of a downlink scenario, where the satellite acts as transmitter and an OGS as receiver, the signal first propagates through the vacuum of space, experiencing no broadening effects. Conversely, in an up-link scenario (satellite as the receiver and an OGS as the transmitter), the beam is broadened at the beginning of its journey. This leads to a substantial expansion of the beam by the time the satellite is reached. In comparison, the effect is less detrimental in downlink scenarios as only the last 10 km of the path are within the atmosphere [11, 37]. While overall losses in free-space scale with the square of the distance, whereas losses in optical fibers scale exponentially with distance, the former are less predictable. The Earth's atmosphere is a complex system where conditions can

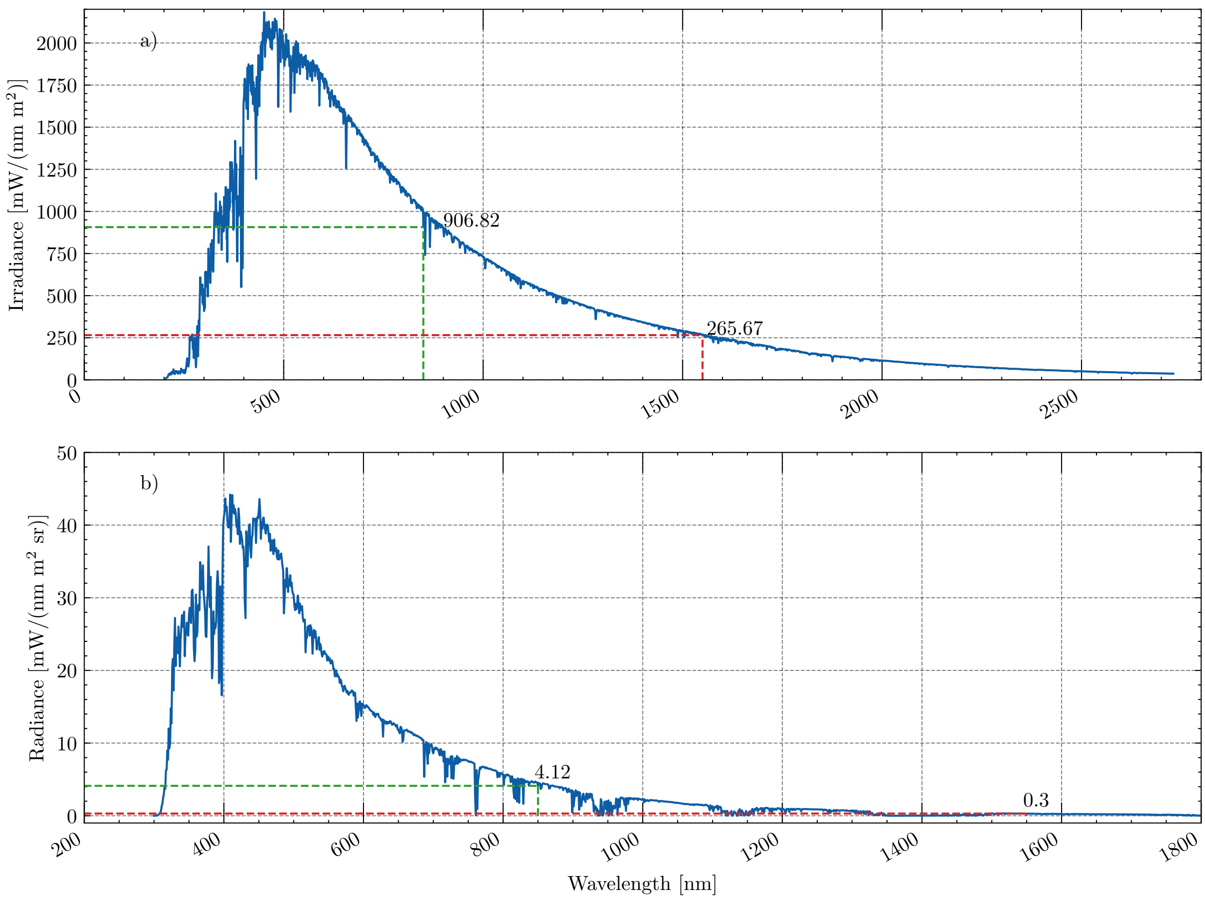

Figure 3.7: a) *TSIS-1 HSRS spectrum* (solar spectrum) [15]. b) Simulated radiances using the *uvspec* model from the library for radiative transfer (libRadtran)[20, 40]. The settings are described in Section C.1. Marked in green and red are the values for 850 nm and 1550 nm respectively. The irradiance at 1550 nm is smaller by a factor of approximately 3.4, increasing to a factor of 13.7 in the simulated radiance in the reference scenario.

vary rapidly and differ significantly between locations. Atmospheric pressures decays exponentially with altitude. Since pressure is directly linked to molecule density, it affects the transmission of light. Furthermore, the concentration of specific molecules in the atmosphere is heavily influenced by location and weather. For example, urban environments feature higher concentrations of anthropogenic molecules such as e.g. CO_2 (carbon dioxide) or CH_4 (methane). At higher altitudes above 10 km, the constituents are primarily dominated by the accumulation of volcanic ashes, which fluctuate depending on volcanic activity [22]. In clear sky conditions the attenuation can be lower than attenuation experienced in optical fibers [61]. However, in non ideal weather conditions, such as rain or mist, attenuation can increase dramatically, reaching values up to 20 dB km^{-1} [17]. In addition to directly contributing to the attenuation of free-space QKD, the atmospheric conditions heavily influence the noise introduced by e.g. the solar sky radiance, which is commonly grouped under the name of background light (BGL). Different techniques can be employed to predict and mitigate the impact of BGL as seen in the following section [28, 29, 37].

	Optical fiber	Free-space (line of sight)	Free-space (satellite)
Loss scaling	exponential with distance	quadratic with distance	
Loss sources	random scattering in fiber	atmospheric scattering and absorption	
Noise sources	detector noise	BGL	
Implemented encoding	phase-encoding	polarization-encoding	
Wavelengths	NIR band and C-band	NIR band (and C-band)	
Advantages	indep. of external conditions	no fiber link needed	enables global communication network
Disadvantages	limited range	line of sight, dep. on atmosphere	complex technology, dep. on atmosphere

Table 3.4: Overview of the different implementations for the quantum channel. While the C-band is explored more in free-space QKD, the NIR band is still preferred.

3.2.3 The role of background light in free-space QKD

BGL in satellite QKD originates from various sources (see Table 3.5). During daytime operation, the primary source is the solar sky radiance, which dominates all other sources. It is classified as a diffuse radiation components, as telescopes during optical communication avoid direct sunlight. At nighttime, sky radiance is dominated by the Moon, stars and planets. In contrast to daytime operation, these celestial bodies may appear within the field-of-view (FOV) of the telescope during communication. As a result, both direct and diffuse radiation must be considered. Additional phenomena that contribute during nighttime operation are zodiacal light [8], airglow[9] and emissions by other galaxies that light up the night sky. Former sources include all natural sources of BGL. Light generated by human activity is categorized as anthropogenic light. Anthropogenic light, emitted by e.g. buildings and vehicles, can also scatter into the FOV of the telescope. The contributions of anthropogenic light are closely linked to the geographic location of the receiver and play a significant role in urban environments than in remote locations [25, 28].
A common BGL source independently of operation time, is referred to as channel crosstalk and reflections from the transmitter device. Channel crosstalk incorporates the noise contributions which stem from other sub-systems such as the satellite tracking system which may stray into the quantum channel and contributes as direct and diffuse radiation [25, 28].

[8]Zodiacal light describes the light scattered towards the Earth by interplanetary material [19].
[9]Airglow refers to the light emitted by molecules and atoms in the upper atmosphere [14].

Source	Type of radiation
solar sky radiance (Sun)	diffuse
lunar sky radiance (Moon)	direct and diffuse
stars and planets	direct and diffuse
zodiacal light, airglow, emission in the galaxy	diffuse
reflections of the transmitter device	direct
channel crosstalk	direct and diffuse
anthropogenic light	diffuse

Table 3.5: Sources of BGL classified by their impact as either diffuse or direct radiation. The table is taken from [28] and was slightly adapted.

Not only is the magnitude of BGL dependent on the location due to varying contributions of anthropogenic light, but also it is influenced by specific atmospheric conditions and their impact on the light propagation. Light emitted by any source interacts with the aerosols within the atmosphere before eventually being scattered into the FOV. Consequently, light is scattered and absorbed in different ways depending on the composition of local aerosols and particles [25, 28].
Beyond atmospheric conditions influencing the propagation of light and the overall sky brightness being influenced by various sources, the amount of BGL coupled into the system is dependent on the systems design. Figure 3.8 provides a schematic of a basic receiver system. It incorporates several techniques to mitigate the impact of BGL such as temporal filtering (time gating) of the detector and spectral and spatial filtering [25].

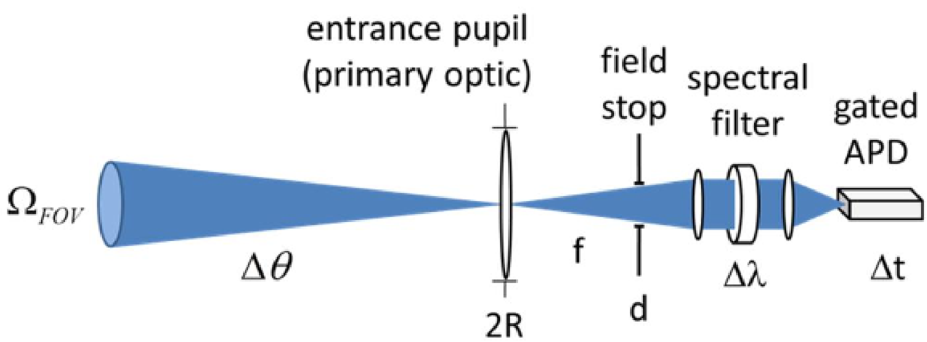

Figure 3.8: Example schematic for an optical receiver system comprising spectral filtering, temporal filtering via a gated avalanche photon detector, and a primary optic. Graphics taken from [25] Figure 1.

The number of noise photons incorporated in the system is quantified by equation[10]

$$N_{\mathrm{ph}} = \frac{I_{\mathrm{sky}} \cdot \Omega_{\mathrm{FOV}} \cdot A_{\mathrm{rec}} \cdot \lambda \cdot \Delta\lambda \cdot \Delta t}{hc} \tag{3.4}$$

By adjusting the gating time of the detector[11] the amount of detected BGL can be limited. This technique requires precise synchronization between the transmitter and the receiver, as the arrival time of the photons must be known. Effective spectral filtering (reducing $\Delta\lambda$) can be achieved by employing (ultra-)narrow filters of less than 1 nm. Regarding telescope design, modifications are limited to the reduction of Ω_{FOV}, as reduction of $\mathrm{A}_{\mathrm{rec}}$ would simultaneously decrease the collection of signal and noise, thereby negatively impact the signal-to-noise ratio. As a result, a narrow Ω_{FOV} is the primary way to reduce contributions of BGL while designing the telescope [37]. Effective spatial filtering is currently achieved with adaptive opticss (AOs), which reduces wavefront distortion induced by atmospheric turbulence at the potential cost of a more complex optical setup and aid SMF coupling. SMF would offer the best spatial filtering, but are limited by the effectiveness of the coupling. Overall, the amount of BGL that is coupled into a system can be influenced heavily by its design even though the sky radiance $\mathrm{I}_{\mathrm{sky}}$ is dependent on the location and the atmosphere [25, 59].

Suppressing BGL through system design is highly important, since BGL increases the QBER and any increase in QBER must be attributed to the potential presence of an eavesdropper. The degree to which BGL has to be suppressed depends on the protocol and system attenuation. Without proper suppression techniques, BGL can increase the QBER above the threshold at which the protocol must be aborted, because an eavesdropper might have gained significant information[5]. The limits imposed on the amount of BGL coupled into a QKD system, can be estimated by models for the QBER. Such a model has been developed, for instance, for the decoy-state BB84 protocol by Häusler et al. [28]. Figure 3.9 illustrates the QBER for a specific background radiation. The QBER is calculated by dividing the amount of erroneous detection events by the total number of detections (see Equation 12 in [28]). Both quantities depend on the background radiation, system attenuation, detector efficiency, DCR and gating time (see Equations 10 and 11 in [28]). Figure 3.9 shows that for system attenuation's exceeding 35 dB, contributions of BGL must remain below 15 mW nm^{-1} m^{-2} sr^{-1} to allow a successful QKD protocol. At higher attenuation levels, the impact of BGL becomes more severe and stronger BGL suppression is required.

[10]This equation is identical to Equation 1 in [25], where $\mathrm{A}_{\mathrm{rec}}$ is given as πR^2 and the sky radiance is named H_{b}.

[11]Gating time describes the temporal window the detector is active and detecting photons.

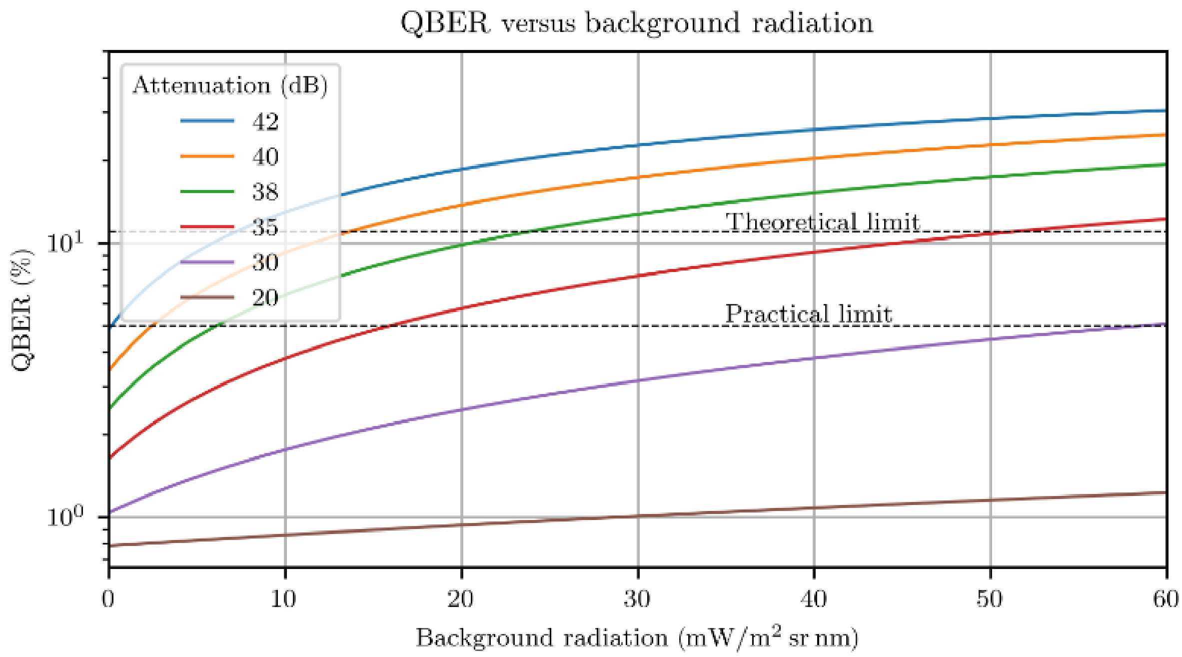

Figure 3.9: QBER in dependency of background radiation and quantum channel attenuation for a decoy-state BB84 protocol. The theoretical and experimental limit mark the QBER above which secure key generation is feasible. Graphics taken from [28] Figure 3.

The expected BGL can be estimated by the means of simulation, as shown in [28, 29]. Figure 3.10 illustrated solar sky radiance maps, that have been created using the *uvspec* model from the library for radiative transfer (libRadtran) [20, 40] for a wavelength of 1565 nm. The solar sky radiance varies greatly, depending on the aerosol composition in the atmosphere (see Figure 3.10 a)) and the position of the Sun (see Figure 3.10 b)). Expected radiances can additionally vary drastically within a fixed scenario, depending on the telescope position. While for a Sun position at 30° elevation, the solar sky radiance close to the surface in the direction of the Sun can reach values as high as 57 mW nm^{-1} m^{-2} sr^{-1}, it can also reach values as low as 0.48 mW nm^{-1} m^{-2} sr^{-1} in the opposite direction, with the Sun at the back of the telescope.

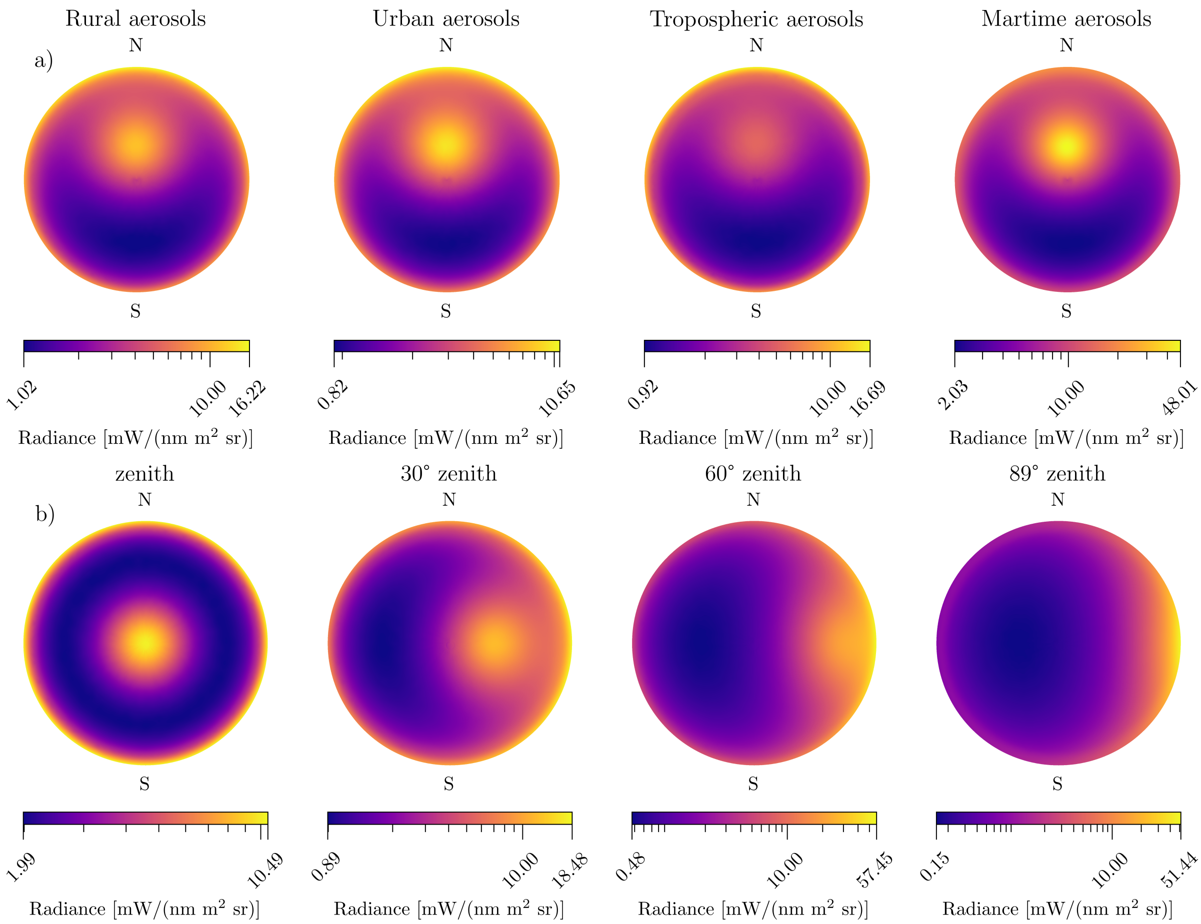

Figure 3.10: a) Simulated sky radiance maps with varying aerosol compositions for a fixed Sun position.b) Simulated sky radiance maps with varying source positions for a fixed aerosol composition. The simulation settings can be found in Sections C.2 for a) and C.3 for b).

3.2.4 State-of-the art background light measurements

BGL can be characterized either by the means of simulation or through direct measurements. A state-of-the art measurement device and measurement results for the C-band are presented in the works of Stefanie Häusler et al. in [28, 29]. The experimental setup used consists of a bandpass filter, a collimator and and optical fiber connected to a single photon detector[12] (see Figure 3.11). This collimator setup was utilized to measure the solar sky radiance at the location of Oberpfaffenhofen, Germany, and the University of Waterloo, Canada, for different azimuth directions and varying elevation angles. The results of the measurements were compared with simulated radiances using the libRadtran. To convert the measured count rates to measured radiances, both publications rely on component characterizations provided by the respective manufacturers. An example of the results, a measurement series performed at the University of Waterloo is illustrated in Figure 3.12[13]. To align the simulated radiances with the empirical data, two input parameters for the simulation were adjusted: the surface albedo (reflectance) and the visibility.

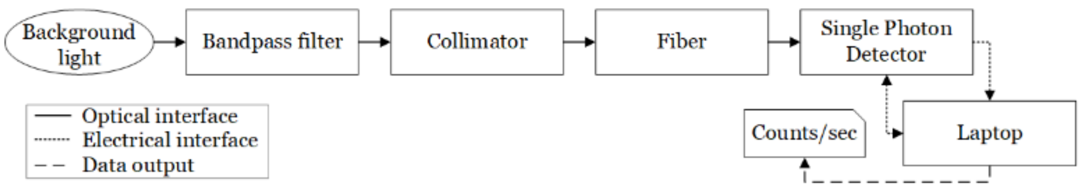

Figure 3.11: BGL measurement setup used in Waterloo [29] and in Oberpfaffenhofen [28]. Taken from [29] Figure 2.

It is possible to identify multiple combinations of albedo and visibility that yield good approximations of the empirical data as shown in Figure 3.13. This Figure visualizes the correlation between measured and simulated radiances for different combinations of albedo and visibility[14]. The graphic depicts the median ratio between the measured and simulated radiances across all measurement positions shown in Figure 3.12, hence, a value greater than one denotes a general underestimation by the simulation, whereas a value less than one a marks an overestimation. Nevertheless, the choice of appropriate albedo and visibility values must fit the environmental conditions during the measurement and cannot be chosen based on pure mathematical optimization. Both publications demonstrated, that, measured solar sky radiances can be predicted by simulation tools under the assumption that the albedo and visibility are constrained to a justifiable regime.

[12]For the employed optical components refer to Table 1 in [29] or Table 2 in [28]

[13]The original graphic is located in [29] Figure 3, bottom left.

[14]This visualization was created by the author of this thesis using the original data and was not included in the publication [29].

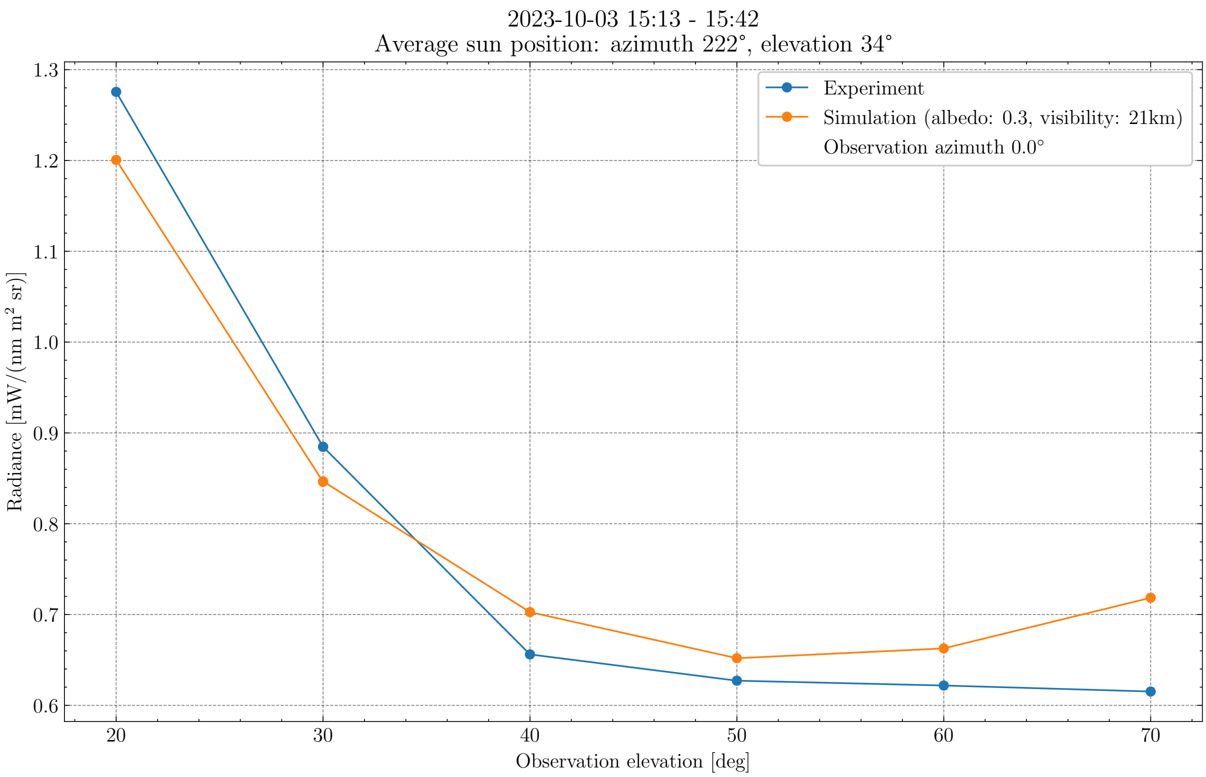

Figure 3.12: Reconstructed result of a BGL measurement during daylight at 1550 nm with clear sky conditions on the RAC rooftop at the campus of the University of Waterloo, Canada, with simulation results utilizing the same settings described in Figure 3 in [29].

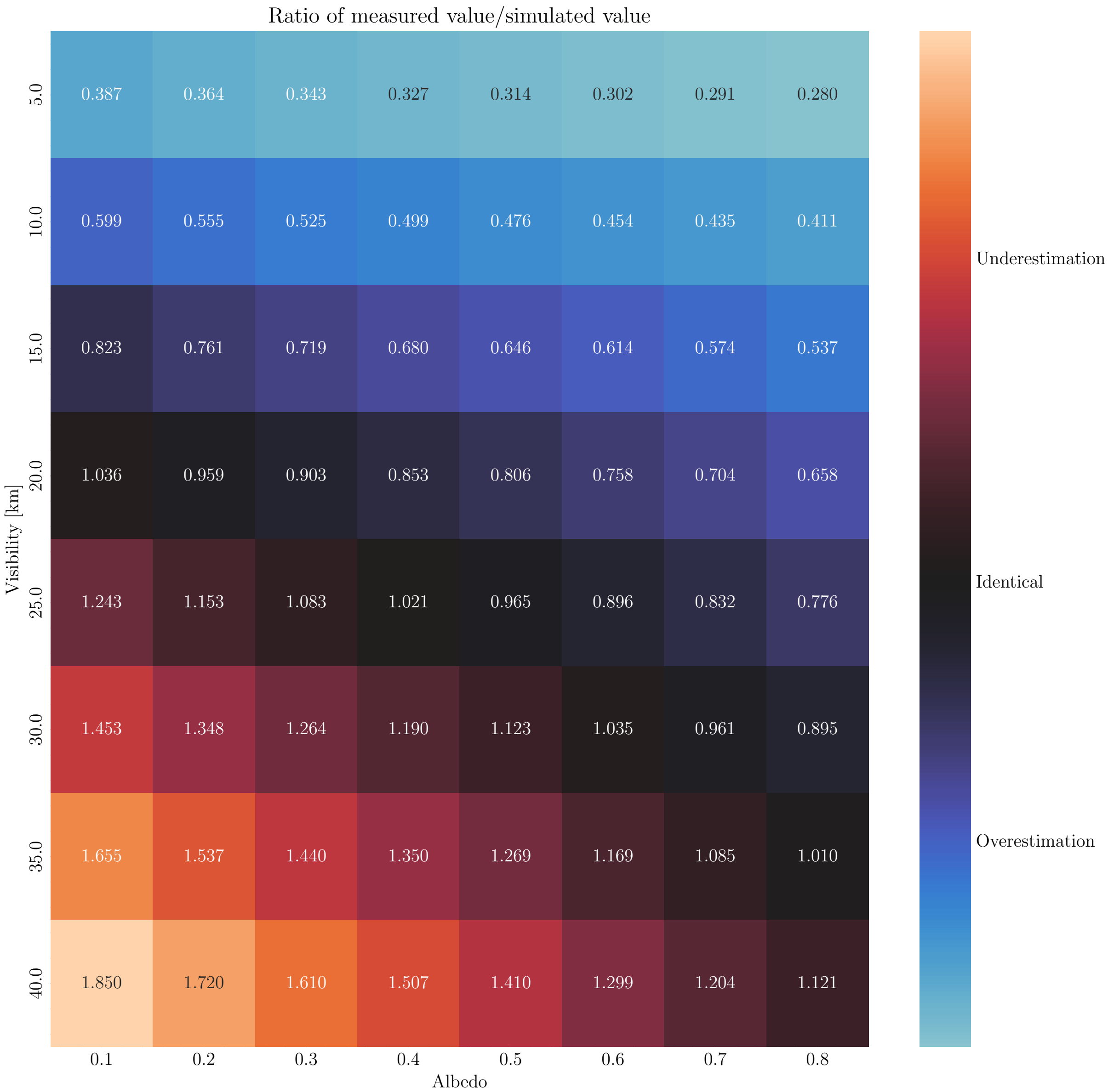

Figure 3.13: Median ratio between measured and simulated radiances for the 0° azimuth measurement series in Waterloo (03.10.2023) from [29] with different albedo and visibility settings. Each block represents a median of all ratios across the different measurement positions. Multiple combinations can be identified that reach ratios of almost one, expected to generated simulations matching the empirical data. The simulation settings are identical to the settings described in Figure in [29], but with varying albedo and visibility.

Chapter 4

Radiative Transfer for background light simulations

The foundation of BGL simulations, as illustrated in Figure 3.12 and 3.10, is the the radiative transfer in the Earth's atmosphere. To predict BGL induced by any source, the radiative transfer equation (RTE) must be solved for a given source spectrum with an adequate atmospheric description. In the following sections, the RTE is derived (see Section 4.1), simplified (see Section 4.2) and solvers and software tools (see Sections 4.3 and 4.4) to solve the RTE are presented.

4.1 Derivation of the radiative transfer equation

For simplicity, the RTE is derived phenomenologically, following the methodology of Wendisch and Yang on pages 149 ff [77]. It has been demonstrated in the works of [45, 46, 47, 73] that it can also be derived from Maxwell's equations including polarization.
The phenomenological approach is similar to derivations in fluid dynamics. In case of the RTE a 6D volume element ($\mathrm{d}^3V\mathrm{d}^2\Omega\mathrm{d}\lambda$) and the change of the photon number is considered. This volume element is linked to the spectral photon density function ($\xi_\lambda(\vec{r},\hat{s},t)$) and number of photons (n_{ph}) by

$$\xi_\lambda(\vec{r},\hat{s},t) = \frac{\mathrm{d}^6 n_{\mathrm{ph}}(\vec{r},\hat{s},t)}{\mathrm{d}^3V\mathrm{d}^2\Omega\mathrm{d}\lambda} \tag{4.1}$$

The 6D element consist of

1. The 3D spatial volume element $\mathrm{d}^3\mathrm{V}$ centered at $\vec{r}$
2. The solid angle element $\mathrm{d}^2\Omega$ centered around the propagation direction $\hat{s}$
3. The wavelength interval $\mathrm{d}\lambda$

A mathematical description of the change of n_{ph} can be built by adding all individual processes that affect n_{ph}. Those processes include

a) Convergence due to photon stream through the volume element

b) Losses due to absorption

c) Losses due to scattering events

d) Gains due to scattering events

e) Gains due to emissions

Photon stream This term classifies the continuous flow to radiation through the volume element. Therefore, it is described by the stream into the volume element minus the stream out of the element for all three spatial dimensions (x,y,z). Using the gradient operator and the speed of light the process can be modelled by

$$\left(\frac{\partial \mathrm{d}^6 n_{\mathrm{ph}}(\vec{r},\hat{s},t)}{\partial t}\right)_{\mathrm{stream}} = -c\cdot\hat{s}\cdot\left(\boldsymbol{\nabla}\xi_\lambda(\vec{r},\hat{s},t)\right)\,\mathrm{d}^3V\mathrm{d}^2\Omega\mathrm{d}\lambda \tag{4.2}$$

Absorption losses Within the volume element, photons may be absorbed by particles, representing the primary loss mechanism. In most atmospheric models, absorption and scattering properties within the medium are assumed to be stationary and thus time-independent. To quantify the effect the total number of photons is multiplied with the probability of absorption, which is characterized by the absorption coefficient $\beta_{\mathrm{abs}}(\lambda,\vec{r})$.

$$\left(\frac{\partial \mathrm{d}^6 n_{\mathrm{ph}}(\vec{r},\hat{s},t)}{\partial t}\right)_{\mathrm{abs}} = -\xi_\lambda(\vec{r},\hat{s},t)\cdot\beta_{\mathrm{abs}}(\lambda,\vec{r})\cdot c\;\mathrm{d}^3V\mathrm{d}^2\Omega\mathrm{d}\lambda \tag{4.3}$$

Scattering losses Similar to the absorption term, scattering events can remove a photon from the volume element by changing the propagation direction. The mathematical treatment is nearly identical to the absorption, with the exception scattering coefficient $\beta_{\mathrm{sca}}(\lambda,\vec{r})$ replacing the absorption coefficient. This is formally expressed by

$$\left(\frac{\partial \mathrm{d}^6 n_{\mathrm{ph}}(\vec{r},\hat{s},t)}{\partial t}\right)_{\mathrm{sca,loss}} = -\xi_\lambda(\vec{r},\hat{s},t)\cdot\beta_{\mathrm{sca}}(\lambda,\vec{r})\cdot c\;\mathrm{d}^3V\mathrm{d}^2\Omega\mathrm{d}\lambda \tag{4.4}$$

Scattering gains In contrast to absorption, which solely represents a loss mechanism, scattering can also introduce gains. A photon may either scatter out of the initial propagation direction ($\hat{s}\to\hat{s}'$) resulting in loss, or scatter into from an arbitrary direction into the specific propagation direction ($\hat{s}'\to\hat{s}$), resulting in gain. To account for all possible directions $\hat{s}'$, the expression must be integrated over all $\hat{s}'$. The probability of respective scattering events is given by a phase function $\mathcal{P}(\lambda,\vec{r},\hat{s}',\hat{s})$. The gain term is given by

$$\left(\frac{\partial \mathrm{d}^6 n_{\mathrm{ph}}(\vec{r}, \hat{s}, t)}{\partial t}\right)_{\mathrm{sca,gains}} = c \cdot \beta_{\mathrm{sca}}(\lambda, \vec{r}) \int \frac{\mathcal{P}(\lambda, \vec{r}, \hat{s}', \hat{s})}{4\pi} \xi_\lambda(\vec{r}, \hat{s}, t)\ \mathrm{d}\hat{s}'\ \mathrm{d}^3 V \mathrm{d}^2\Omega \mathrm{d}\lambda \quad (4.5)$$

Emission gains Emission of electro-magnetic radiation takes place through various means such as e.g. black body radiation. Mathematically, all sources together are quantified by a source coefficient $j_{\mathrm{emi},\lambda}(\vec{r}, \hat{s}, t)$. The equation describing the effect is given by

$$\left(\frac{\partial \mathrm{d}^6 n_{\mathrm{ph}}(\vec{r}, \hat{s}, t)}{\partial t}\right)_{\mathrm{emi}} = j_{\mathrm{emi},\lambda}(\vec{r}, \hat{s}, t)\ \mathrm{d}^3 V \mathrm{d}^2\Omega \mathrm{d}\lambda \quad (4.6)$$

Adding equations 4.2 - 4.6 yields the photon budget equation which can be substituted into equation 4.1. This equation can be expressed in terms of the spectral radiance $L_\lambda(\vec{r}, \hat{s}, t)$, which is related to the spectral photon density by

$$\xi_\lambda(\vec{r}, \hat{s}, t) = L_\lambda(\vec{r}, \hat{s}, t) \frac{\lambda}{h \cdot c^2} \quad (4.7)$$

In 3D the time depended scalar RTE in terms of the spectral radiance is expressed by

$$\begin{aligned} \frac{1}{c}\frac{\partial L_\lambda(\vec{r}, \hat{s}, t)}{\partial t} + \hat{s} \cdot \nabla L_\lambda(\vec{r}, \hat{s}, t) = &- \beta_{\mathrm{ext}}(\lambda, \vec{r}) L_\lambda(\vec{r}, \hat{s}, t) \\ &+ \beta_{\mathrm{sca}}(\lambda, \vec{r}) \int \frac{\mathcal{P}(\lambda, \vec{r}, \hat{s}', \hat{s})}{4\pi} I_\lambda(\vec{r}, \hat{s}, t) \mathrm{d}\hat{s}' \\ &+ J_{\mathrm{emi},\lambda}(\vec{r}, \hat{s}, t) \end{aligned} \quad (4.8)$$

4.2 Simplifications of the radiative transfer equation

During this phenomenological derivation, a simplification was already considered, by dropping the polarization dependency. It is common to only consider the stationary 3D RTE, i.e. $\frac{\partial}{\partial t} = 0$, given by

$$\begin{aligned} \hat{s} \cdot \nabla L_\lambda(\vec{r}, \hat{s}) = &- \beta_{\mathrm{ext}}(\lambda, \vec{r}) L_\lambda(\vec{r}, \hat{s}) \\ &+ \beta_{\mathrm{sca}}(\lambda, \vec{r}) \int \frac{\mathcal{P}(\lambda, \vec{r}, \hat{s}', \hat{s})}{4\pi} I_\lambda(\vec{r}, \hat{s}') \mathrm{d}\hat{s}' \\ &+ J_{\mathrm{emi},\lambda}(\vec{r}, \hat{s}) \end{aligned} \quad (4.9)$$

In the next step, the geometry is chosen. In atmospheric science, Cartesian or spherical geometry are typically employed [42]. In both geometries, the direction of radiation is described by the azimuths angle (ϕ) and zenith angle (θ). When utilizing solvers such as the DISORT, it is advantageous to use the cosine of the zenith angle, defined as $\mu = \cos\theta$. This substitution enables further simplifications (more in section 4.3.1). The choice of geometry dictates the expansion of the streaming term $\hat{s}\boldsymbol{\nabla}$. For Cartesian systems, the plane-parallel geometry is frequently applied. This approximation is valid, as long as horizontal gradients in the x and y directions are negligible, assuming the atmosphere is horizontally homogeneous [42, 77]. Under these assumptions the following approximations hold

$$\hat{s} \cdot \boldsymbol{\nabla} = \cos(\phi)\sqrt{1-\mu^2}\frac{\partial}{\partial x} + \sin\phi\sqrt{1-\mu^2}\frac{\partial}{\partial y} + \mu\frac{\partial}{\partial z} \approx \mu\frac{\partial}{\partial z} \tag{4.10}$$

In spherical geometry the z has to be exchanged for r, which is a suitable approximations for solar zenith angles less than 90 degrees [68]. Inserting equation 4.10 into equation 4.9, replacing all vector quantities $\vec{r}$ with z and expressing the propagation directions $\hat{s}$ and $\hat{s}'$ in terms of μ and ϕ yields the following form of the RTE

$$\begin{aligned} \mu\frac{\partial L_\lambda(z,\mu,\phi)}{\partial z} =& -\beta_{ext}(\lambda,z)L_\lambda(z,\mu,\phi) \\ &+ \frac{\beta_{sca}(\lambda,z)}{4\pi}\int_0^{2\pi}\int_{-1}^{1}\mathcal{P}(\lambda,z,\mu,\phi,\mu',\phi')L_\lambda(z,\mu',\phi')\mathrm{d}\phi'\mathrm{d}\mu' \\ &+ J_{\mathrm{emi},\lambda}(z,\mu,\phi) \end{aligned} \tag{4.11}$$

The final step introduces the single-scattering albedo $\omega(\lambda, z)$ (see Equation 4.12) and the emission source function $J_{\mathrm{emi},\lambda}(z,\mu,\phi)$ (see Equation 4.13). Expressing the emission source function with the single-scattering albedo and dividing both sides of equation 4.11, yields the 1D monochromatic RTE in plane-parallel geometry 4.14.
In most applications the frequency of the propagating light is assumed constant, as inelastic processes such as Raman scattering play only a minor role, the wavelength dependencies often are omitted. If a spherical geometry is applied the coordinate z in equation 4.14 is exchanged for r. Furthermore, equation 4.14 is frequently expressed in terms of the optical depth τ (see Equation 4.15). Applying this transformation leads to the more standard form of the RTE (see Equation 4.16)[42].

$$\omega(z) = \omega(\lambda, z) = \frac{\beta_{\mathrm{sca}}(\lambda,z)}{\beta_{\mathrm{ext}}(\lambda,z)} = \frac{\beta_{\mathrm{sca}}(\lambda,z)}{\beta_{\mathrm{sca}}(\lambda,z)+\beta_{\mathrm{abs}}(\lambda,z)} \tag{4.12}$$

$$J_{\mathrm{emi},\lambda} = \beta_{\mathrm{abs}}(\lambda,z)B[T(z)] \tag{4.13}$$

$$
\begin{aligned}
-\frac{\mu}{\beta_{\text{ext}}(z)}\frac{\mathrm{d}L(z,\mu,\phi)}{\mathrm{d}z} &= L(z,\mu,\phi) \\
&\frac{\omega(z)}{4\pi}\int_0^{2\pi}\int_{-1}^{1}\mathcal{P}(z,\mu,\phi,\mu',\phi')L(z,\mu',\phi')\mathrm{d}\phi'\mathrm{d}\mu' \\
&-(1-\omega(z))B[T(z)]
\end{aligned}
\tag{4.14}
$$

$$
\begin{aligned}
\tau &= \int_z^{\infty}\beta_{\text{ext}}(\lambda,z')\mathrm{d}z' \\
\mathrm{d}\tau &= \beta_{\text{ext}}(\lambda,z)\mathrm{d}z
\end{aligned}
\tag{4.15}
$$

$$
\begin{aligned}
-\mu\frac{\mathrm{d}L(\tau,\mu,\phi)}{\mathrm{d}\tau} &= L(\tau,\mu,\phi) \\
&-\frac{\omega(\tau)}{4\pi}\int_0^{2\pi}\int_{-1}^{1}\mathcal{P}(\tau,\mu,\phi,\mu',\phi')L(\tau,\mu',\phi')\mathrm{d}\phi'\mathrm{d}\mu' \\
&-(1-\omega(\tau))B[T(\tau)]
\end{aligned}
\tag{4.16}
$$

4.3 Solving the radiative transfer equation

Solving Equation 4.14 is a complex task, as scattering processes transform the problem into an integro-differential equation, which posses no analytical solution [69]. A common strategy employed to solve such equations is the discrete-ordinate method. This approach eliminates the integrals, to derive a set of coupled ordinary differential equations (see Equation 4.23). The strategy is utilized by the well-known Discrete Ordinate Radiative Transfer solver (DISORT) developed by Stamnes et al. [67]. The explanation of DISORT in Section 4.3.1 is based on the documentation of methodology in [67].
Alternatively, a statistical Monte-Carlo method can be applied . In the context of radiative transfer, a specific number of photons are traced through the atmosphere, with all interactions, such as scattering and absorption, being modelled throughout its trajectory [77]. This method is implemented in the Monte Carlo code for the physically correct tracing of photons in cloudy atmospheres (MYSTIC) by Bernhard Mayer (see Section 4.3.2) [41, 43].

4.3.1 DISORT

To solve the integro-differential Equation 4.16, the radiance field is split into a direct part I_{dir} and a diffuse part I_{diff} with

$$L = L_{\text{dir}} + L_{\text{diff}} \tag{4.17}$$

The solution for the direct component is trivial; given by the Beer-Lambert-Bouguer law for a parallel beam with intensity I_0 at the top of atmosphere (TOA) and initial position μ_0, ϕ_0 (see Equation 3b in [67]).

$$L_{dir} = L_0 \cdot \mathrm{e}^{-\tau/\mu_0}\, \delta(\mu - \mu_0)\, \delta(\phi - \phi_0) \tag{4.18}$$

This solution modifies Equation 4.16 by adding a new "source term" due to in-scattering from the direct beam (see Equation 4.19). In the following equations the subscript for the diffuse component is dropped.

$$\begin{aligned}
-\mu \frac{\mathrm{d}L(\tau,\mu,\phi)}{\mathrm{d}\tau} &= L(\tau,\mu,\phi) \\
&- \frac{\omega(\tau)}{4\pi} \int_0^{2\pi} \int_{-1}^{1} \mathcal{P}(\tau,\mu,\phi,\mu',\phi') L(\tau,\mu',\phi') \mathrm{d}\phi' \mathrm{d}\mu' \\
&- (1-\omega(\tau)) B[T(\tau)] \\
&- \frac{\omega(\tau) I_0}{4\pi} \mathcal{P}(\tau,\mu,\phi,\mu_0.\phi_0) \mathrm{e}^{-\tau/\mu_0}
\end{aligned} \tag{4.19}$$

The objective is to eliminate any integrals to simplify the differential equation. It is assumed that the scattering phase function solely depends on the angle between the incoming and scattered beams, such that $\mathcal{P}(\tau,\mu,\phi,\mu',\phi') \to \mathcal{P}(\tau,\cos\Theta)$. Consequently, the scattering phase function is expanded as a series of 2M Legendre polynomials. After applying addition theorem for spherical harmonics, the full expansion is expressed by

$$\mathcal{P}(\tau,\cos\Theta) = \sum_{l=0}^{2M-1} (2l+1) g_l(\tau) \left\{ P_l(\mu) P_l(\mu') + 2 \sum_{m=1}^{l} \Lambda_l^m(\mu) \Lambda_l^m(\mu_0) \cos m(\phi - \phi') \right\} \tag{4.20}$$

where $g_l(\tau)$ denotes the normalization coefficient of the Legendre polynomials and Λ_l^m represents the normalized Legendre polynomials.

Similar to the scattering phase function, the radiance is likewise expanded using a Fourier series in ϕ

$$L(\tau,\mu,\phi) = \sum_{m=0}^{2M-1} L^m(\tau,\mu)cos(m(\phi_0-\phi)) \tag{4.21}$$

Substituting Equations 4.20 and 4.21 into Equation 4.19 yields 2M independent integro-differential equations (4.22), which are decoupled from ϕ. The integral over μ' is approximated using a quadrature sum such as e.g. a Gaussian quadrature rule [67]. This transformation results in a set of 2N coupled differential equations with non-constant coefficients, commonly referred to as 2N-stream approximation. The 2N originates from the quadrature sum, where each quadrature angle μ_i represents a "stream" 4.23.
To obtain an analytical solution, DISORT discretizes the medium into multiple homogeneous layers, solving the equations 4.23 for every layer individually. Each layer may posses individual τ,ω and $\mathcal{P}$, depending on the vertical inhomogeneity of the medium . Numerically, the solution reduces to solving an eigenvalue problem. The angle ϕ is only used one during the final construction of the solution when explicit radiance values are calculated [67].

$$\begin{aligned}
-\mu\frac{\mathrm{d}L^m(\tau,\mu)}{\mathrm{d}\tau} =& L^m(\tau,\mu) \\
&- \frac{\omega(\tau)}{2}\int_{-1}^{1}\mathrm{d}\mu' \sum_{l=m}^{2M-1}(2l+1)g_l(\tau)\Lambda_l^m(\mu)\Lambda_l^m(\mu')L^m(\tau,\mu') \\
&- \delta_{m0}(1-\omega(\tau))B[T(\tau)] \\
&- \frac{\omega(\tau)L^0}{4\pi}(2-\delta_{m0})\sum_{l=m}^{2M-1}(2l+1)g_l(\tau)\Lambda_l^m(\mu)\Lambda_l^m(\mu_0)\mathrm{e}^{-\tau/\mu_0}
\end{aligned} \tag{4.22}$$

$$\begin{aligned}
-\mu_i\frac{\mathrm{d}L^m(\tau,\mu_i)}{\mathrm{d}\tau} =& L^m(\tau,\mu_i) \\
&- \frac{\omega(\tau)}{2}\sum_{j=-N}^{N}\mathrm{w}_j \sum_{l=m}^{2M-1}(2l+1)g_l(\tau)\Lambda_l^m(\mu_i)\Lambda_l^m(\mu_j)L^m(\tau,\mu_j) \\
&- \delta_{m0}(1-\omega(\tau))B[T(\tau)] \\
&- \frac{\omega(\tau)L^0}{4\pi}(2-\delta_{m0})\sum_{l=m}^{2M-1}(2l+1)g_l(\tau)\Lambda_l^m(\mu_i)\Lambda_l^m(\mu_0)\mathrm{e}^{-\tau/\mu_0}
\end{aligned} \tag{4.23}$$

4.3.2 MYSTIC

The inner workings of the algorithm have been thoroughly described by Bernhard Mayer in [43] and serve as the template for the following explanation of the algorithm.
In contrast to DISORT, MYSTIC does not aim to solve the RTE directly, but rather simulates the propagation of numerous photons through the atmosphere. This approach allows easier incorporation of complex processes and features, such as clouds that vary rapidly in time and space, or complex surface structures.
The general procedure in MYSTIC can be be divided into the following steps

(i) Generation of photons and determination of initial conditions (position at TOA, initial direction)

(ii) Calculation of optical thickness

(iii) Propagation of photons according to optical thickness calculated in (ii) and directions calculated in (i),(iv) or (v)

(iv) Determination of the effects of absorption and scattering (updating directions and photon weights)

(v) Evaluation of surface interactions (updating directions and photon weights)

(vi) Calculation of the optical properties of interest

The calculation of individual optical properties (step vi) occurs only after the trajectories of all photons have been determined and the photons have been counted. A trajectory reaches its end once the traced photon leaves at the TOA or is absorbed by the surface.
In the following, the procedure of random number draws in MYSTIC is explained. Afterwards each step (i) - (vi) is explained in greater detail.
Random number draw During steps (i) - (v) random values must be calculated for several properties, such as the optical thickness in step (ii). This calculation is conducted following Von Neumann's Golden rule of Sampling[1]. For a given probability density $p(x)$ the cumulative probability density $P(x)$ is calculated as follows

$$P(x) = \int_0^x p(x')\mathrm{d}x' \tag{4.24}$$

The advantage of using the cumulative density function is that for any interval of equal size the in range of $P(x)$ is identical. For example, $P(x) \in [0.1, 0.2]$ is equal to the probability

[1] More commonly known under the name *inverse transform sampling*.

of as $P(x) \in [0.6, 0.7]$. Afterwards the inverse of the cumulative probability density is calculated as

$$x = P^{-1}(\rho) \tag{4.25}$$

For a given probability density, it is possible to generate random values for x by drawing a uniformly distributed random number ρ from the interval (0,1). An example draw is depicted in Figure 4.1.

(i) Photon generation First, photons have to be generated based on a specific source, such as the solar spectrum (irradiance at TOA). Under the assumption that the atmosphere is illuminated homogeneously by the Sun,each photon is assigned a random location in the x-y plane at the TOA. The initial direction is defined by the solar azimuth and zenith angles and are assumed to be constant over the whole x-y plane.

(ii) Calculating the optical thickness To determine the distance a photon travels,before any interaction occur, a path length is calculated. This path is determined by the extinction probability, which follows the Lambert-Beer's law

$$p_{\text{ext}}(\tau) = p_{\text{surv}}(\tau) = \mathrm{e}^{-\tau} \tag{4.26}$$

A random τ is sampled by using the technique described above. The inverse cumulative probability density is given by equation 4.27. Figure 4.1 illustrates an example draw of 10^6 randomly values of τ , which align perfectly with the probability described by equation 4.26.

$$\begin{aligned} P_{\text{ext}}(\tau) &= \int_0^{\tau} \mathrm{e}^{-\tau'} \mathrm{d}\tau' \\ \tau(\rho) &= P_{\text{ext}}(\tau)^{-1} - \ln(1-\rho) \end{aligned} \tag{4.27}$$

(iii) Photon propagation Following the calculation of τ, the distance which a photon travels through the grid (typically rectangular) is determined by integrating the extinction coefficient along its trajectory. The direction of the trajectory is defined by the azimuth and zenith angles, which either have been derived from an previous event or are equal to the initial conditions. Once the photon arrives at its path length determined earlier, its position and cell index is saved and the next phase is initiated.

(iv) Interaction phase Each cell of the grid posses individual optical properties that determine the future of photons arriving in each cell. A photon may either be absorbed or scattered into a new direction.

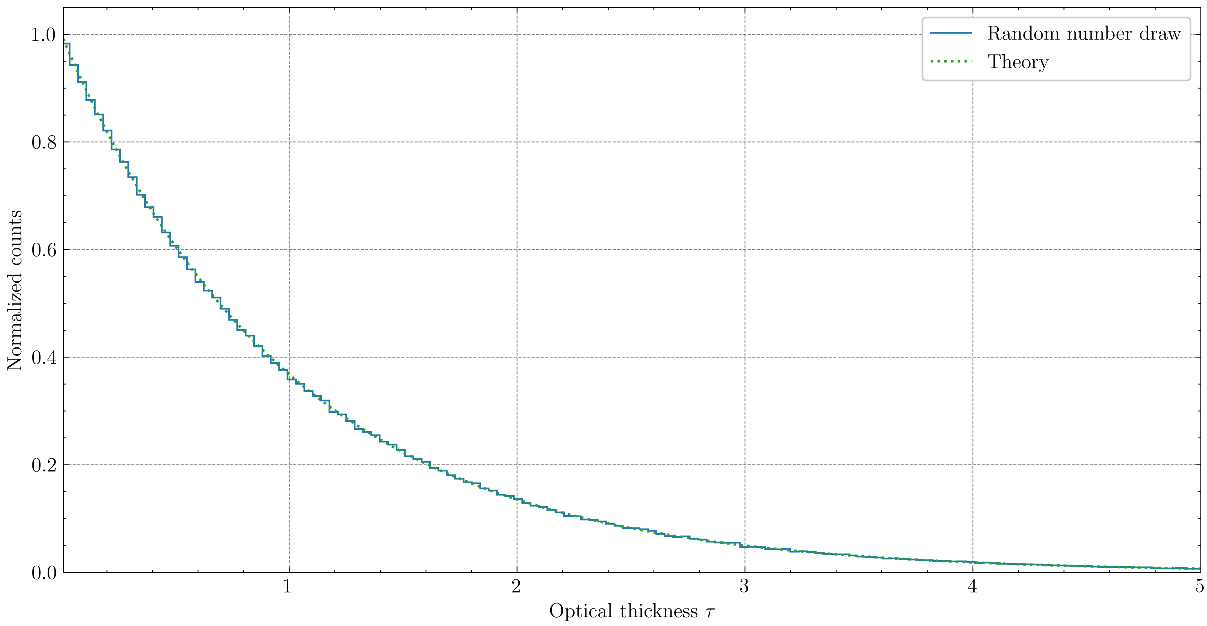

Figure 4.1: Random numbers in MYSTIC are drawn according to the process outlined in 4.3.2. The process is illustrated for the sampling of optical thickness based on the underlying probability density given by the Lambert-Beer's law.

To determine the new direction, a random number draw is performed using the corresponding probability density for the specific scattering event(e.g. molecule or water droplet scattering).

To optimize calculation, absorption is not modelled as the photon being discarded. In this naive case, the a significant computational time would be required, due to the loss of many photons which not attribute to the final photon count. Instead, photons weights are introduced at the creation of each photon. This weight is decreased between between interactions according to the Lambert Beer law. By modelling absorption continuously, the only interaction that occurs are scattering events, that have to be modelled differently once the surface is reached.

(v) Surface interaction Upon reaching the surface, a photon is either absorbed or reflected. In this context, absorption does terminates the journey of a photon and it contributes to the photon count. If the photon is reflected, the reflection is either modelled as a Lambertian surface (isotropic reflection with constant albedo) or by a Bidirectional Reflectance Distribution Function (BRDF). The latter allows for calculation of the new direction depending on the incident direction. As for absorption processes, the reflection only occurs with a certain probability and thus the photon weights are adjusted by it before the cycle starts at step (ii) again (if they are not absorbed).

(vi) Calculating optical properties After all photon trajectories terminated, optical properties, such as the surface irradiance or radiance, are calculated. The specific methodologies can be found in [43]. Depending on the property different approaches are utilized using the counted photons and their weights. Generally, with a higher photon number the accuracy of MYSTIC is increased following

$$\frac{\sigma}{\mu} = \sqrt{\frac{N - pN}{pN^2}} \tag{4.28}$$

where p is the probability of the transmission through the atmosphere and N the number of photons traced. However, increasing the photon number does increases not only the accuracy, but also the computational costs, scaling with $\mathcal{O}(n^2)$.

4.4 Software tools for radiative transfer

To solve the RTE, several software packages and tools can be utilized such as library for radiative transfer (libRadtran) (current version 2.0.6)[20, 40] and MODTRAN (Moderate resolution atmospheric Transmission) [9, 10]. In this thesis, libRadtran is employed (see Section 4.4.1).
For daytime simulations, the source irradiance spectrum is given by the *TSIS-1 HSRS spectrum* [15]. This spectrum is identical to the solar irradiance spectrum that is used in the *LIME toolbox* (current version 0.8) to calculate lunar irradiance spectra for nighttime simulations (see Section 4.4.2).

4.4.1 libRadtran

libRadtran is a publicly available software package comprising data sets and tools, written in C and Fortran, designed to address various problems regarding atmospheric radiation. Its core tool is *uvspec*, a radiative transfer model used to calculate radiation fields within Earth's atmosphere. The model is suitable for applications requiring radiation analysis across the spectral range from 120 nm to 100 µm. The *uvspec* tool is invoked via the command line utilizing an ASCII input file. Upon completion of the calculations, an output file is generated containing optical properties determined by the parameters specified in the input file. If the input file includes a pointing direction of a sensor, radiances can be calculated explicitly; otherwise *uvspec* provides upward and downward diffuse and direct irradiances by default [40].
Figure 4.2 illustrates the structure of the uvspec model. The atmospheric description and optical properties rely on the built-in data sets, but can also be customized by providing custom files. For BGL simulations, the most critical input parameters are the source file, the source position, the choice of aerosol and atmospheric model and the sensor location.

The source file is either a spectrum of the Moon calculated using the *LIME toolbox*, or the *TSIS-1 HSRS spectrum* for the Sun [15]. For each measurement, the source location is calculated, while the sensor location is provided by the chosen telescope position.
Built-in datasets are utilized for the atmospheric and the aerosol models. The latter is based on the model by Eric Shettle [63], with default properties consisting of a rural type of aerosols below 2 km, background aerosols above 2km, spring-summer conditions, and a visibility of 50 km, which can be adjusted in the input file. The atmospheric models provided by libRadtran are based on the works of Anderson et al. [1], from which the US-standard is selected by default. To model the absorptive properties of the gases in the atmosphere, the fine *REPTRAN* parameterization (with width of 1 cm^{-1}) is employed [21].

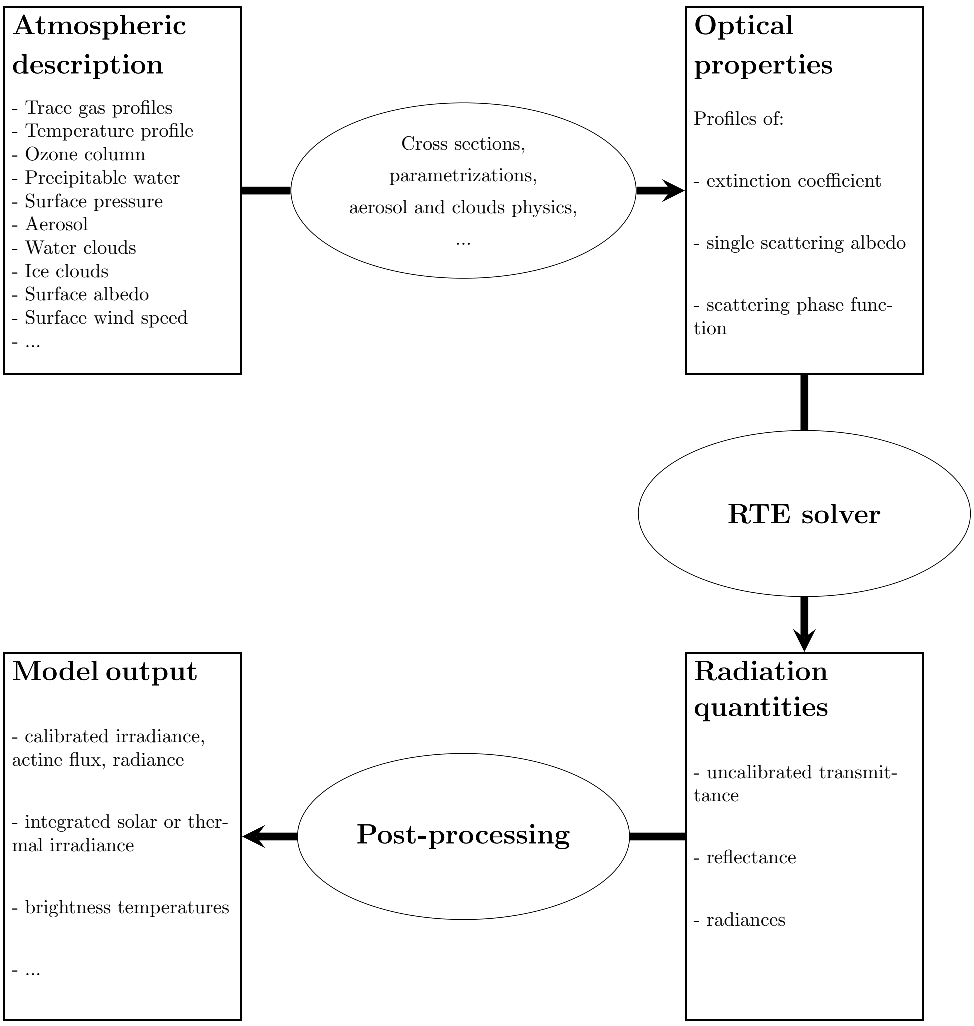

Figure 4.2: Flowchart of the uvspec model structure. Graphics based on Figure 1 in [40].

4.4.2 LIME toolbox

While numerous models of the solar irradiance spectrum are available, the lunar irradiance spectrum presents greater complexity due to variations introduced by the changing Sun-Earth-Moon geometry (see Figure 4.3). The Lunar Irradiance Model of the European Space Agency (LIME) is based on the widely used ROLO (Robotic Lunar Observatory) model by Kieffer and Stone [30] and was developed to surpass the latter in accuracy. To achieve this, a CIMEL radiometer equipped with channels at 440 nm, 500 nm, 675 nm, 870 nm, 1020 nm and 1640 nm was employed to observe lunar irradiances at two different locations: the Izana Atmospheric Observatory and the Teide Peak Observatory. Measurements have been taken over the course of over four years totalling 590 lunar observations, forming the basis for the estimation of model parameters [72].

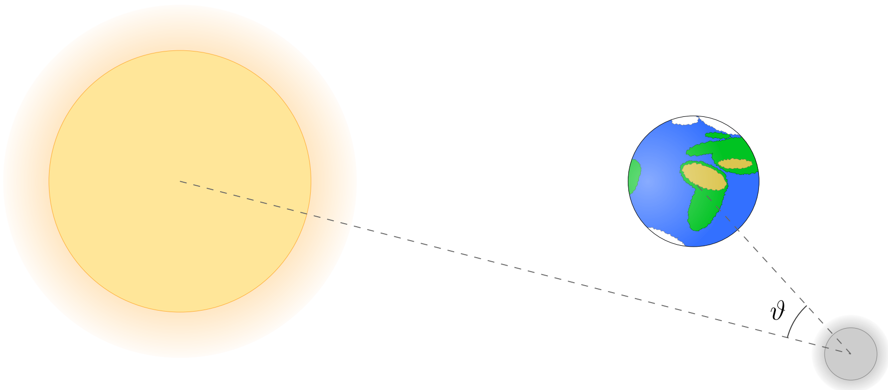

Figure 4.3: Sun-Earth-Moon geometry with Moon phase angle ϑ.

The *LIME toolbox* (hereafter referred to as LIME) is a publicly available software toolbox based on the model. It can be used to calculate lunar irradiance, lunar reflectance, and the degree of linear polarization. To calculate irradiance for a specific location on Earth, the geodetic coordinates (longitude and latitude), altitude, and UTC time must be provided. A significant advantage of LIME is the command-line interface, which, similar to *uvspec*, offers easy integration into a *Python* workflow.

Figure 4.4 depicts three spectra calculated using the graphical user interface of LIME for the location of the OGSOP (Latitude: 11.277 98°E, Latitude: 48.084 76°N Altitude: 650 m). From top to bottom, the error of the model increases significantly. In example (c), the model fails to produce physically meaningful results. LIME only guarantees reliable data for absolute Moon phase angles between 2° and 90°. The Moon phase angle describes the angle between the incident light (Sun → Moon) and the reflected light towards the observer (Moon → Earth). Consequently, the application of LIME for BGL simulations is limited to Moon phases between the waxing half-Moon and waning half-Moon.

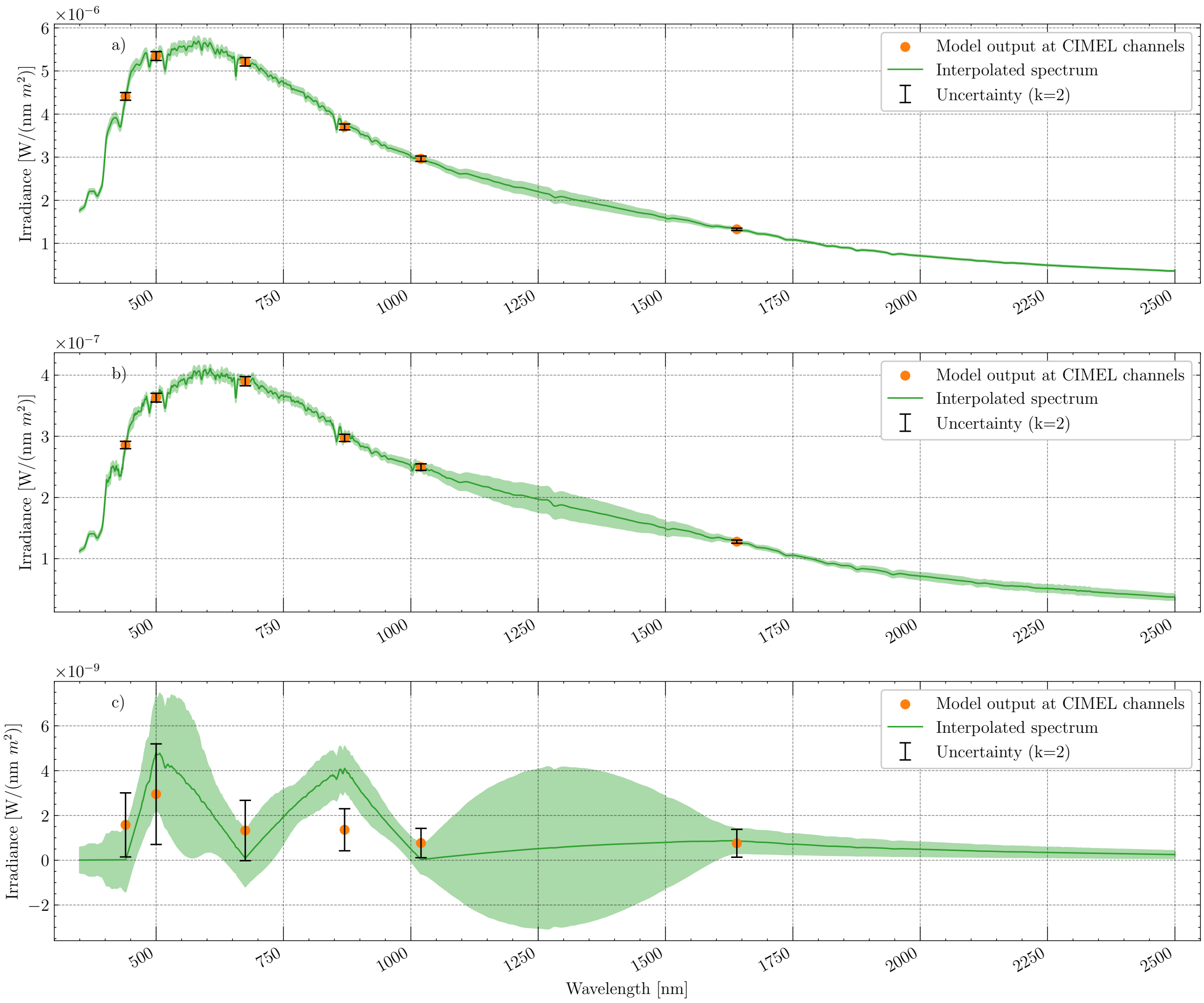

Figure 4.4: Example spectra calculated with LIME. LIME is only reliable if the absolute Moon phase angle is in the window between 2° to 90°. From a) to c) the Moon phase angle increases while simultaneously the uncertainty grows. The Moon phase angles for each calculated spectrum are a) -4.09° b) -94.41° c) -173.33° corresponding to the UTC times a) 23.12.2026 22:00:00 b) 16.12.2026 22:00:00 c) 09.12.2026 09:00:00. The spectra were calculated using the geographic coordinates of the OGSOP (altitude: 650 m, longitude: 11.277 98°E, latitude: 48.084 76°N).

Chapter 5

Converting measurement data

To be able to compare the measurement results shown in Section 9.3, with other setups and simulations utilizing libRadtran, the measured count rates must be converted to radiances. First the measured count rates are converted to the photon rate, the number of photons in front of the employed detector (see Section 5.1). In the second step, these photon rates are used to calculate the setup independent radiance values (see Section 5.2). The derivations follow the internal technical report by multiple colleagues in [26][1]. Furthermore, the description of the count rate dependent SDE is based on the internal report by a colleague [74].

5.1 Converting count rates to photon rates

The count rates that are extracted during measurements do not account for detector specific characteristics, that must be addressed. For the employed SNSPD these effects include:

Detector recovery time (τ_{rec}): Time period during which the detector is less sensitive to incident photons while the bias current recovers (see Section 3.2.1).

Detector dark count rate (R_{dcr}): Counts not caused by BGL.

System detection efficiency (η_{sde}): Photons missed due to e.g. photons not being absorbed by the nanowire or registered by the readout electronics (see Section 3.2.1).

[1] While not acting as a main contributor for the derivation, the author of this work took part in the discussions and initiated the revision of the first iteration of formulas leading to this internal report.

To consider all these, the DCR (R_{dcr}) is subtracted from the signal count rate (R_{sig}) and the difference is divided by the SDE. As mentioned in Section 3.2.1, the SDE has to take the count rate into account if the arrival time of the photons ($\tau_{\mathrm{ph-ph}}$) matches or is smaller than the timescale of τ_{rec}.

$$R_{\mathrm{ph,bgl}} = \frac{R_{\mathrm{sig}} - R_{\mathrm{dcr}}}{\eta_{\mathrm{sde}}(R_{\mathrm{sig}})} \tag{5.1}$$

The recovery process of the SDE for a single nanowire SNSPD, such as employed in the experiment, can be modelled by an exponential sigmoid function (see [56, 74])

$$\eta_{\mathrm{det}}(t) = \frac{\eta_{\mathrm{sde},0}}{1 + \exp\left(-\frac{t-\tau_{\mathrm{rec},50}}{\tau_*}\right)} \tag{5.2}$$

with $\eta_{\mathrm{sde},0}$, the fully recovered SDE, $\tau_{\mathrm{rec},50}$ the time at which 50% of the SDE is reached (50% recovery time) and a fitting parameter τ_*. The latter two are determined by fitting the sigmoid function to a recovery time measurement (see Section 8.2.1).
To express the SDE in terms of the count rate, Equation 5.2 first has to be multiplied by the probability density of two photons arriving, given by a Possonian probability density, to receive the probability density of two detections in terms of t. Integrating this expression under the assumption that $R \cdot t < 1$ yields the probability of a detection in terms of the count rate

$$\begin{aligned} \eta_{\mathrm{sde}}(R) &= \eta_{sde,0} \cdot R \int_0^\infty \exp(-R \cdot t) \cdot \left(1 + \exp\left(-\frac{t-\tau_{\mathrm{rec},50}}{\tau_*}\right)\right)^{-1} \mathrm{d}t \\ &\approx \eta_{sde,0} \cdot \left(\frac{\alpha\pi}{\sin(\alpha\pi)} \cdot \exp(-\alpha\Gamma) - \frac{\alpha}{1-\alpha} \cdot \exp(-\Gamma)\right) \end{aligned} \tag{5.3}$$

with $\alpha = R\tau_*$ and $\Gamma = \frac{\tau_{\mathrm{rec},50}}{\tau_*}$. As long as R remains stable across the detection window, Equation 5.3 can be used to convert the measured R_{sig} and R_{dcr} to $R_{\mathrm{ph,bgl}}$ by applying Equation 5.1 with $\eta_{\mathrm{sde}}(R_{\mathrm{sig}})$ given by Equation 5.3

5.2 Converting photon rates to radiances

The radiance L in units of $\mathrm{mW\,nm^{-1}\,m^{-2}\,sr^{-1}}$ is defined as

$$L = \frac{P}{\Delta\lambda_{\mathrm{eff}} \cdot \Omega_{\mathrm{FOV}} \cdot A_{\mathrm{rx}} \cdot \eta_{\mathrm{sys}}} \tag{5.4}$$

where $\Delta\lambda_{\mathrm{eff}}$ is the effective filter bandwidth, Ω_{FOV} the solid angle field-of-view (FOV) of the receiver, A_{rx} the collecting receiver area, P the measured power in mW and η_{sys} the system efficiency.

Parameters fixed by the experimental setup include the effective filter bandwidth of the dichroic mirror (34.9 nm), the receiver collection area, calculated from the diameter of the primary mirror of the telescope (D_{rx} = 80 cm, see Equation 5.6) and the system efficiency (see Equation 7.1). Using the values of $R_{\mathrm{ph,bgl}}$, calculated according to the procedure outlined in the previous section, the optical power in can be calculated by

$$P = \frac{R_{\mathrm{ph,bgl}} \cdot \mathrm{hc}}{\lambda} \tag{5.5}$$

$$A_{\mathrm{rx}} = \frac{\pi \cdot D_{\mathrm{rx}}^2}{4} \tag{5.6}$$

The solid angle Ω_{FOV} can be expressed via the planar angle FOV (θ_{FOV}) using the small angle approximation [62]

$$\Omega_{\mathrm{FOV}} = 2\pi(1 - \cos\theta_{\mathrm{FOV}}) \approx \pi \cdot \theta_{\mathrm{FOV}}^2 \tag{5.7}$$

As detailed in Section 7.1, the BGL is coupled into a SMF. Within the SMF, light is treated as a Gaussian beam characterized by a beam waist w_0 and a mode field diameter (MFD)[2]. A formula for the divergence angle, which is equivalent to the FOV of the fiber, can be derived using geometric optics provided the following criteria are satisfied:

1. The beam must be diffraction limited.
2. The M^2 beam quality factor must be approximately 1.
3. The optical system must satisfy the paraxial approximation.

The first condition is met when the effective focal length of the system is sufficiently large in comparison to the beam waist and the impact of the central obscuration ratio of the telescope is negligible. Given the effective focal length f_{OGS}= 3865 mm and a central obscuration ratio of 3/8, these conditions are sufficiently met. The second condition is

[2]The mode field diameter is defined as the $1/e^2$ diameter including 86% of the beam power.

fulfilled as quality factor M^2 of a fundamental Gaussian beam, as in the SMF, is close to 1. Condition three typically holds for SMF systems where $f \leq 1\,\mathrm{cm}$ and the beam remains collimated. As the optical system satisfies both, the last condition is met and the approach using geometric optics justified.
The formula for the divergence angle is derived from the geometry illustrated Figure 5.1 and is defined as

$$\tan\theta_{\mathrm{SMF}} \approx \theta_{\mathrm{SMF}} = \frac{w_0}{f} = \frac{\mathrm{MFD}}{2f} \tag{5.8}$$

Incorporating the MFD into the derivation intrinsically accounts for theoretical losses associated with coupling light into a SMF under optimized mode-matching conditions, as the calculation does not incorporate total beam power. Consequently, η_{sys} (see Equation 7.1) excludes contributions of the fiber coupling.
Combining 5.4 - 5.8, substituting $\theta_{\mathrm{FOV}} = \theta_{\mathrm{SMF}}$ and converting the power to mW to match libRadtran's output, yields the final conversion formula for photon rates measured by the SNSPD to radiances at the SMF

$$L_{\mathrm{SMF}} = \frac{R_{\mathrm{ph,bgl}} \cdot \mathrm{hc} \cdot 10^3}{\lambda \cdot \Delta\lambda_{\mathrm{eff}} \cdot \pi \cdot \left(\frac{\mathrm{MFD}}{2f}\right)^2 \cdot \left(\frac{\pi D_{\mathrm{rx}}^2}{4}\right) \cdot \eta_{\mathrm{sys}}} \tag{5.9}$$

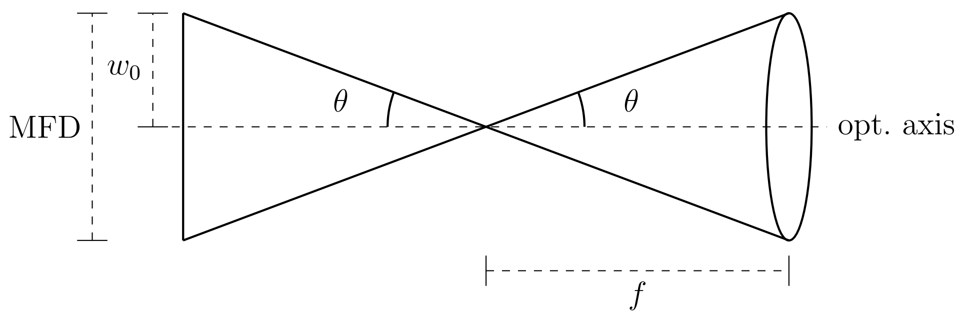

Figure 5.1: The geometry for the deviation of the divergence angle used in Equation 5.8 consists of the SMF on the left, and the focus lens on the right. MFD is the mode field diameter of the optical fiber, w_0 the beam waist and f the (effective) focus length.

Chapter 6

Simulating background light

Simulations offer a complementary tool that, under certain conditions, can aid in predicting BGL. Particularly for daytime operations, simulation tools can provide estimates of the solar radiation observed that align with experimental measurements (see Figure 3.12) under clear-sky conditions [28, 29].
To simulate the observed radiation, the RTE is solved (see Chapter 4) utilizing the software tools libRadtran and LIME, which are presented in Sections 4.4.1 and 4.4.2.
This chapter focuses on the integration of these tools to simulate BGL for measurements with the OGSOP during daytime (see Section 6.2) and nighttime (see Section 6.3).

6.1 Similarities between daytime and nighttime simulations

A fundamental limitation for both daytime and nighttime simulation is imposed by the range of zenith angles covered by *uvspec*. To simplify the RTE, the cosine of the zenith angle μ is used (see Section 4.3.1), which cannot take a value of zero. Hence, simulations are typically restricted to observation zenith angles unequal 90°, or values are slightly shifted to prohibit a zero value.
Another limitation for simulating BGL is the limitation to clear-sky conditions for comparisons between simulations and measurements. Even though it is possible to include clouds in *uvspec* if MYSTIC is chosen as a solver, the clouds need to be characterized with regard to their altitude and water/ice content [40]. This information would need to be measured in real time during BGL measurements, which is not deemed feasible.
As mentioned in Section 4.4.1, the *uvspec* model is invoked by providing an ASCII input file.

With the exception of the source file, the input file requires almost identical parameters to be generated. Some parameters are fixed by the measurement setup, including:

Wavelength: Defined by the center wavelength of the dichroic mirror (see Section 7.1).

Location: Determined by the latitude (°N) and longitude (°E) coordinates of the OGSOP.

Altitude: Specified by the altitude of the OGSOP in meters. In *uvspec*, the altitude sets the lower boundary of the atmosphere.

Telescope position: Determined by the specific measurement (azimuth angle and zenith angle) and essential to calculate explicit radiances.

The location of the OGSOP is frequently used in the backend to convert local times into time-zone-aware datetime objects to ensure that the input requirements of LIME and the *Astropy* package are met. *Astropy* is used to calculate the source position of the Sun and the Moon utilizing the DE440 ephemerides data [52].
Additional parameters that must be specified in the input file include the aerosol season (spring/summer or fall/winter mixture), aerosol haze conditions (rural, urban, maritime, or tropospheric atmospheric constituents type below 2 km), albedo (ranging from 0 to 1), visibility (in km) and the solver.The DISORT solver is employed, with the exception of large source zenith angles. For large zenith angles, MYSTIC provides more accurate results than DISORT even with the pseudospherical corrections applied, as MYSTIC can utilize a full 1D spherical shell atmosphere model [40]. If the MYSTIC solver is selected, the number of traced photons must also be defined.
Individual settings employed for the simulations are outlined in Section C and are referenced upon usage.

6.2 Daytime simulations

Simulating BGL during daytime measurements is equivalent to simulating the radiative transfer of solar radiation through the atmosphere, as the Sun dominates all other BGL sources. Therefore, the solar position and the solar spectrum at the top of atmosphere (TOA) must be defined. For the latter, the *TSIS-1 HSRS spectrum* [15] is utilized[1], while for a given time, the position of the Sun is calculated using the *Astropy* package.

[1]As the *TSIS-1 HSRS spectrum* provides irradiances values in units of $\mathrm{W\,m^{-2}\,nm^{-1}}$, the spectrum must first be converted to the *uvspec* format of $\mathrm{mW\,m^{-2}\,nm^{-1}}$.

To achieve maximum accuracy, simulations should ideally be conducted for each timestamp of a BGL measurement, as the source location changes over the course of the measurement. However, simulating for every individual timestamp for a 10 minute measurement (see Section 7.3.3) would result in 600 simulations for each individual telescope position. Assuming an average computation time of 0.3 s for a simulation with DISORT or2 s with MYSTIC tracing 10^6 photons[2] and a full measurement series of at least seven positions, the simulations would take 21 minutes for DISORT and 140 minutes for MYSTIC. While feasible for an individual simulation run, tuning and testing with new parameters becomes time consuming. Hence, only a subset of timestamps is used for the simulation rather than every individual timestamp.

Figure 6.1 illustrates the change in radiance between consecutive simulations conducted five minutes apart across a full summer and winter day for different observer positions. The most significant change is observed during sunrise and sunset. When simulations are conducted for sunrise or sunset, radiances are simulated for every timestamp.

Outside of these scenarios, the changes are in general higher during summer, when the Sun reaches higher elevations with relative changes reaching values of up to approximately 6%. To minimize the error introduced to the simulations, the time separation must be chosen carefully. To highlight the impact of shorter time separations between consecutive simulations, Figure 6.1 depicts a time period with high relative change in radiance. For separations of 30 s, the expected change over the whole day, excluding sunrise and sunset, is below 0.6%. This value will act as the maximum separation between simulated timestamps.

[2]Both times are based on the tracking the execution time of *uvspec* while running the python wrapper scripts. Execution times have been observed to change slightly depending on the input parameters.

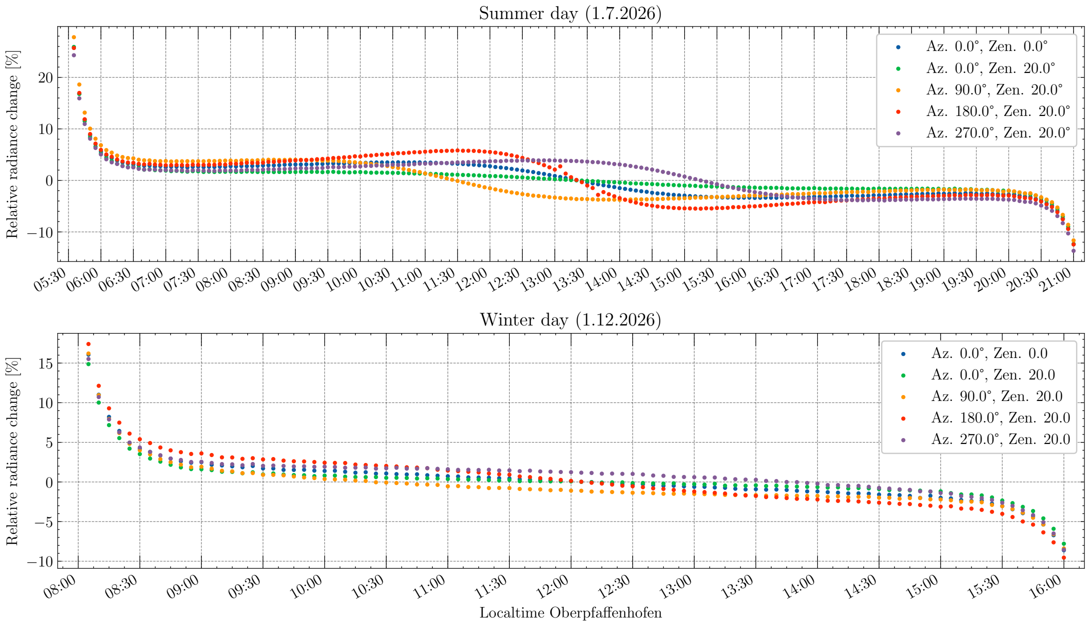

Figure 6.1: Relative changes between consecutive solar radiance simulations during summer and winter with five minutes separation for different observer positions (Az. = azimuth angle, Zen. = zenith angle) are illustrated. The changes peak during sunrise and sunset and vary more in the summer when the Sun rises to higher elevations. The simulation settings are outlined in Section C.4.

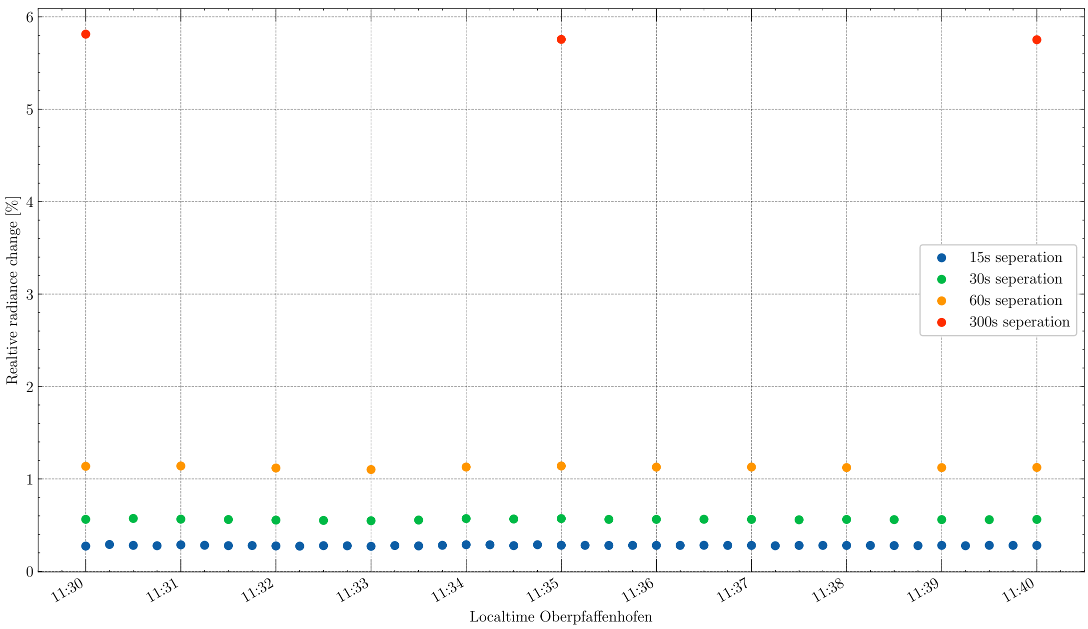

Figure 6.2: Shown are the changes between consecutive solar radiance simulations for the summer scenario in Figure 6.1 over a short time period with varying temporal separations. With decreasing temporal separation, the relative change decrease at the cost of increasing computational time due to more simulations being conducted. The settings are outlined in Section C.4.

The procedure for creating daylight simulations for a BGL measurement is schematically illustrated in Figure 6.3. A simulation function is provided with:

1. The size of the time blocks (less than 30 s).
2. The *TSIS-1 HSRS spectrum* file path.
3. The parsed measurement file that contains the data table and the fixed measurement parameters (wavelength, location, altitude, and telescope position).
4. The additional settings consisting of the aerosol season, aerosol haze, albedo, visibility, solver, and an optional photon number.

Once all parameters are provided, the function splits the measurement into the time blocks with the defined length. Subsequently, the *uvspec* wrapper function is called with the same setting for each block. The *uvspec* wrapper calculates the Sun's position and manages the input and output files and returns the results of the simulation. Theses results are collected by the simulation function and combined once the loop through all blocks is finished. As the simulation results change over the course of a single BGL measurement due to the changing Sun position, the simulation results will always be visualized as error bars to show the range of the simulated radiances.

For a BGL measurement with a duration of 600 s, and a block size of 30 s, this procedure reduces the computation time for a simulation of a whole measurement series (seven individual measurements) by a factor of 30, requiring only 42 s with DISORT and 280 s with MYSTIC. with expected deviations of less than 1%.

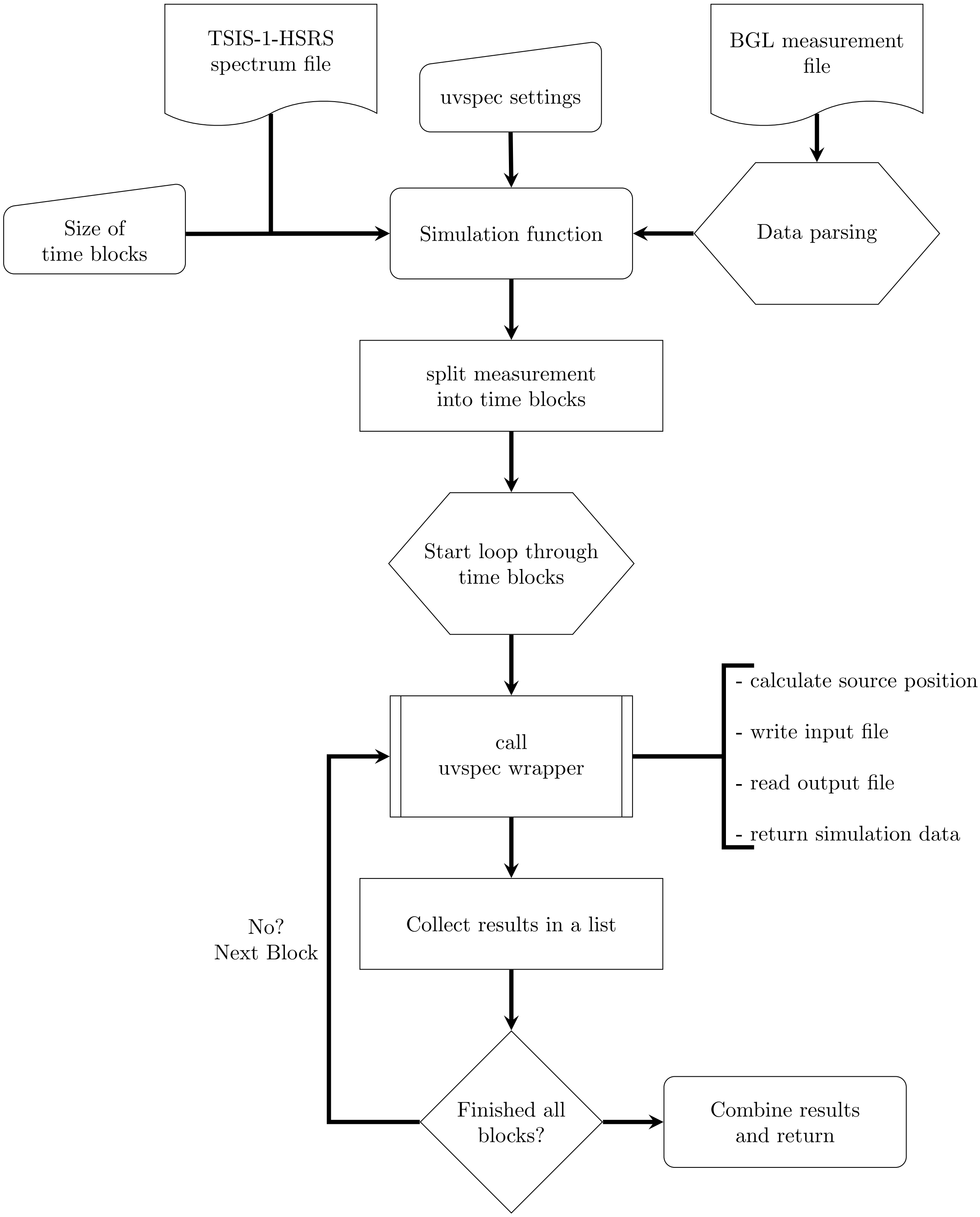

Figure 6.3: Schematic representation of the process of simulating BGL for a daytime measurement. A precise breakdown of the functions inputs is given at the end of Section 6.2. For a full measurement series with multiple observation positions, this procedure is repeated for each observation position. The source position is calculated based on the middle timestamp of the current block.

6.3 Nighttime simulations

Unlike for daytime BGL, which is dominated by primarily one source, nighttime BGL cannot be described by a single dominant source. Instead, anthropogenic light, diffuse and direct contributions from stars and planets, zodiacal light, airglow and diffuse emissions from the galaxy (see Table 3.5) contribute to the measured background light radiation, but are challenging to model without existing site specific measurements. The focus of this thesis will be the simulation of the lunar sky radiance, considering only the Moon as a source for BGL. Using LIME, lunar spectra are calculated and utilized as input for *uvspec*[3].
A major difference between nighttime and daytime simulations is the usage of an individual spectrum for each 10 minute measurement. While for daytime measurements, the *TSIS-1 HSRS spectrum* is applicable for all Sun positions because the spectrum does not change significantly, the Moon only reflects light from the Sun instead of emitting light on its own. Thus, the lunar irradiance spectrum is dependent on the Sun-Earth-Moon geometry, commonly described by the Moon phase angle (see Figure 4.3). The Moon phase angle changes over the course of a period of lunar visibility (moonrise to moonset), with a higher rate of change observed during moonrise and moonset. An example of the phase angle and the rate of change (for a temporal resolution of five minutes) is given in Figure 6.4, starting on the 22.12.2026 with moonrise and ending with moonset on the 23.12.2026[4]. The influence of the changing geometry on the lunar spectrum is illustrated in Figure 6.5. A lunar spectrum calculated on 22.12.2026 at 21:00 acts as the baseline for the deviation calculations. As the position of the Moon deviates from the baseline, the lunar spectrum experiences a deviation of up to approximately 0.8% after a time period of 30 minutes. For the center wavelength of the BGL measurements (1565 nm), the deviation is smaller, at approximately 0.65%. To maintain high accuracy while minimizing computational time, one spectrum is calculated at the middle timestamp of each measurement. For a measurement with the duration of 10 minutes, a spectrum calculated at the middle timestamp has, at most, a temporal separation of five minutes to any given data point. By comparing the highest phase angle change of $\pm 0.055^\circ$ during moonrise and moonset, with the green curve in Figure 6.5, which shows the deviations for a Moon phase angle change of -0.07° relative to the baseline, it is concluded that the error induced by using one lunar spectrum calculated at the middle timestamp should be less than $\pm 0.3\%$. As no measurements were conducted during moonrise or moonset the error is likely even smaller.

[3]To match the irradiance spectrum units of the input files of *uvspec* ($\mathrm{mW\,m^{-2}\,nm^{-1}}$), the output of LIME must first be converted.

[4]These dates were chosen specifically to cover a day when the Moon rises early and sets late, such that high elevations are reached during the time period.

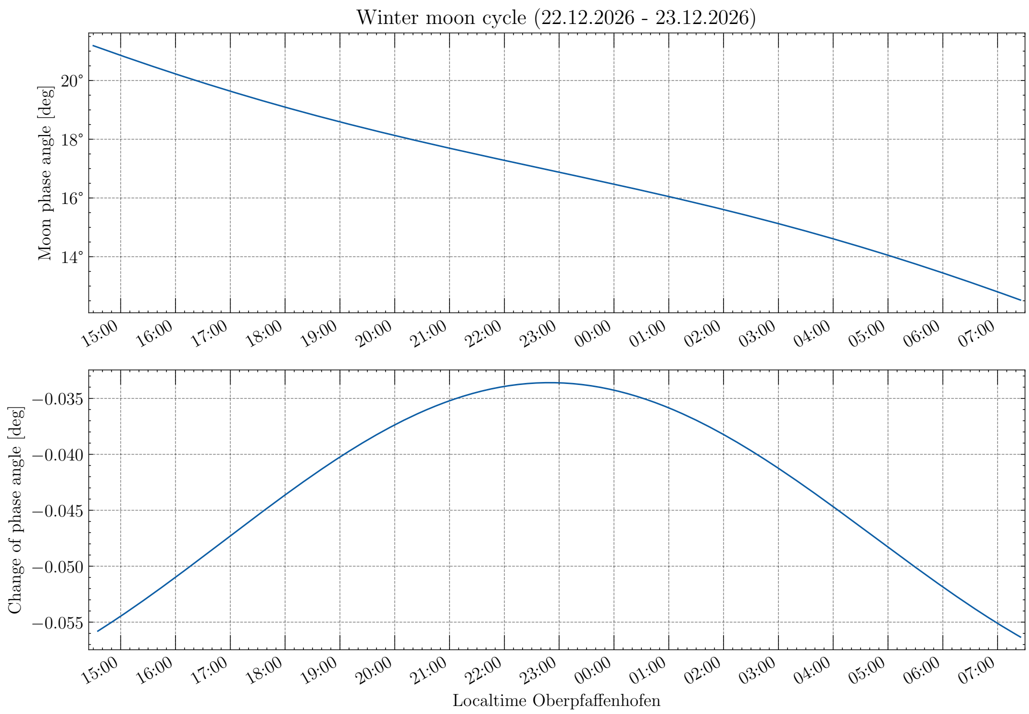

Figure 6.4: Moon phase angle change over a full night. The separation between consecutive Moon position calculations is five minutes.

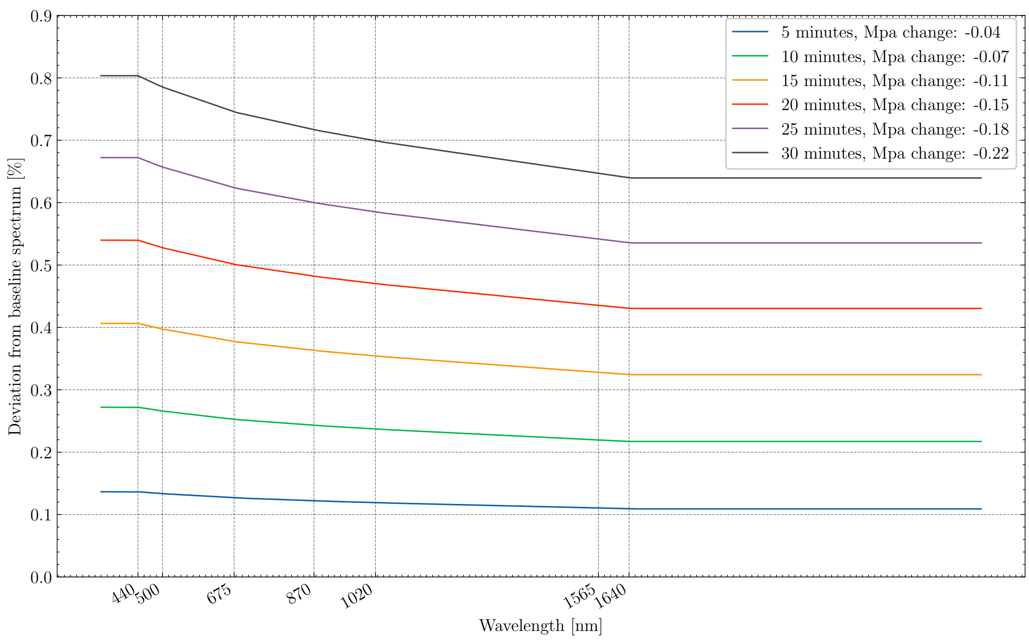

Figure 6.5: Deviations from a baseline lunar spectrum (calculated lunar spectrum at 22.12.2026 21:00) are depicted with increasing temporal separation/ increasing Moon phase angle change. The gridlines include the 6 CIMEL wavelengths 440 nm, 500 nm, 675 nm, 870 nm, 1020 nm and 1640 nm and the center wavelength of the BGL measurements 1565 nm. The inputs for LIME are the GEO coordinates of the OGSOP (altitude: 650 m, longitude: 11.277 98°E, latitude: 48.084 76°N) and the timestamps 22.12.2026 21:05,22.12.2026 21:10, . . . , 22.12.2026 21:30.

As with daytime measurements, the lunar position changes significantly during a measurement. The associated change in radiance between consecutive calculations with five minute separation for a winter and summer day and across different observation positions is illustrated in Figure 6.6 [5]. During moonrise and moonset the highest changes are observed. However, measurements were not conducted during these times, and consequently the impact can be neglected. Across the entire night, values up to approximately 5% are reached. Consistent with daytime simulations, reducing the time between two consecutive simulations increases the accuracy (see Figure 6.7).

The procedure for creating nighttime simulations for a BGL measurement is schematically illustrated in Figure 6.8 and is very similar to daytime simulations. A Moon spectrum can be provided to the simulation function or is calculated for the provided measurement file, with the middle timestamp being inferred from the data table. Otherwise, the inputs remain the same as for the daytime simulations ,and when visualized, error bars are utilized based on the same reasoning as in Section 6.2.

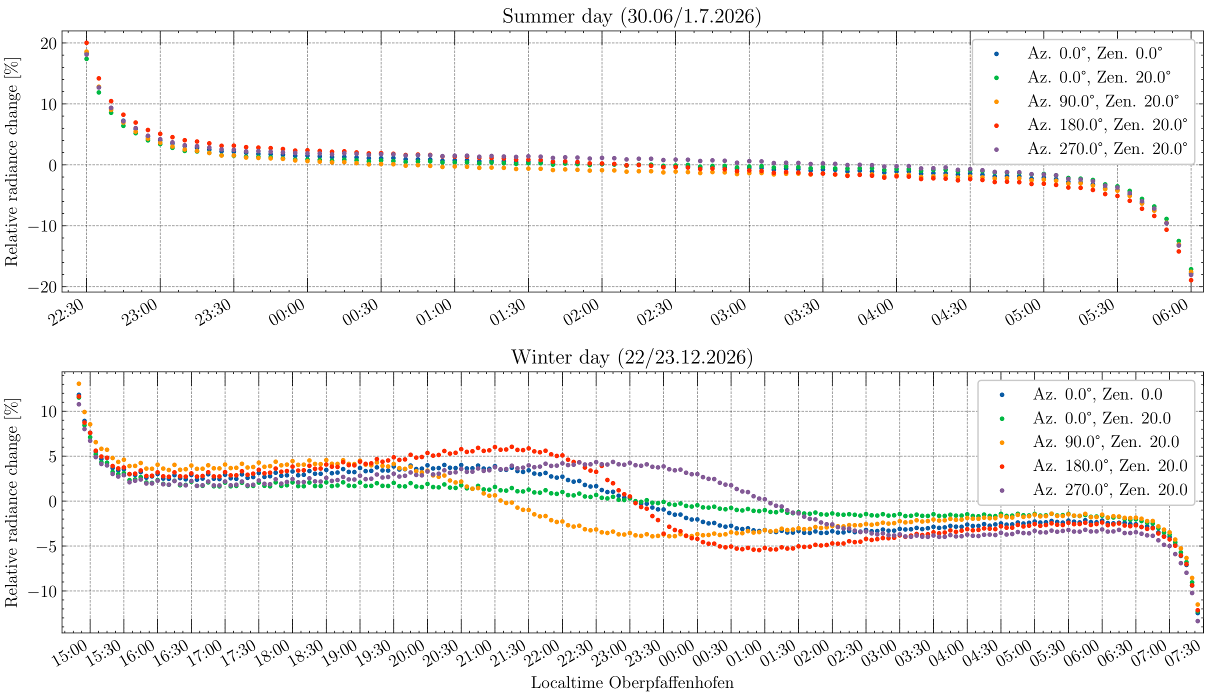

Figure 6.6: Relative changes between consecutive lunar radiance simulations during summer and winter with five minutes separation for different observer positions (Az. = azimuth angle, Zen. = zenith angle) are illustrated. The changes peak during moonrise and moonset and vary more in winter, when the Moon rises to higher elevations. For the simulations, settings and procedures for the lunar spectra are explained in Section C.5.

[5] The underlying spectra were calculated using LIME following the previously established rule: each ten minute segment has a lunar spectrum calculated at its middle timestamp.

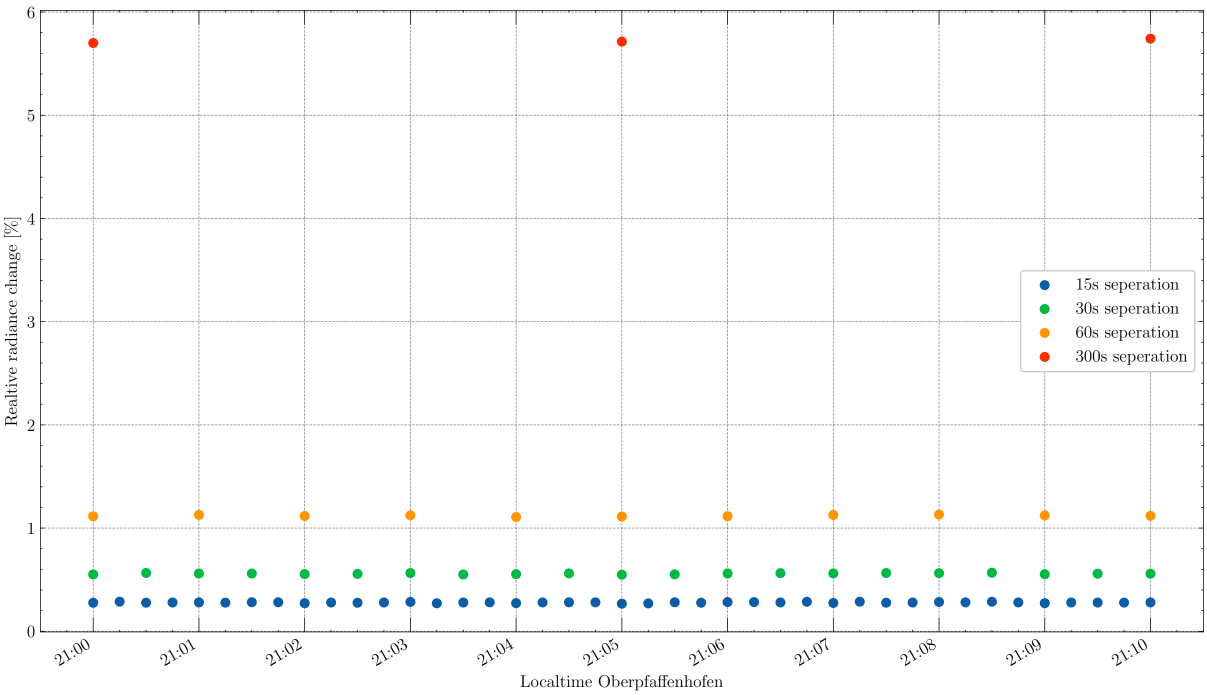

Figure 6.7: Depicted are the changes between consecutive lunar radiance simulations for the winter scenario in Figure 6.6 over a short time period with varying temporal separations. With decreasing temporal separation, the relative change decreases at the cost of increasing computational time due to more simulations being conducted. For the simulations, settings and procedures for the lunar spectra are explained in Section C.5.

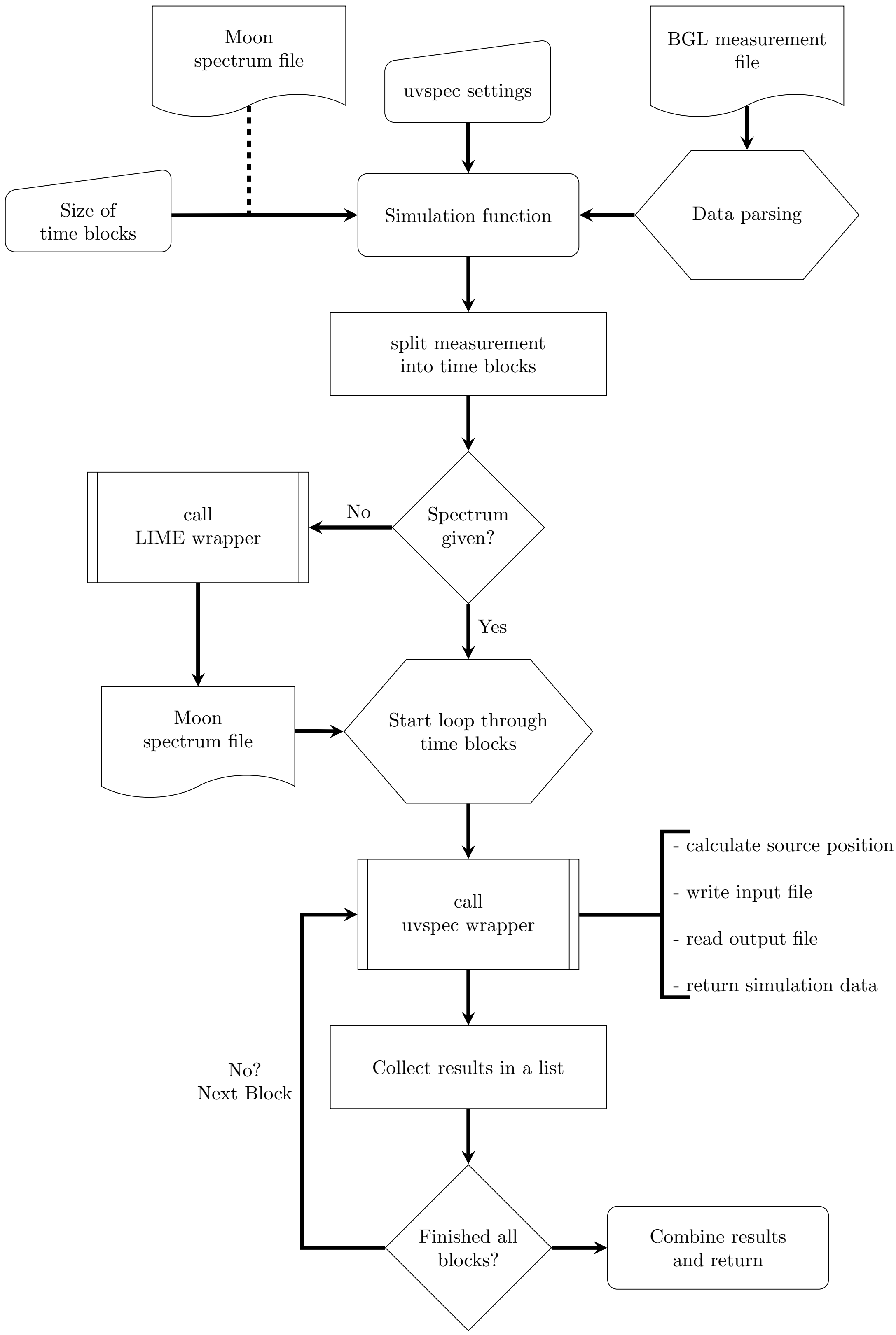

Figure 6.8: Schematic representation of the process of simulating BGL for a nighttime measurement. A precise breakdown of the functions inputs is given at the end of Section 6.3. For a full measurement series with multiple observation positions, this procedure is repeated for each observation position. The source position is calculated based on the middle timestamp of the current block.

Chapter 7

Measuring background light with the OGSOP

To measure BGL in the C-band, the pre-existing setup at the OGSOP (altitude: 650 m, longitude: 11.277 98°E, latitude: 48.084 76°N), is extended by a fiber based optical setup developed for BGL detection. This chapter first introduces the full optical setup and the procedures for the SMF coupling alignment and transmission loss measurements. Subsequently, the data acquisition and post-processing methodologies are outlined. Finally, the chapter concludes with an introduction of the measurement campaigns performed and analyzed in this work.

7.1 Optical setup

The full setup, involving the pre-existing optical setup, can be split into three primary segments: the telescope and Coudé train (connection of telescope with the Coudé laboratory), the free-space path on the optical bench (Coudé bench) and the fiber-guided path to the SNSPD.

Telescope and Coudé train

The telescope, a Ritchey-Chrétien type in Nasmyth configuration, is a three mirror system with main mirror diameter of 80 cm and a freely 360° rotatable tertiary mirror. Light can be directed to one of the four installed Nasmyth ports. Port two connects the telescope with the Coudé lab via the Coudé train. Inside the latter, the light is collimated, and a vacuum tube serves to isolate telescope and laboratory. A comprehensive overview of this subsystem can be found in [54].

Free-space path

Figure 7.1 illustrates the entire optical system. First a beamsplitter directs a part of the collimated beam towards a infrared camera, which can be used to monitor the image as seen by the telescope. Subsequently, the light passes through the first optical relay[1]and is redirected by a tip and tilt mirror. The second relay focuses pupil plane on a deformable mirror (DM), which together with the tip and tilt mirror, form a part of the AO, which aids the SMF coupling in a QKD downlink scenario. During the BGL measurement campaigns,the AO system is not utilized and the tip- and tilt mirror and deformable mirror replaced by flat mirrors. The light is then redirected by mirrors, and a third relay refocuses the beam onto a dichroic mirror. The dichroic mirror features a center wavelength of 1565 nm and an effective bandwidth $\Delta\lambda_{\text{eff}} = 34.9\,\text{nm}$. A final lens is installed to aid the SMF coupling. To permit manual adjustments of the coupling, the SMF is mounted on top of a movable platform,which can be moved in all three spatial directions (x,y,z). In addition, the mount allows angular tip and tilt adjustments. The complete optical system on the Coudé bench has an effective focus length of $f_{\text{OGS}} = 3865\,\text{mm}$.

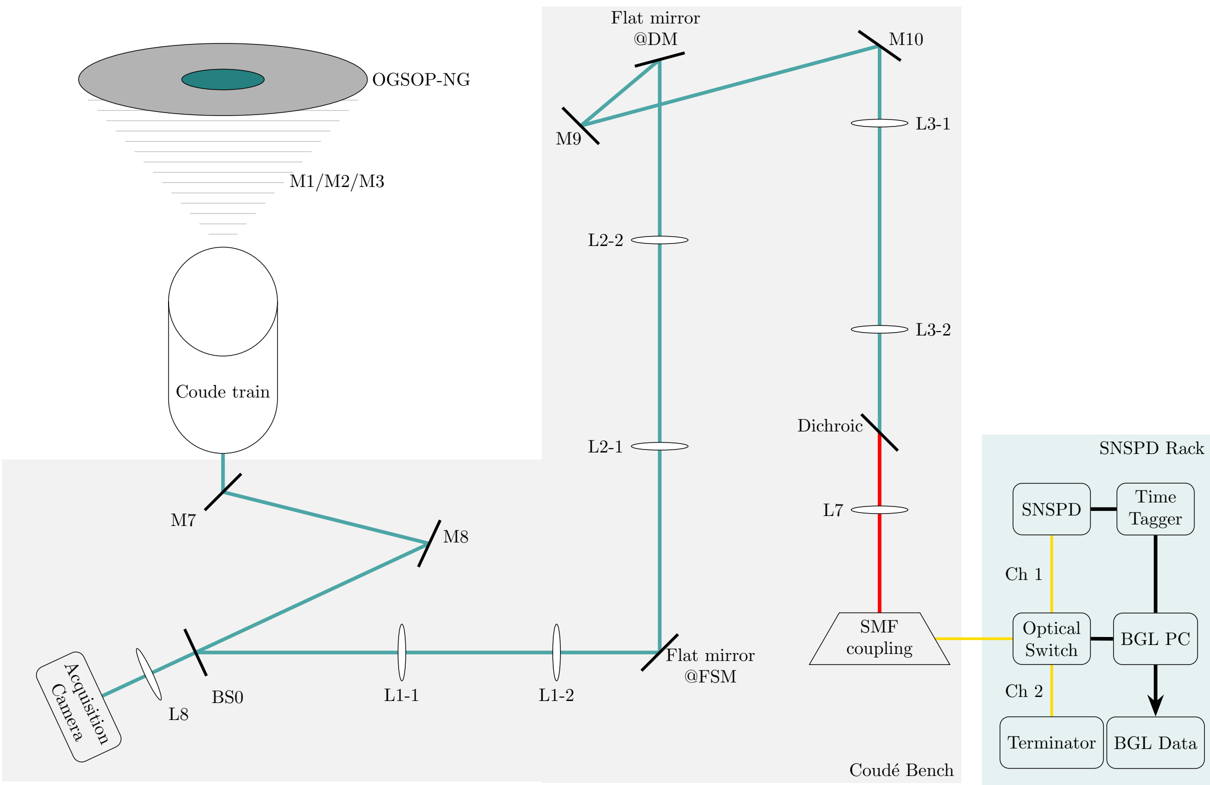

Figure 7.1: The optical setup for BGL measurements consists of the OGS connected to the lab via the Coudé train, the Coudé bench and the SNSPD rack. Light is guided via the Coudé train and a lens system until it is coupled into a SMF. Afterwards an optical switch either directs the light onto the SNSPD or terminates it. The voltage spikes of the SNSPD are registered with a time tagger.

[1]The optical relays in this setup refocus the pupil plane of the collimated beam.

Fiber guided path

After the light is coupled into the SMF, it is guided to the rack housing the SNSPD. a standard ID281 SNSPD System by ID Quantique. For the data acquisition, a Swabian Instruments Time Tagger Ultra is utilized[2].

Due to significant fluctuations and drifts observed in the DCR of the SNSPD, the optical switch, a FFSM-126C01332 optical switch module by Agiltron, was integrated into the setup. Figure 7.2 depicts the DCR measured over a long time period in a) and a short time period in b). For better visual clarity, a rolling average was applied to both measurements with a window of 60 s in a) and 30 s in b). In a) a distinct drift can be identified, particularly from the second hour until the end of the measurement. This drift, while small, is detrimental for nighttime measurements where low count rates are expected. These results demonstrate, that a single DCR measurement at the start of a multi hour campaign is insufficient.

Substantial fluctuations were also observed over shorter timescales as depicted in b). The standard deviation within the time window is 26.28 Hz, which rises concerns even if the DCR is measured prior to any BGL measurement.

Since the DCR cannot be monitored in parallel to the data collection, an alternative approach was implemented to estimate the current DCR. By integrating the optical switch as shown in Figure 7.1, it is possible to alternate between measuring the BGL and DCR (R_{sig}) or the DCR (R_{dcr}) depending on the active channel. The important specifications of each electrical and optical component can be found in Table A.1.

[2]The trigger level of the time tagger was adjusted to fit the output voltage spike of the SNSPD prior to this work.

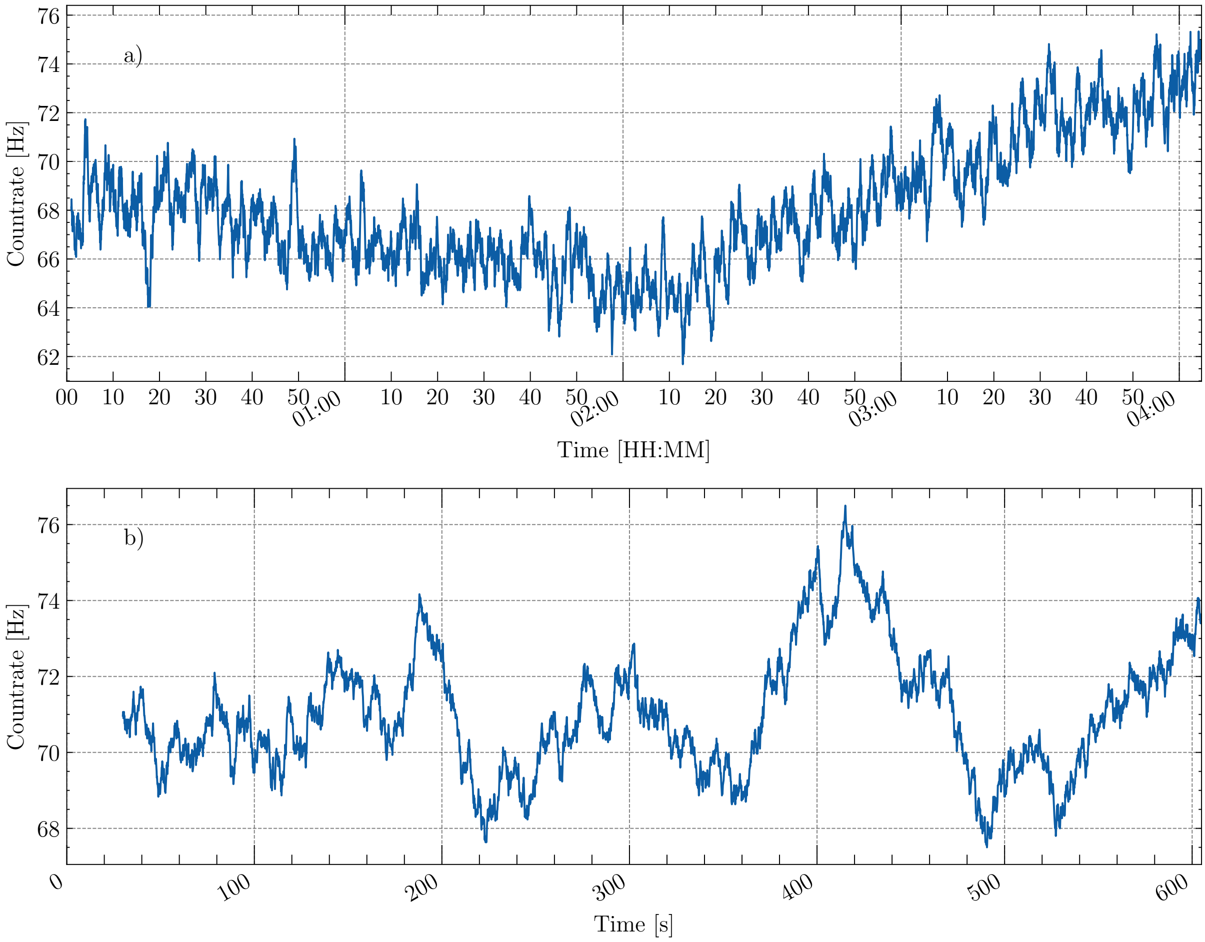

Figure 7.2: a) Rolling average of the DCR with a window of 60 s. b) Rolling average of the DCR with a window of 30 s. The data was acquired with the time tagger while all input ports of the SNSPD were covered.

7.2 Calibration of the transmission losses

Before each measurement campaign, the transmission loss of the OGSOP must be calibrated to calculate the system efficiency η_{sys}, which is used to convert the measured count rates to radiances according to Equation 5.9. Prior to determining the calibration loss, all fiber connectors are cleaned and the SMF coupling alignment is verified[3]. To perform the verification and any potential realignment, the setup shown in Figure 7.3 is utilized.

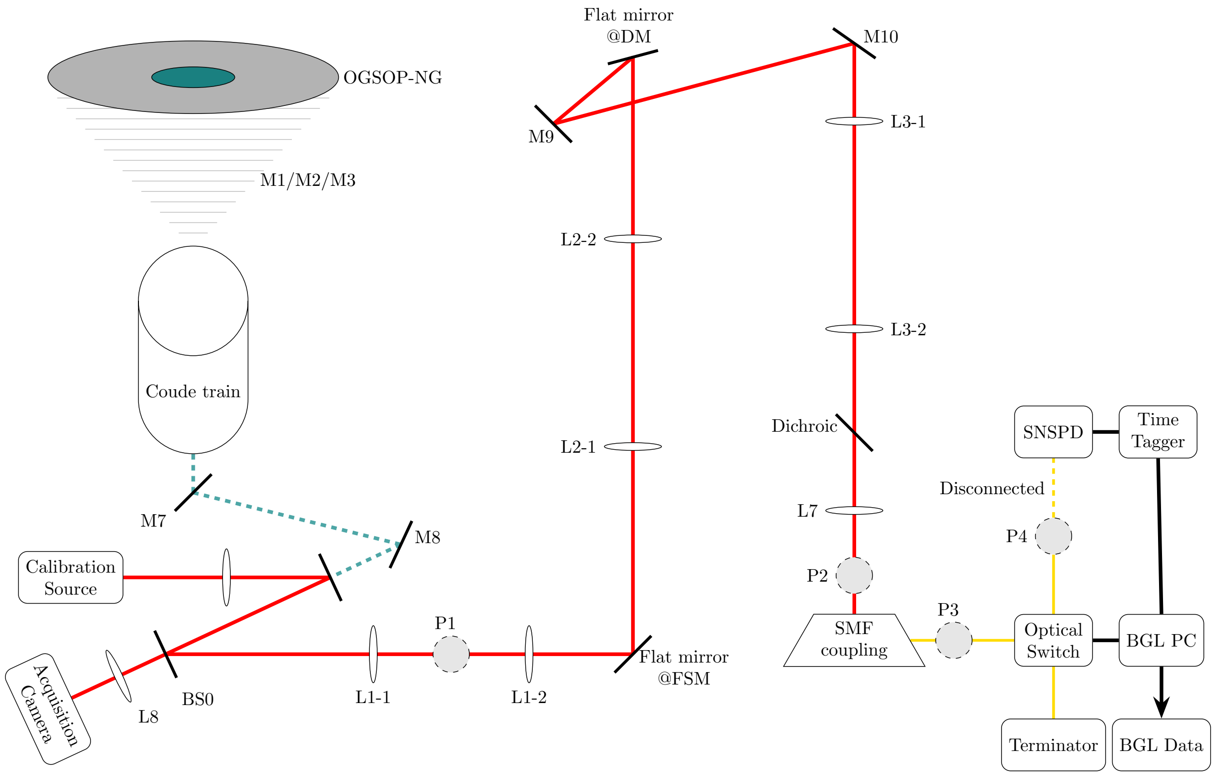

Figure 7.3: For the alignment of the setup, the light from the Coudé train is blocked and instead, the telescope simulator provides a collimated beam at 1565 nm. Power measurements are conducted at points P1-P4. Measuring the power between P2 and P3 aids the alignment of the fiber coupling, while measurements between P1 and P2 as well as between P3 and P4 are used to determine the losses in the setup. To prohibit the SNSPD from heating up, the fiber connection to the SNSPD is not established and the light is terminated.

An auxiliary mirror is inserted into the Coudé bench setup to block the light from the telescope, while simultaneously connecting the telescope simulator, comprising of a tunable C-band laser and a lens system, to the optical path of the Coudé bench. This laser provides a collimated beam at 1565 nm, the center wavelength of the dichroic, and is used for the fiber alignment and the transmission loss measurement.

[3]The alignment of the Coudé bench is verified in advance by colleagues.

The target for the fiber alignment is a coupling loss of less than −3.0 dB, marking the expected median SMF coupling loss in experiments [55]. The loss of the fiber coupling is determined by measuring the power with a Thorlabs S122C sensor at points P2 and P3 in Figure 7.3. To adjust the alignment, the screws on the fiber mount platform are utilized (see Section 7.1).
Subsequently, the powers at the highlighted measurement points P1-P4 in Figure 7.3 are measured to determine the transmission losses. Throughout the whole process, it is mandatory to attenuate or terminate the light before it reaches the SNSPD to prevent it from heating up, as the maximum power rating at 1565 nm of 3.8 pWwould otherwise be exceeded[4].
The system efficiency (η_{sys}) is derived from the losses determined by the prior measurement with

- $\text{Loss}_{\text{Coudé}}$: The loss accumulated before measurement points P1 including the telescope and Coudé train. This loss was characterized in previous works and is fixed at −3.8 dB [2].
- $\text{Loss}_{\text{free-space}}$: The loss accumulated between measurement points P1 and P2, which includes all optical components up until the SMF coupling.
- $\text{Loss}_{\text{fiber-segment}}$: The loss accumulated between measurement point P3 and P4 including the losses inside the SMF and the optical switch.

These values are substituted into Equation 7.1. Equation 7.1 does not explicitly include the measured coupling losses of the SMF coupling, as this effect is treated indirectly by including the MFD of the SMF (see Section 5.2).

$$\begin{aligned} \eta_{sys} &= \eta_{\text{Coudé}} \cdot \eta_{\text{free-space}} \cdot \eta_{\text{fiber-segment}} \\ \eta_i &= 10^{-\text{loss(dB)}_i/10} \end{aligned} \tag{7.1}$$

[4]The power limit is derived from the maximum detection rate (see Table A.1)

7.3 Data acquisition and post-processing

7.3.1 General data acquisition

For the acquisition of data and the control of the optical switch, a web interface was developed (see Figure D.1). A measurement for a specific telescope position can be conducted fully automated with the software when the telescope has been moved to the desired position. Once the measurement is started with a provided measurement duration, a periodic callback is initiated. Every second the integrated count rates are queried from the time tagger and an index counting the amount of count rates queried is incremented by the queried amount. This index is compared with the threshold that is set for the optical switch activation. If the threshold is reached, the counter is reset and the active channel toggled. As soon as the measurement duration is reached, the measurement is terminated and the data is saved. To be able to distinguish DCR and signal count rates, the optical channel is tracked within the saved data and is utilized in the post-processing to calculate photon rates and radiances. A more detailed description of the capabilities of the interface and all possible inputs is given in the Appendix in Section D.1.

7.3.2 General data post-processing

In post-processing the measured count rates are converted to measured radiances using Equation 5.9[5]. Therefore, the data is sliced into consecutive pairs of R_{sig} and R_{dcr} blocks using the tracked active switch channel. For each consecutive pair of R_{sig} and R_{dcr} blocks, a measured radiance is calculated by taking the mean of the measured R_{sig} and R_{dcr}.
However, before the mean is taken, the data is masked by discarding the measured count rates in direct vicinity of the change of the active switch channel. This step is necessary, because the detection system electronics and the optical switch control are not synchronized. The SNSPD continuously detects photon counts, which are integrated by the time tagger and returned upon request. If the channel is switched while data is being accumulated for a specific bin, the bin can not be attributed to either R_{sig} or R_{dcr}, but rather is a superposition of both.
Figure 7.4 provides a schematic representation of the effect for two signals: a 1 Hz signal at channel one and a 5 Hz signal at channel two. In an ideal scenario, the optical switch would trigger instantaneously, once the specified amount of count rates was queried, but in real measurements delays in code occur and hardware does not react instantaneously.

[5] A comprehensive list of parameters and their origins can be found in the Appendix in Table B.1.

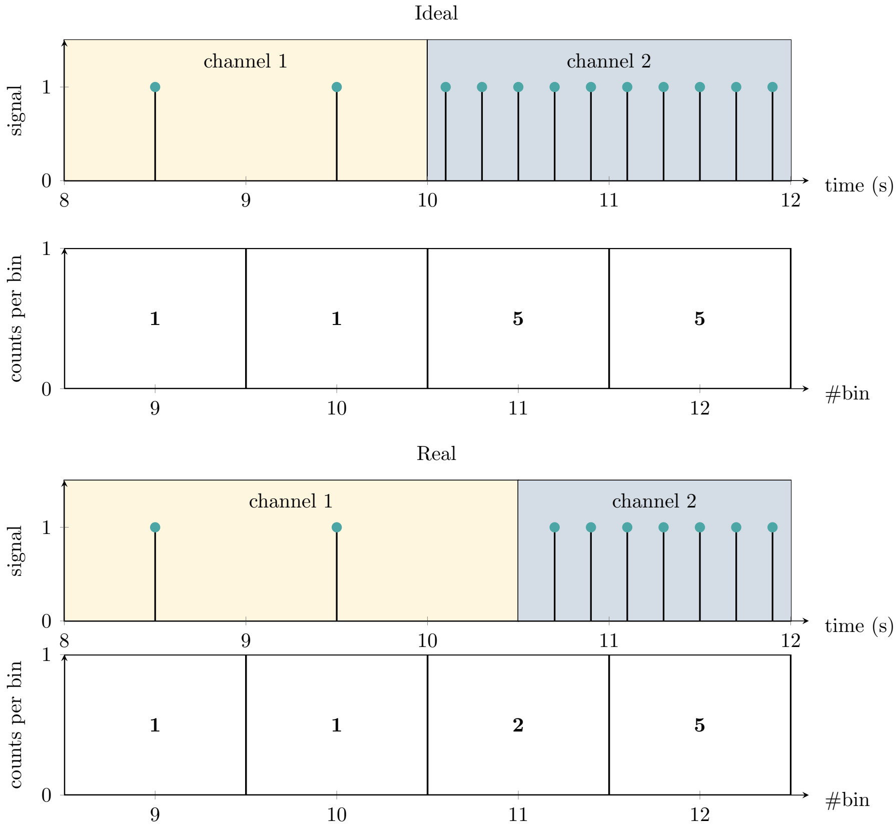

Figure 7.4: The impact of the missing synchronization between the optical switch and the time tagger is illustrated for two signals: 1 Hz at channel 1 and 5 Hz at channel 2. In the ideal case, the optical switch activates once a bin of the time tagger is fully integrated such that all bins perfectly resemble the frequency of the expected signals. In the experiment, the optical switch and time tagger are not synchronized leading to switches occurring while data is accumulated in one bin. These bins contain information of the DCR and the signal and cannot be used in post-processing.

The effect is illustrated in Figure 7.5 for a measurement conducted with a laser, the optical switch and the SNSPD. The active channel was changed after ten count rates were received, while count rates are queried every second from the time tagger. The data points between both, the R_{sig} and R_{dcr} level are clearly visible at these high powers.
An example of the most important steps of the conversion is given in Table 7.1 for real BGL data taken from a daytime measurement.

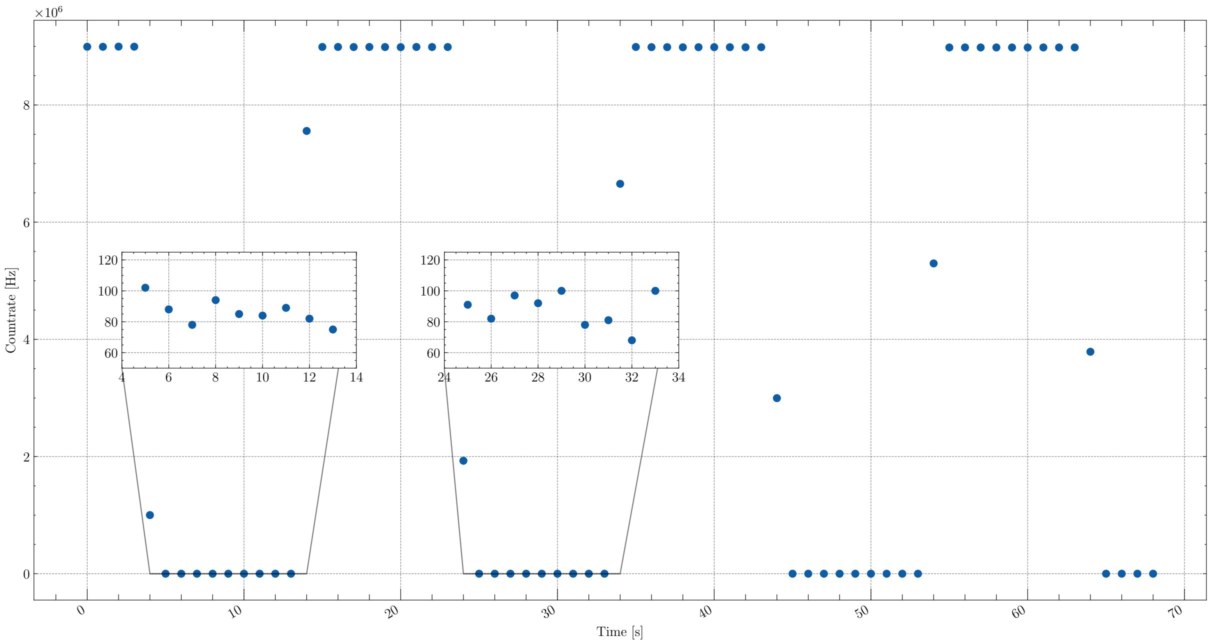

Figure 7.5: To simulate a BGL measurement, an attenuated laser source was connected to the optical switch and the channels were connected identical to the setup described in Figure 7.1. The effect of the missing synchronization is clearly visible, as data points between the signal and DCR level occur, which have to be treated in post-processing.

Count rate [Hz]	Switch tag	Masked count rate [Hz]
362484.0	1.0	NaN
360720.0	1.0	360720.0
361564.0	1.0	361564.0
362637.0	1.0	362637.0
361243.0	1.0	361243.0
360182.0	1.0	NaN
239859.0	2.0	NaN
76.0	2.0	76.0
90.0	2.0	90.0
87.0	2.0	87.0
76.0	2.0	76.0
92.0	2.0	NaN
Mean R_{sig}	Mean R_{dcr}	Calculated radiance
361 541 Hz	82.25 Hz	$1.88\,\text{mW}\,\text{nm}^{-1}\,\text{m}^{-2}\,\text{sr}^{-1}$

Table 7.1: The data was taken from a BGL measurement during daytime resembling one block of signal count rate (R_{sig}) and dark count rate (R_{dcr}). Equation 5.9 is applied to the mean values of the masked data. A mask is applied, to remove erroneous values in the vicinity of the active channel change of the optical switch. The parameters for the equation are taken from Table B.1 with η_{sys}=0.251. A tag 1.0 is equivalent to measured R_{sig} and a tag 2.0 is equal to measured R_{dcr}.

7.3.3 Conducted measurement campaigns

Several BGL measurement campaigns were conducted throughout the time of this thesis. Each campaign was planned and executed under clear sky conditions, as these represent the most common conditions for satellite QKD and allow the measured radiance to be compared with simulation results (see Section 6.1). Each campaign consisted of multiple measurement series, with each series corresponding to measurements conducted for a fixed azimuth angle with varying zenith angles. Prior to each campaign, the transmission loss was determined and the SMF aligned according to the procedure outlined in 7.2. In addition, during night measurements a bright star was tracked prior to performing BGL measurement to verify the functionality of the setup. Furthermore, during each measurement, all ambient sources of light in the laboratory were turned off or blocked.

Measurement day: 08.08.2025 Four measurement series from this campaign are included in this thesis. The first two are daytime measurement conducted at fixed azimuth

angles of 45° and 135°. The measurement directions were chosen such that the telescope did not point towards the Sun, which is common for optical communication. The zenith angle of the telescope was varied between 0° and 70° in 10° degree steps for both measurement series and for each position approximately 10 minutes of data was acquired [6].
In addition, a sunset measurement was performed from 17:00 to 22:20 local time. During this measurement, the telescope was pointed at the zenith and data was accumulated for the full duration of the measurement.
Afterwards, the light pollution of Munich during the night with a full Moon was observed, by pointing the telescope toward an azimuth direction of 75°. The zenith angles were varied from 80° to 0° in 10° steps to better capture the anthropogenic light close to the surface at high zenith angles closer. Each position was monitored for approximately 10 minutes.
Measurement day: 04.11.2025 Two measurement series during full Moon conditions from a measurement campaign conducted with a partner are included in this thesis. The first series, at an azimuth angle of 0°, captures a region of very low light pollution with only a few distinct sources of anthropogenic light close to the surface. The second direction, at an azimuth angle of 150°, features measurements in relative proximity to the Moon, a major source of BGL. Instead of scanning the zenith angles with a fixed step width, four/ or five distinct zenith position were chosen during this campaign. These include the zenith angles of 12°, 24°, 36°, 60° and the zenith position of 0°, which is incorporated into the measurement series for the azimuth angle of 0°.
A short summary of each measurement is provided in Table 7.2, including further information regarding the measurement times and environmental conditions in the respective viewing directions. For the measurement series featuring multiple timestamps, the timestamps correspond to the measured zenith angles in descending order, starting with a zenith angle of 0° for the azimuth angle of 0° and 12° for the azimuth angle of 150°.

Table 7.2: Environmental conditions of the BGL measurement series.

Azimuth	**Time window (local time)**	**Environment description**
	08.08.2025	
45°	14:27 - 15:36	Construction site with cranes and campus buildings, then air field and agricultural fields

[6] At the time of this campaign, the automatic measurement feature ensuring a distinct measurement time was not implemented yet such that the real measurement time varies slightly.

Table 7.2: Environmental conditions of the BGL measurement series.

Azimuth	**Time window (local time)**	**Environment description**
135°	17:43 - 19:01	Neighbouring campus building at slightly lower height as the OGSOP, then air field and agricultural fields
75°	22:26 - 00:11	Construction site with cranes and campus buildings, then air field, and Munich in the distance
Sunset at zenith	17:00 to 22:20	Clear view of the sky.
	04.11.2025	
0°	19:41 - 19:51 20:48 - 20:58 21:39 - 21:49 22:29 - 22:39 23:06 - 23:16	Construction site with cranes and campus buildings,then fields close to the small city of Neugilching
150°	20:08 - 20:18 21:01 - 21:11 21:52 - 22:02 22:41 - 22:51	Similar to 135°

Chapter 8

SNSPD calibration

At the core of the optical setup for BGL measurements described in Section 7 is the ID281 SNSPD system by ID Quantique. To achieve a higher accuracy, a calibration setup was built to determine the fully recovered SDE. This chapter presents the calibration measurement setup and its development . Furthermore, a formula is derived and necessary intermediate steps are described. Subsequently, the data acquisition and post-processing procedures are detailed, before finishing with a short description of the conducted calibration measurement.

8.1 Calibration setup

To determine the fully recovered SDE, a relative measurement approach was implemented. In this configuration, the power of a laser beam is measured in parallel using the SNSPD and a second calibrated reference sensor (see Figure 8.1). For the latter, a Thorlabs S154C sensor is employed due it performance and ease of implementation. The S154C is compatible with the Thorlabs PM100D power meter console, which can be controlled via Standard Commands for Programmable Instruments (SCPI). Consequently, a *Python* backed was developed utilizing SCPI and the *PyVISA* package. In addition, the S154C features one of the lowest detection ranges for a non single photon detector, with a sensitivity as low as 100 pW.
In addition to the reference sensor and SNSPD the setup (see Figure 8.1) consists of a beamsplitter to split the light for the parallel measurement, fixed attenuators, an optical switch to enable consecutive measurements of the signal and dark count rates of the SNSPD in a consecutive (refer to Section 7.1 for further details), and a laser. The laser, a ID Photonics CoBrite tunable laser (SC type), provides laser light at 1565 nm with a minimum power of 7.6 mW. To keep the optical paths to the SNSPD and reference sensor nearly identical, a Thorlabs 99.9:0.1 (1×2) single-mode beamsplitter was selected.

With this beamsplitter and sufficient attenuation in front of it, the power at the tap and signal ports of the beamsplitter can be matched to fit the detection ranges of both detectors[1]

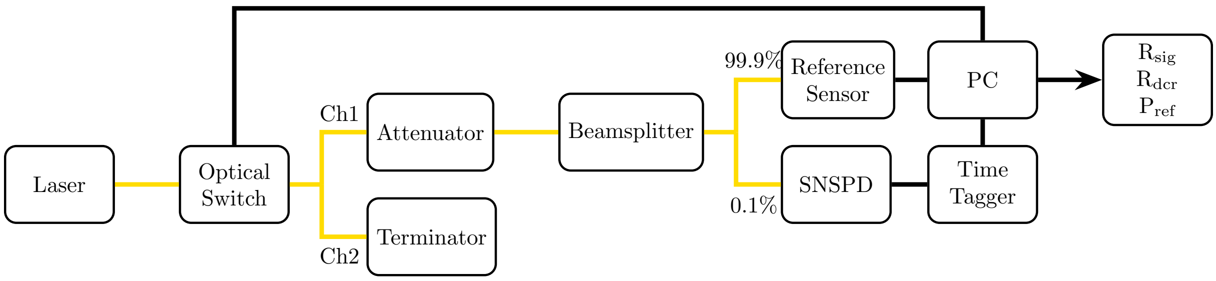

Figure 8.1: The first iteration of the optical setup used for calibration is fully fiber based and features an optical switch for the consecutive observation of DCR and signal count rate. Light is split with a beamsplitter and a reference sensor is used to monitor the power in parallel. Details on the components can be found in Table A.1.

Multiple test measurements were conducted with this setup, with two results depicted in Figure 8.2. The data depicted in c) and d) was taken directly after the laser emission was activated. A clear decrease in power over time is visible, which is caused by the laser stabilizing its power output. To ensure this effect does not influence the calibration negatively, calibration measurements were not performed until the laser had a least one hour to stabilize its power output.
The measurement shown in a) and b) exhibits fluctuations in the count rate of the SNSPD. These fluctuations are not present in the power readings of the reference sensor and can be attributed to the polarization sensitivity of the SNSPD (see Section 3.2.1). Although the CoBrite laser features a polarization maintaining output, the polarization state does not remain constant over time. This assumption was verified by connecting the laser to a polarization controller (PSY-201 by Luna Innovations[2]) (see Table A.1) and monitoring the change of the Stokes parameters over a two hour time period (see Figure 8.3).

[1]The S154C sensor has a minimum detection power of 100 pW, while the SNSPD at 1565 nm possesses and approximate upper power limit of 3.8 pW which is calculated based on the maximum detection rate of 30 Mcps (see Table A.1).

[2]Previously known as General Photonics.

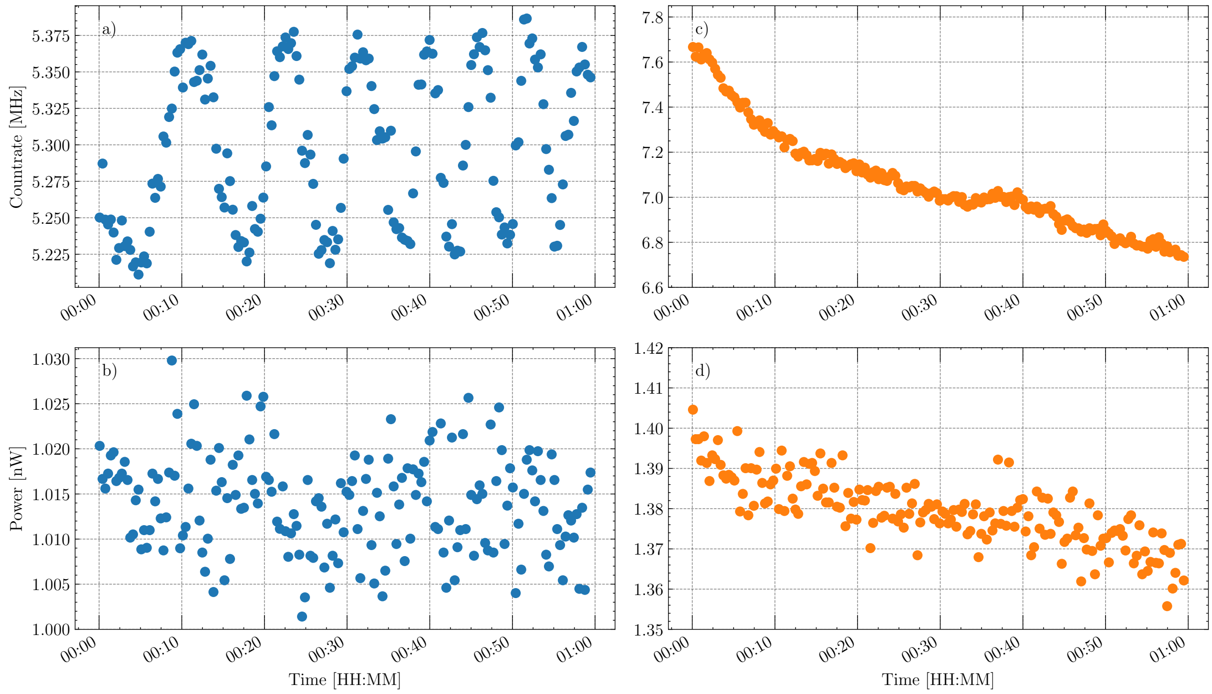

Figure 8.2: Two results of power and count rate measurements conducted with the setup illustrated in Figure 8.1 are shown. a) and b) feature periodic fluctuations in the SNSPD signal, not visible at the Thorlabs S154C sensor. In c) and d) a decline in both detected count rate and power over time is visible. The data for c)/d) was taken shortly after the laser emission was enabled, while a)/b) was observed after the emission was enabled for a few hours.

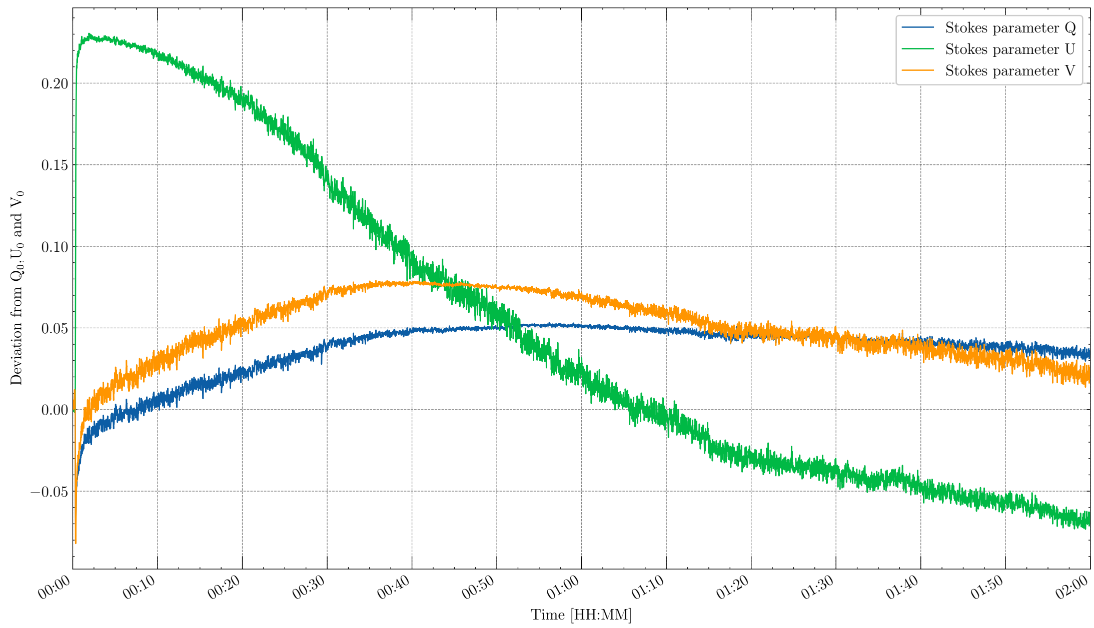

Figure 8.3: Deviations of the polarization state parameterized by the Stokes parameters Q, U and V, measured with the PSY201 polarization controller by Luna Innovations. The deviations are calculated with respect to the first measured values of Q,U and V.

Due to the drifting polarization state of the laser and the polarization sensitivity of the SNSPD, a polarization controller (PSY-201 by Luna Innovations) was incorporated into the final setup (see Figure 8.4). The PSY-201, similar to the PM100D power meter console, can be controlled via SCPI. Consequently, a *Python* backend was developed to regulate the polarization state of the light. Because the minimum input power of the polarization controller is approximately 316 nW, attenuation is performed in front and after the controller to ensure minimal disturbance of the tracked polarization state.
To evaluate the performance of the SNSPD in a typical BGL measurement scenario, the incident light should ideally be unpolarized. This can be achieved by utilizing the discrete polarization scramble option of the PSY-201 by applying a high scramble frequency. Additionally, the polarization controller is used to identify the maximum and minimum fully recovered SDE. Therefore, a grid of polarization states on the Poincaré sphere is generated (see Figure 8.8) and a calibration measurement is conducted for each polarization state.

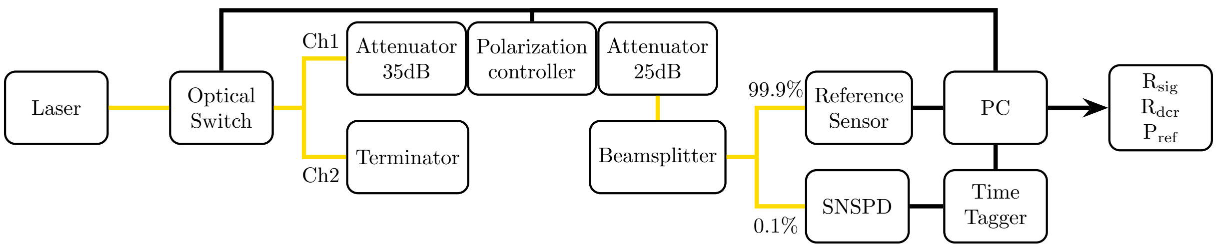

Figure 8.4: Final setup used for the calibration of the SNSPD. In comparison to the first iteration (see Figure 8.1), a polarization controller was added to test the polarization sensitivity of the SNSPD. Attenuators were placed in front and after the polarization controller to ensure the tracked polarization states are disturbed as little as possible. Components can be found in Table A.1.

8.2 SNSPD efficiency calculation

The formula used to determine the fully recovered SDE ($\eta_{\text{sde},0}$) is derived from the relationship between count rates and photon rates (see Equation 5.1). By substituting this equation into Equation 5.5 the power incident on the SNSPD can be expressed in terms of the SDE (η_{sde}):

$$P_{\text{SNSPD}}(\eta_{\text{sde}}(R_{\text{sig}})) = \frac{h \cdot c}{\lambda \cdot \eta_{\text{sde}}(R_{\text{sig}})} \cdot (R_{\text{sig}} - R_{\text{dcr}}) \tag{8.1}$$

The R_{sig} dependency of η_{sde} can be neglected if $\tau_{\text{ph-ph}} = \frac{1}{R_{\text{sig}}} >> \tau_{\text{rec}}$. If this condition is satisfied, η_{sde} is equal to $\eta_{\text{sde},0}$. Because the SNSPD calibration was conducted at higher count rates, this condition is not satisfied and the count rate dependency has to be taken into account (see Equation 5.3). Since the power is measured in parallel, the power at the SNSPD can be expressed in terms of the power measured at the reference sensor via

$$P_{\text{ref}} = \gamma \cdot P_{\text{SNSPD}} \iff \gamma = \frac{P_{\text{ref}}}{P_{\text{SNSPD}}} \equiv \frac{P_{\text{signal port}}}{P_{\text{tap port}}} \tag{8.2}$$

where γ quantifies the conversion ratio between the signal and tap ports of the implemented beamsplitter. Combining Equation 8.2 and Equation 8.1 yields

$$\eta_{sde,0} = \frac{h \cdot c \cdot (R_{\text{sig}} - R_{\text{dcr}}) \cdot \gamma}{\lambda \cdot P_{\text{ref}} \cdot \left(\frac{\alpha\pi}{\sin(\alpha\pi)} \cdot \exp(-\alpha\Gamma) - \frac{\alpha}{1-\alpha} \cdot \exp(-\Gamma)\right)} \tag{8.3}$$

with $\alpha(R_{\text{sig}}) = R_{\text{sig}}\tau_*$ and $\Gamma = \frac{\tau_{\text{rec},50}}{\tau_*}$. To apply Equation 8.3, the γ-factor must be determined according to the procedure outlined in Section 8.2.2.

8.2.1 Determining the SNSPD recovery time

To calculate the fully recovered SDE described by Equation 8.3, $\tau_{\text{rec},50}$, the recovery time at 50% of the fully recovered SDE, and τ_* must be determined. Therefore, the data from a recovery time characterization is fitted with the exponential sigmoid function in 8.4. This data was kindly provided for our detection system by ID Quantique, an IonQ company.

$$\text{NormCounts(t)} = \frac{1}{1 + \exp\left(-\frac{t-\tau_{\text{rec},50}}{\tau_*}\right)} \tag{8.4}$$

Figure 8.5 a) displays the raw unfitted data, while b) illustrates the sigmoid fit. To generate the fitted dataset in b) from the original data the following steps were conducted:

1. Identify the end time of the laser pulse.
2. Extract the part of the data accumulated subsequent to the saturation pulse.
3. Shift the timescale such that zero is equal to the end time of the pulse.
4. Normalize the counts to the fully recovered steady-state level following the saturation.
5. Apply the exponential sigmoid function in Equation 8.4 to fit the data and extract $\tau_{\text{rec},50}$ and τ_*.

The extracted values for the first channel of the SNSPD system, which was utilized during the BGL measurements and calibration measurement, are $\tau_{\text{rec},50} = 73.132\,\text{ns}$ and $\tau_* = 12.767\,\text{ns}$.

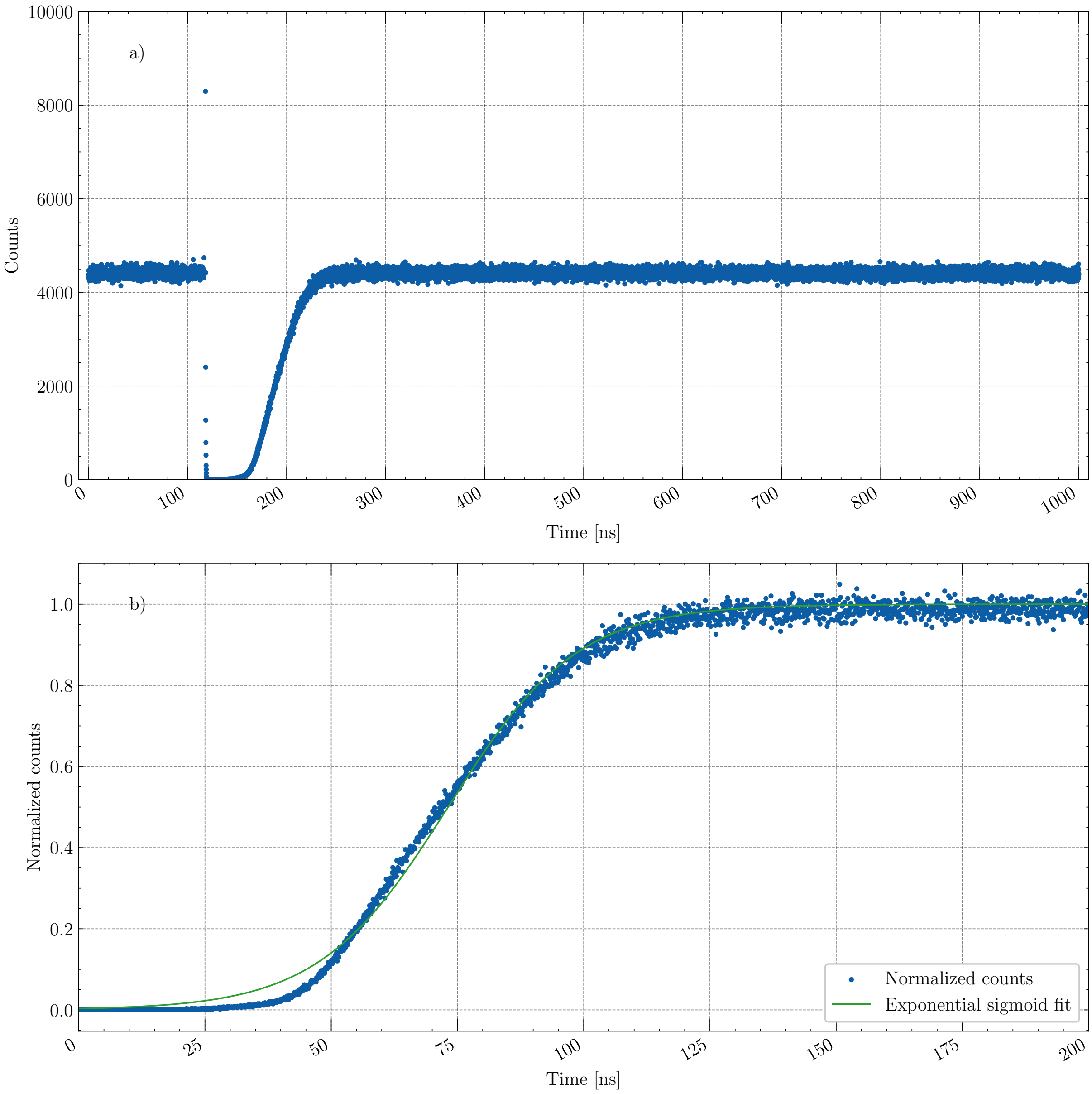

Figure 8.5: Illustration of recovery time measurements. Data courtesy of ID Quantique, an IonQ company. a) Raw data as received by ID Quantique. b) Exponential sigmoid fit of recovery time after saturation.

8.2.2 Measuring the conversion ratio between beamsplitter ports

The γ factor, which describes the conversion ratio between the beamsplitter ports, must first be determined in a separate characterization measurement. Figure 8.6 shows the setup which merely consists of the same laser source sourced used in the calibration setup (set to 1565 nm), and two sensors connected to the tap and signal ports of the beamsplitter. Specifically, a Thorlabs S122C sensor is connected to the signal port, while a Thorlabs S154C sensor monitors the power at the tap port.

A *Python* based web interface, depicted in Figure D.3, was developed to automate the data acquisition[3]. For the characterization, power values are queried from both sensors over a one hour time period utilizing the identical backend developed for the power meter control in the SNSPD calibration setup (see Section 8.1).

According to Equation 8.2, γ is defined as the ratio of the power measured at the signal port to the power measured at the tap port. Consequently, if γ is calculated the tap-to-signal-port ratio, the γ term in Equation 8.3 must be placed into the denominator.

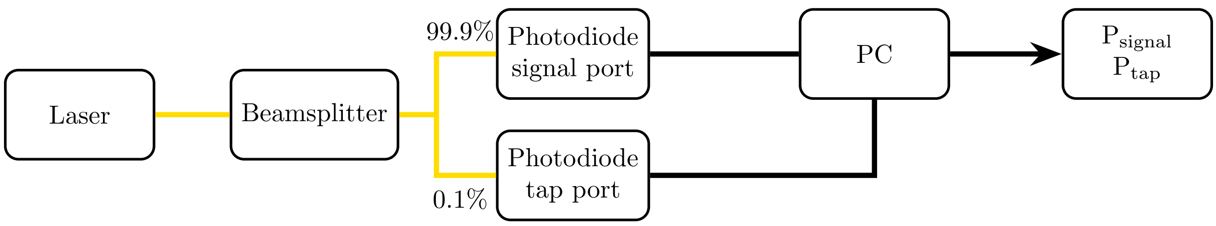

Figure 8.6: The setup to determine the γ-factor, describing the conversion ratio between the tap and signal port of the beamsplitter, consists of two photodiodes monitoring the power output in parallel at 1565 nm. Components can be found in Table A.1.

8.3 Data acquisition and post-processing

Similar to the BGL measurements, a *Python* based web interface was developed to manage the hardware components and the data acquisition (see Figure D.2). The components comprise the optical switch, the power meter console connected to the reference sensor, the polarization controller, and the time tagger.

As described in Section 8.1, the polarization controller is used to either scramble the polarization generating unpolarized light or to track a specific state on the Poincaré sphere. The software is capable of automatically executing a scan for a given grid, wherein an individual measurement is conducted for each polarization contained in the grid. After the polarization state for an individual calibration measurement is set, a periodic callback is initiated. With every execution, the power and count rate are queried from the time tagger

[3]For a more detailed breakdown of the capabilities of the software refer to Section D.3.

and power meter console. Once enough data has been collected to calculate a specified amount of $\eta_{\mathrm{sde},0}$ values , the calibration measurement is terminated and the data is saved. This process repeats for every polarization state included in the grid. The capabilities and input parameters of the interface are described in greater detail in Section D.2.
The saved data files occasionally do not contain data for every elapsed second of the calibration measurement. This discrepancy arises due to a lack of synchronization between the time tagger and the periodic query requests. Because of delays in code and hardware execution, a query request might return either no count rates or multiple count rates.

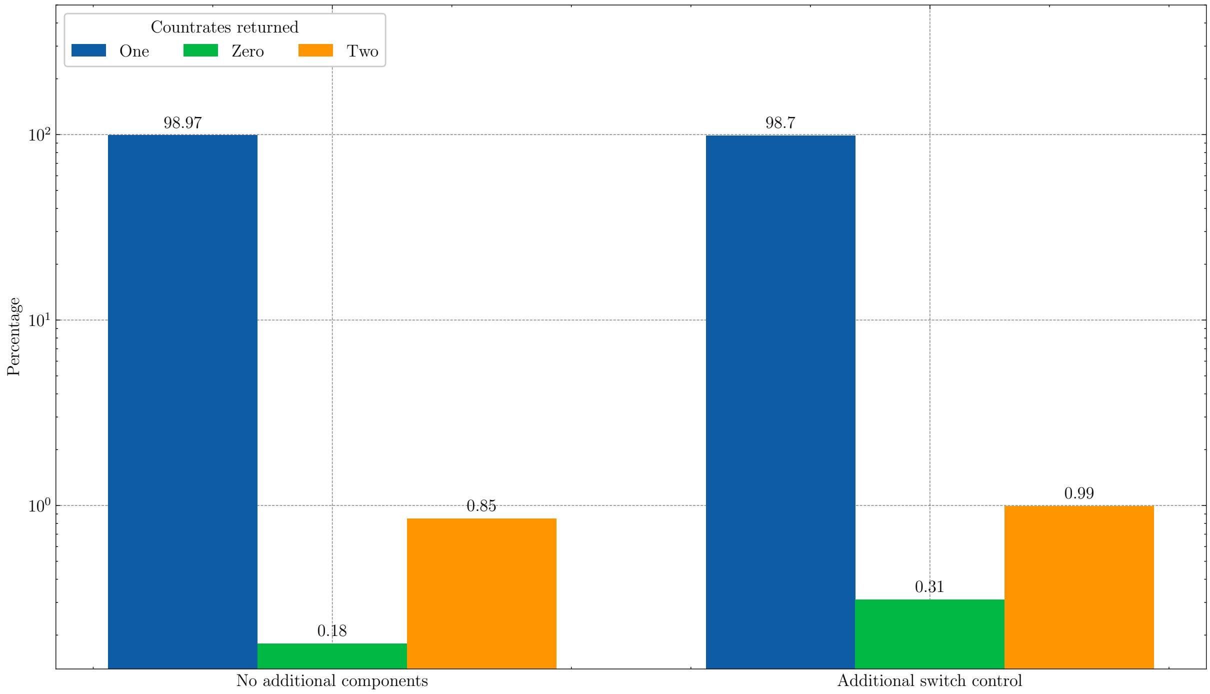

Figure 8.7: The amount of returned count rates by the time tagger in one single query request depends on the complexity of the executed code, as small delays in code and hardware execution disrupt the not actively enforced synchronization between the time tagger (continuous monitoring) and the measurement loop. On the left, the effect is shown for a simple DCR measurement with no additional components. One the right, a setup including the optical switch was used.

Although the probability of either occurring is low, as demonstrated in Figure 8.7, it disrupts the measurement flow if not addressed. If multiple count rates are returned, a corresponding power value cannot be mapped to each count rate, because the power is queried after the count rates are received. Consequently, the earlier received count rates are discarded and only the most recent value is kept. Conversely, if no count rate is returned, the measured power value is discarded. Based on test measurements illustrated in Figure 8.7, this procedure results in a data loss of less than 1%. In return, this procedure increases the accuracy of the calibration measurement due to the improved temporal correlation between queried count rate and power. If multiple count rates are returned and the current power were be used as a reference for both, inaccuracies due to variations in laser power during that time might not be adequately reflected. The saved data files contain the power of the reference sensor, as well as R_{sig} and R_{dcr}, which can be identified by the tracked active channel of the optical switch. Similarly to the post-processing of BGL measurements, the data for the calibration measurement is masked by discarding the measured count rates and powers in direct vicinity of the active switch channel transitions (for the explanation refer to Section 7.3.2). Consequently, the data is split into consecutive pairs of R_{sig} and R_{dcr} blocks. For each pair of blocks, Equation 8.3 is applied to the mean values of R_{sig}, R_{dcr} and P_{ref}. The latter calculation uses the data acquired during illumination (R_{sig} block) and does not consider the data from the R_{dcr} blocks, as the dark count rate is already subtracted by the power meter console. An example of the calculation is shown in Table 8.1.

Raw data			Masked data	
Count rate [Hz]	P_{ref} [W]	Switch tag	Count rate [Hz]	P_{ref} [W]
8164998.0	2.62480304e-09	1.0	NaN	NaN
8163975.0	2.65909095e-09	1.0	8163975.0	2.65909095e-09
8164115.0	2.64253841e-09	1.0	8164115.0	2.64253841e-09
8163641.0	2.64608557e-09	1.0	8163641.0	2.64608557e-09
8165903.0	2.64490252e-09	1.0	8165903.0	2.64490252e-09
8163269.0	2.62834998e-09	1.0	NaN	NaN
852094.0	-1.77876967e-11	2.0	NaN	NaN
125.0	-3.59929968e-12	2.0	125.0	-3.59929968e-12
138.0	-2.0151868e-11	2.0	138.0	-2.0151868e-11
145.0	-2.96110809e-11	2.0	145.0	-2.96110809e-11
146.0	-7.14639892e-12	2.0	146.0	-7.14639892e-12
150.0	-3.31581811e-11	2.0	NaN	NaN
Mean R_{sig}	Mean R_{dcr}	Mean P_{ref}	$\eta_{\text{sde},0}$	
8164408.5	138.5	2.6481543625e-09	0.4055	

Table 8.1: The data was taken from a calibration measurement series, resembling one shortened block of signal count rate (R_{sig}) and dark count rate (R_{dcr}). The powers are negative for the one active switch channel, as the power meter console subtracts the DCR automatically, and no light reached the sensor during this time. Equation 8.3 is applied for the mean values with $\gamma = 580.3087$ and τ_* and $\tau_{\text{rec},50}$ as determined in Section 8.2.1.

8.4 Calibration measurement procedure

To calibrate the SNSPD system, a full Poincaré sphere scan was performed to determine $\eta_{\mathrm{sde,0,max}}$ and $\eta_{\mathrm{sde,0,min}}$ using the setup illustrated in Figure 8.4. Prior to the scan, the conversion ratio between the beamsplitter ports (γ) was determined using the setup and procedures discussed in Section 8.2.2.

The grid chosen for the Poincaré sphere scan is visualized in Figure 8.8. It was generated with a step width of 20° for both the polar angle (0° to 180°) and the azimuth angle (0° to 360°). Although a denser grid is theoretically preferable, a trade off was made to reduce the measurement time to a feasible timescale. Each polarization state was scanned for six minutes, yielding 18 values for the fully recovered SDE per measurement. Consequently, the overall measurement duration for the 146 polarization states was 14.6 hours, during which the optical setup had to remain undisturbed. Although components are secured inside the SNSPD rack using screws and tape, environmental disturbances inside the frequently visited laboratory are difficult to mitigate. Because an undisturbed measurement exceeding an overnight window would require extensive planning, the less dense grid was chosen. Following the data acquisition, $\eta_{sde,0}$ was determined for all scanned polarization states according to the procedures outlined in the previous section.

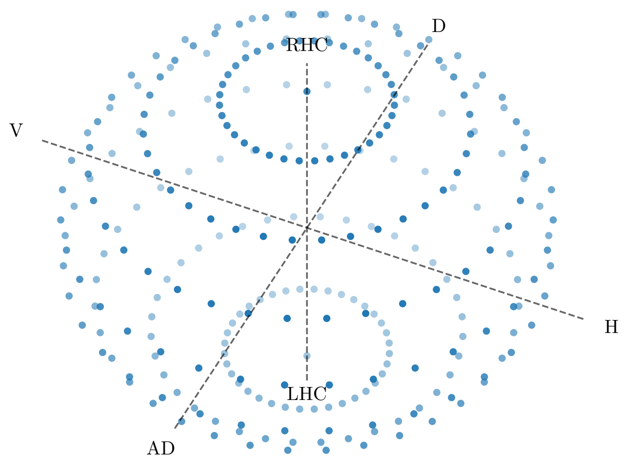

Figure 8.8: Scan grid utilized for the Poincaré sphere scan to identify the maximum and minimum fully recovered SDE.

Chapter 9

Results and discussion

9.1 Results of the transmission loss measurements

During both campaigns, the transmission losses were determined following the procedure outlined in Section 7.2 utilizing the setup shown in Figure 7.3. The measured losses for both days of the BGL measurement campaigns are presented in Table 9.1 and subsequently to calculate the respective system efficiency (η_{sys}) via Equation 7.1. An increase

Campaign date	$\text{Loss}_{\text{Coudé}}$ [dB]	$\text{Loss}_{\text{free-space}}$ [dB]	$\text{Loss}_{\text{fiber-segment}}$ [dB]	η_{sys}
08.08.2025	$-3.8\,\text{dB}$	$-1.3\,\text{dB}$	$-0.9\,\text{dB}$	0.251
04.11.2025	$-3.8\,\text{dB}$	$-1.3\,\text{dB}$	$-1.6\,\text{dB}$	0.214

Table 9.1: Results of the transmission loss measurement. $\text{Loss}_{\text{Coudé}}$ describes all losses accumulated from the telescope up until the first relay, $\text{Loss}_{\text{free-space}}$ the losses accumulated between the first relay and the fiber coupling and $\text{Loss}_{\text{fiber-segment}}$ the losses accumulated in the optical fiber path up until the SNSPD input.

in $\text{Loss}_{\text{fiber-segment}}$ is observed between the two campaigns days, which is most likely attributed to insufficient fiber cleaning or additional losses due to bending of the fiber. The provided losses for the telescope and Coudé train are based on the results from previous works [2].

9.2 Results of the SNSPD calibration

9.2.1 Determination of the power conversion ratio between reference and SNSPD

The γ-factor, describing the conversion ratio between the power measured with the reference sensor and the SNSPD (see Section 8.2.2), was determined with the optical optical illustrated in Figure 8.6. Figure 9.1 a) and b) show the results of the γ measurements prior to the calibration measurement, whereas the measurement depicted in c)/d) originate from an earlier test measurement. Each data set spans a measurement duration of one hour.
On short time scales, the γ-factor appears stable, whereas a clear drift over longer time scales can be identified. This drift is attributed to the drifting polarization state of the laser, as verified by a measurement shown in Figure 8.3, combined with the utilized single mode beamsplitter, which is non polarization maintaining and thus exhibits a small polarization dependency (see e.g. [33, 48]).
In addition to the small drifts in Figure 9.1 a), two large jumps are present at the start of the third hour. These were not observed in earlier and longer tests of the γ characterization setup (see Figure 9.1 c) and d)). As the jump is sudden and an almost steady state is reached afterwards, this observation is most likely explained by an external disturbance to the measurement setup that could not be further identified.
Table 9.2 combines all three measurements in a) and b) and provides the values for γ_{min}, γ_{max} and γ_{mean}. To exclude the disturbance during the third hour, the data is masked in the region between the start of the third measurement and the time at which the γ-factor reaches a more stable state (approximately after $\sim 8000\,\mathrm{s}$).
The impact of the long term fluctuations is deemed negligible for the calibration measurement. This assumption is justified by analyzing the impact of the fluctuations on the calculated fully recovered SDE ($\eta_{\mathrm{sde},0}$) by determining the maximum difference when calculating $\eta_{\mathrm{sde},0}$ with γ_{min} and γ_{max}. Figure 9.2 illustrates the differences calculated for each measured polarization state. Across all measured polarization states the maximal difference is 0.002815, when assuming the worst case scenario. The worst case scenario references the case where either γ_{min} or γ_{max} is used for the calculation but the other is the actual factor describing the ratio at the point of measurement.
For the calculations of $\eta_{\mathrm{sde},0}$ in Section 9.2.2, $\gamma_{\mathrm{mean}} = 580.3087$ is utilized as it provides an accurate estimation under the prior analysis of the introduced error.

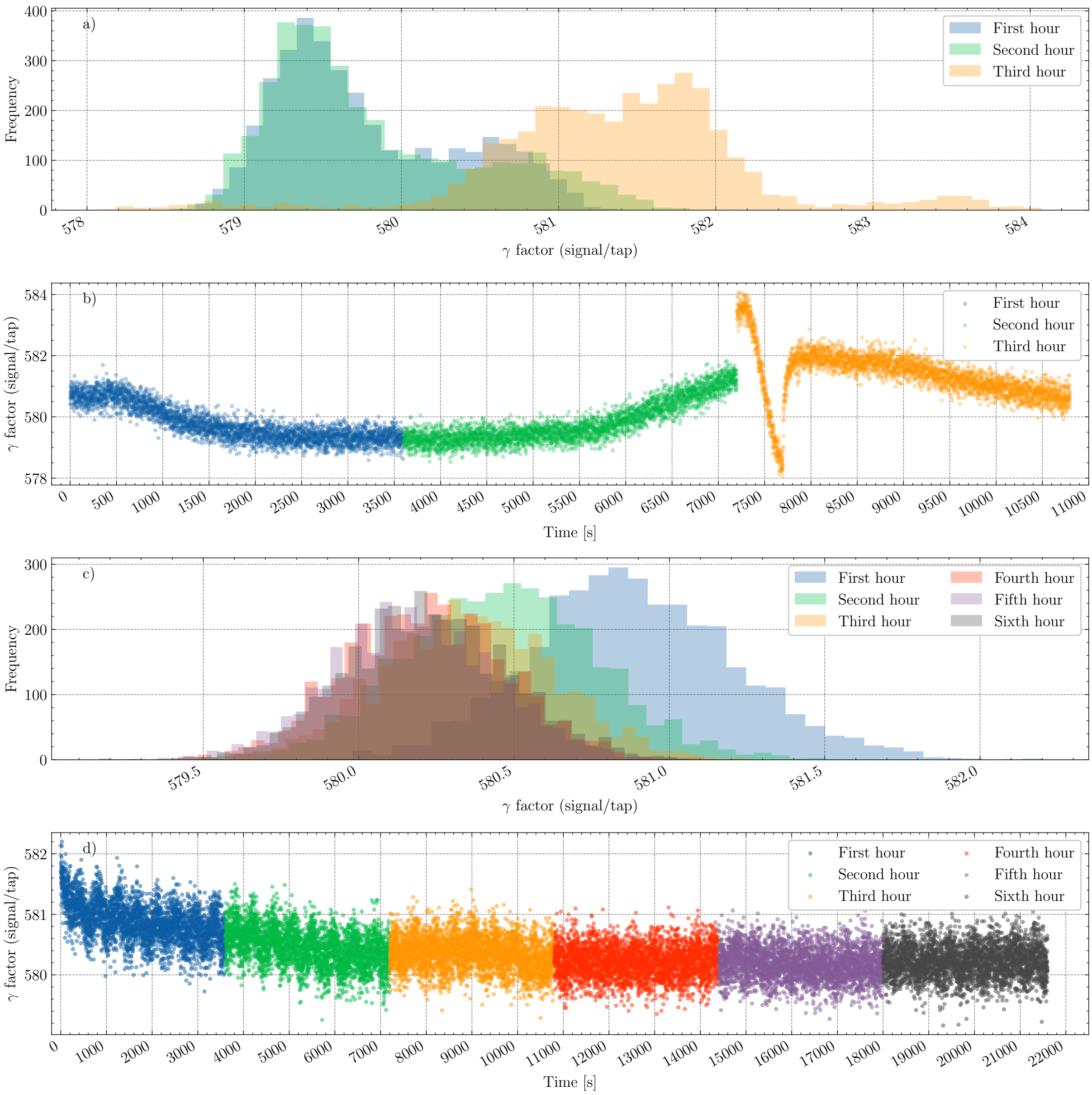

Figure 9.1: a)/b) Determined γ-factor during a three hours measurement prior to the Poincaré scan (see Section 9.2.2) . c)/d) Determined γ-factor during component tests over a six hour time period. Both were conducted with the setup described in Section 8.2.2.

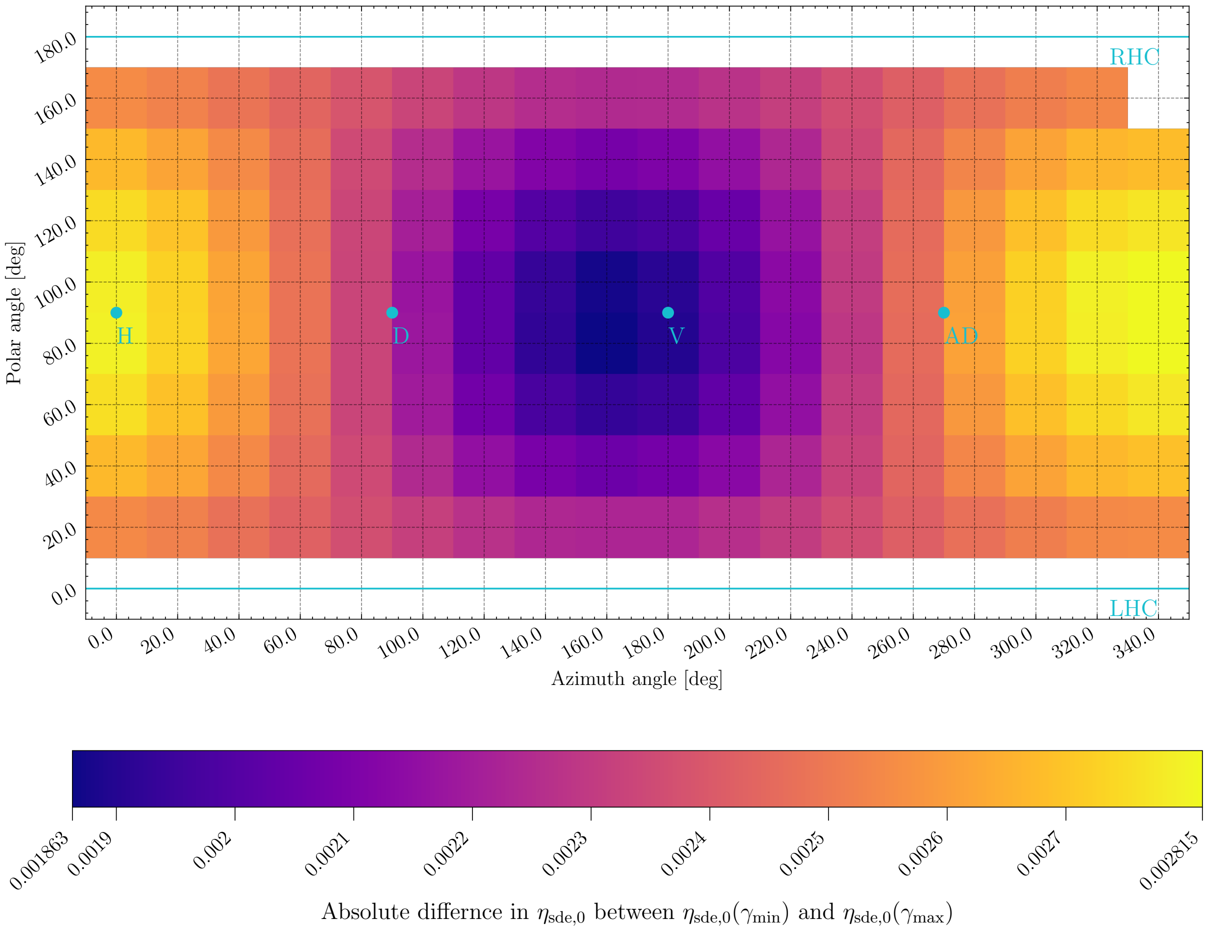

Figure 9.2: Impact of the fluctuation in the conversion ratio γ on the calculated fully recovered SDE ($\eta_{sde,0}$). The depicted absolute difference is determined by subtracting the results of the $\eta_{sde,0}$ calculation with the minimum and maximum γ-factor from Table 9.2. Each intersection of gridlines equals a calculated value. Marked are the six principal polarization's: horizontal, diagonal, vertical, anti-diagonal, left hand circularly and right hand circularly. Measurements for the latter two and the data point (340°,160°) are missing due to the measurement being stopped, because the evaporation cycle of the SNSPD restarted.

	γ-factor Measurement results			
	Minimum	Maximum	Mean	Standard deviation (mean)
First hour	578.5824	581.6969	579.7806	0.5838
Second hour	578.5239	581.8348	579.8114	0.6686
Third hour (masked)	579.9165	582.5940	581.3340	0.5073
Across all measurements	578.5239	582.5940	580.3087	

Table 9.2: Results of the determination of the γ-factor in the conversion ratio measurement prior to the SNSPD calibration measurement.

9.2.2 Results of the calibration measurement

For the determination of the the maximum and minimum fully recovered SDE, a full Poincaré sphere (described in Section 8.4) was conducted with the setup illustrated in Figure 8.4. The results of this scan are depicted in Figure 9.3. At the top, the results are mapped to the Poincaré sphere using the *griddata* function from *SciPy*, setting the interpolation method to „nearest“. Marked are the six principal polarizations, right hand circularly (RHC), left hand circularly (LHC), horizontal (H), vertical (V), diagonal (D) and anti-diagonal (AD). At the bottom, the data is depicted in two dimensions. For each polar and azimuth angle pair, the values are mapped to the same color map chosen for the spherical illustration. In this depiction, it is apparent that some data points are missing, explicitly, the measurement for the right hand circularly and left hand circularly polarizations, as well as the data point at the polarization with 160° polar angle and 340° azimuth angle. As the evaporation cycle of the SNSPD restarted, the measurement had to be stopped.

Nonetheless, the scan shows that the maximum $\eta_{\text{sde},0}$ can be observed for the polarization state described by (Q,U,V) = (0.925,−0.337,−0.174) with $\eta_{\text{sde},0,\text{max}} = 0.407$, whereas the minimum is observed for the polarization state described by (Q,U,V) = (−0.925,0.337,0.174) with $\eta_{\text{sde},0,\text{min}} = 0.270$ [1].

However, even the maximum value underestimates the value provided by ID Quantique ($\eta_{\text{sde},0} = 0.85$), by a factor of 2.08. This rather large deviation can most likely be attributed to two distinct measurement characteristics. ID Quantique conducted their calibration under optimized bias current settings and measured with lower count rates.

[1] Due to the specific generation of the grid (see Section 8.4), the horizontal and vertical polarization were not included in this scan. It is highly likely, that the minimum and maximum should be observed for these polarization states.

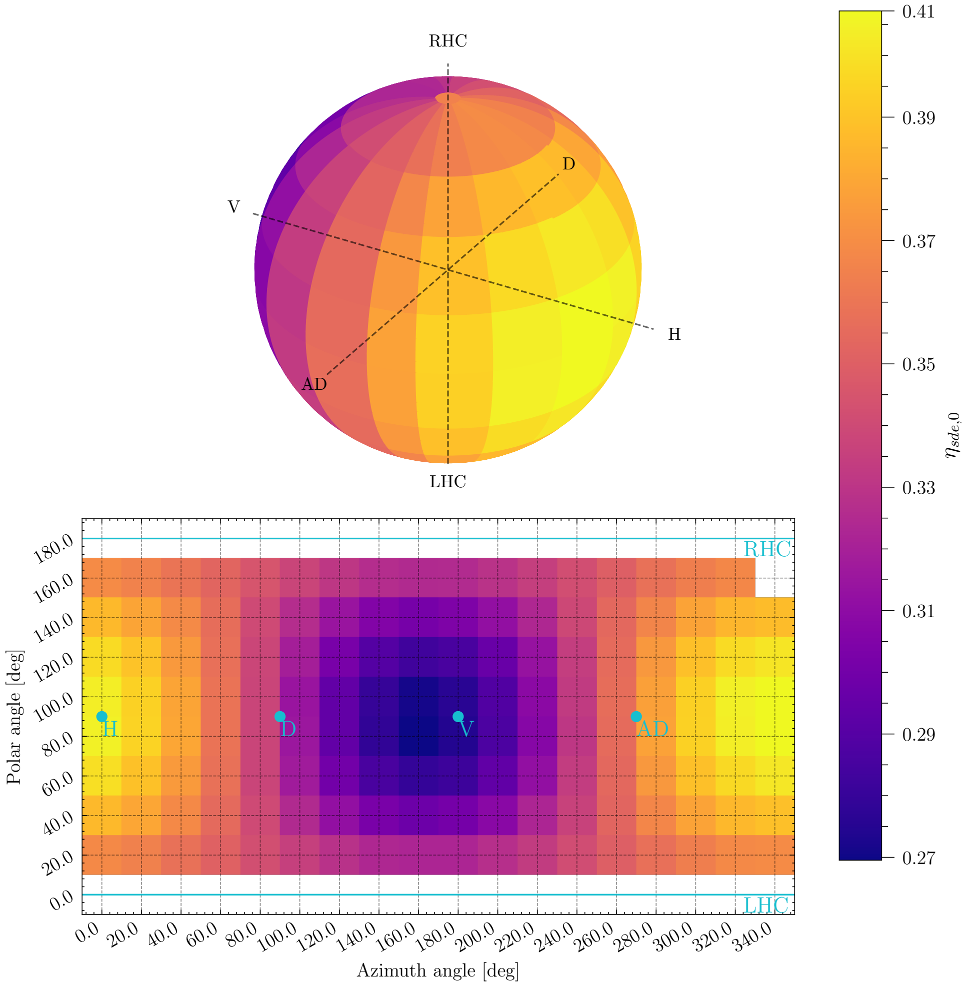

Figure 9.3: Results of the SNSPD calibration measurement, presenting the calculated fully recovered SDE. At the top, depiction on the Poincaré sphere; at the bottom, depiction in 2D. Each crossing of gridlines equals one calculated SDE. Marked are the six principal polarization's: horizontal, diagonal, vertical, anti-diagonal, left hand circularly and right hand circularly. Measurements for the latter two and the data point (340°,160°) are missing due to the measurement being stopped, because the evaporation cycle of the SNSPD restarted.

A non ideal bias current can influence the $\eta_{\text{sde},0}$ and DCR by a significant margin, as shown in Figure 3.4. As the results suggest, it is likely that the calibration measurement was conducted in a non ideal regime. Furthermore, the calibration measurement was conducted with higher count rates, as the power was attenuated to be within the limits of the SNSPD and reference sensor, but no further attenuation was added to the optical path leading to the SNSPD to keep the optical paths to both sensors identical. Consequently, a correction formula, Equation 5.3, was introduced. If the calibration is conducted with lower count rates, where the arrival time between photons is larger than the recovery time of the detector, the calculation would simplify to

$$\eta_{sde,0} = \frac{h \cdot c \cdot (R_{\text{sig}} - R_{\text{dcr}})}{\lambda \cdot \gamma \cdot P_{\text{ref}}}$$

With the results of this calibration measurement, a foundation for a third iteration of the calibration measurement was built, which aims to verify the correction formula and optimize the bias current using the current setup. As this iteration is not part of this work, it was decided to employ the value provided by ID Quantique ($\eta_{sde,0} = 0.85$) and use the correction formula for the analysis of BGL, combined in Euqation 5.9, until further verification and testing of the setup is conducted. In addition, BGL, as measured by the setup described in Section 7.1, is highly unpolarized, therefore, in the final iteration of the calibration measurement, the discrete polarization scramble method of the PSY-201 polarization controller[2] should be applied to determine the average $\eta_{\text{sde},0}$ for unpolarized light.

[2]The interface used for the calibration already provides an option to control this mode remotely. For more information refer to Section D.2

9.3 Results of the background light measurements

In the following sections, the results of the BGL measurements will be discussed individually for daytime, sunset and nighttime measurements. For specific information on each measurement campaign, refer to Section 7.3.3. Throughout each section, the term „measured radiance(s)“is used synonymously with BGL, as BGL is quantified in units of radiance.

9.3.1 Daytime measurements

08.08.2025, measurement azimuth 45° Figure 9.4 depicts the results for the measurement series taken between 14:27 and 15:36 local time. During the measurement, the Sun was almost in the opposite azimuth direction to the telescope viewing direction (compare with the radar plot in Figure 9.4). Towards higher zenith pointing directions, the angular separation between the telescope and the Sun decreases, causing more radiation to scatter into the FOV of the telescope, causing the measured radiances to increase. Closer to the surface,corresponding to larger zenith angles, the measured radiances increase due to the major contributions of light reflected by the surface.
The simulations predict a very similar behavior to the measured radiances. However, they underestimate the measured radiances across the entire zenith angle range, by a factor ranging from 1.77 at the zenith to a peak value of 2.97 at 40°, which decreases toward the surface to 2.29 at 60° and 2.30 at 70°.
The measured radiance at 40° is a significant outlier in the measurement series. This anomaly was not caused by a sudden increase of detected photons, given that the standard deviation across the measurement is among the lowest in this measurement series at $0.004\,\mathrm{mW\,nm^{-1}\,m^{-2}\,sr^{-1}}$ for an average of radiance of $2.183\,\mathrm{mW\,nm^{-1}\,m^{-2}\,sr^{-1}}$. The exact cause of this sudden increase might be explained by certain reflections from cranes at the construction site close to the institute, or by a cloud that remained unnoticed during the measurement. Clouds, due to their inherent brightness (up to $240\,\mathrm{mW\,nm^{-1}\,m^{-2}\,sr^{-1}}$ [37]), can cause a significant increase in the observed radiance as observed during sunset measurements in Waterloo (Figure 4 in [29]), where two almost identical measurements were conducted under clear-sky and partly clouded sky conditions.

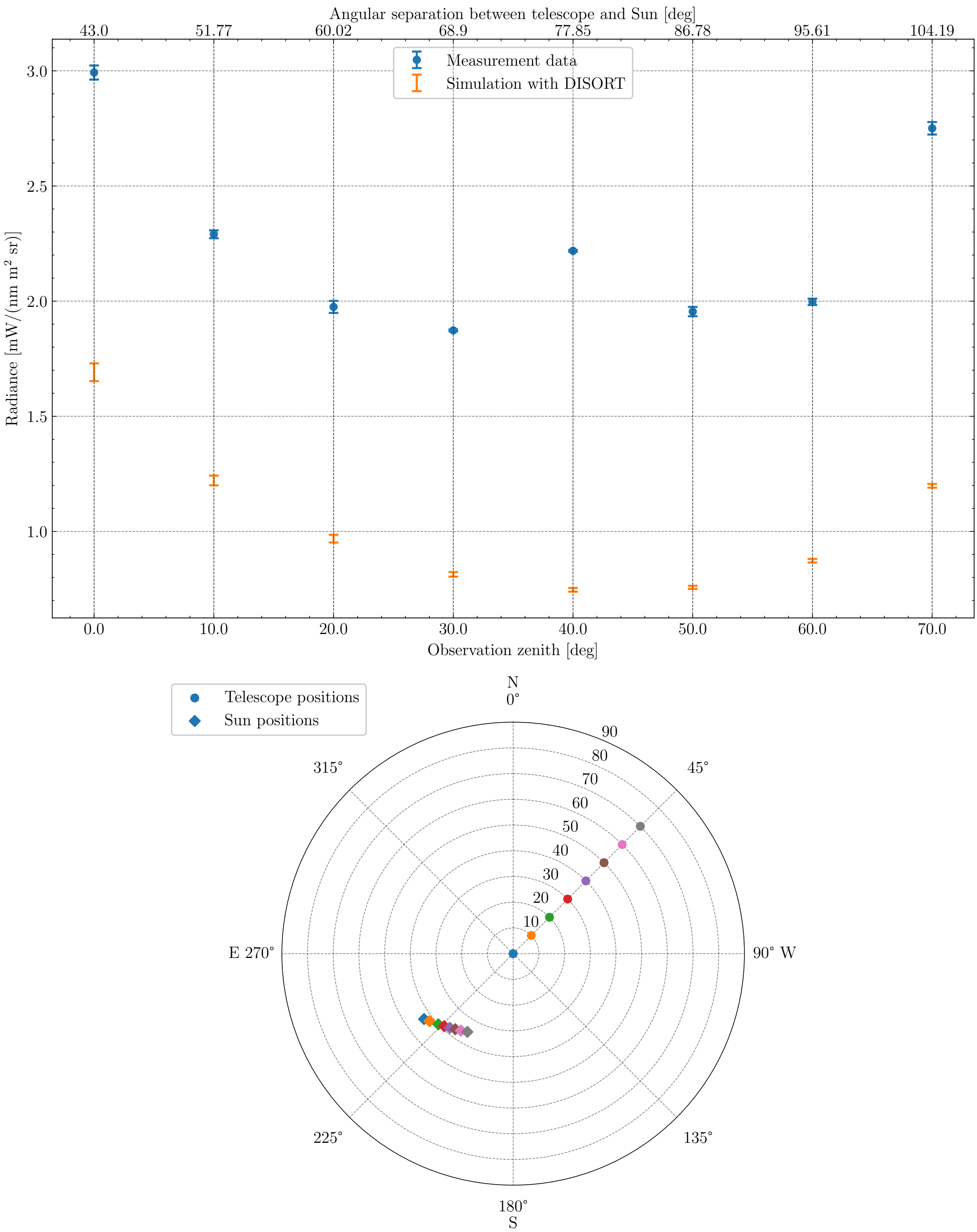

Figure 9.4: Results of the daytime measurement series at a 45° azimuth viewing direction on the 08.08.2025. At the top, the measured radiances are depicted with error bars representing the standard deviation. The simulated radiances are displayed as error bars to visualize the range of the simulation results for each measurement (settings can be found in Section C.6). An additional x-axis at the top indicates the angular separation from the Sun. At the bottom, the positions of the telescope and the Sun are shown, where matching colors represent the same measurement.

Excluding the outlier, the increase toward larger zenith angles may be explained by the complex reflective properties at the surface and, to some extent, by internal reflections inside the telescope dome because the telescope is not shielded. In the simulations shown in Figure 9.4, the albedo and visibility settings (0.15 and 30 km) are based on previous observations for the location in Oberpfaffenhofen measured with the collimator setup described in Section 3.2.3[28]. By adjusting the employed albedo value while maintaining a constant visibility of 30 km, the results can be marginally improved. This improvement is visualized in Figure 9.5, which depicts the correlation between measured and simulated radiances for varying albedo and visibility settings. The correlation is expressed via the median ratio between measured and simulated radiances taken across all observed zenith angles in Figure 9.4. For a visibility of 30 km, an increase in albedo can improve the overall underestimation up to a median ratio of 1.563.

However, typical albedo values for the viewing direction should be dominated by a mixture of albedos for grass (~ 0.3) , asphalt (~ 0.15) and construction concrete ($\sim 0.3 - 0.4$). Hence, an increase to values exceeding 0.4 is difficult to justify. A point can be made that in close proximity to the OGS, higher albedos are to be expected due to the presence of metallic materials at the construction site. These materials vary greatly in albedo depending on the type with for example 0.8 for Aluminium or 0.3-0.5 for (oxidized) steel[3]. With these limitation regarding a reasonable albedo, an albedo significantly higher than 0.4 cannot be justified. When comparing this albedo value with the best achieved ratios in Figure 9.5, at best, a ratio of 1.748 can be reached for a constant visibility of 30 km, which is deemed feasible for clear sky conditions. More accurate results for the entire measurement series can be achieved with visibility's below 30 km.

A selection of simulations featuring different visibility and albedo settings is shown in Figure 9.6, with the original configurations from Figure 9.4 plotted in orange. An increase in albedo primarily affects the simulations close to the surface due to the heightened impact of reflected light, as seen when comparing the simulations plotted in orange and purple. Conversely, altering the visibility shifts the simulated radiances across the entire zenith range within a similar order of magnitude due to an increase in scattering events, as seen when comparing the simulations plotted in purple and red. Although adjusting these settings improves the simulation results, a visibility of 15 km may be unrealistic for clear-sky conditions. Consequently, the settings cannot be the sole reason for the deviations. This conclusion is further reinforced when comparing these results with the BGL measurement data from Waterloo (see Section 3.2.4), where adjustments of the albedo and visibility within a justifiable regime led to better predictions.

Beside the simulation settings, the most likely cause for deviations between measured and

[3]The albedo estimates were taken from Figure 2 in [58] and from the ECOSTRESS library [44].

simulated radiances is the characterization of the measurement setup, which is complex due to the amount of optical components involved. A change in certain parameters could influence the conversion from count rates to radiances according to Equation 5.9. While most of the parameters can be assumed to be determined with sufficient accuracy, the greatest uncertainty is most likely introduced by the transmission loss / system efficiency η_{sys}.

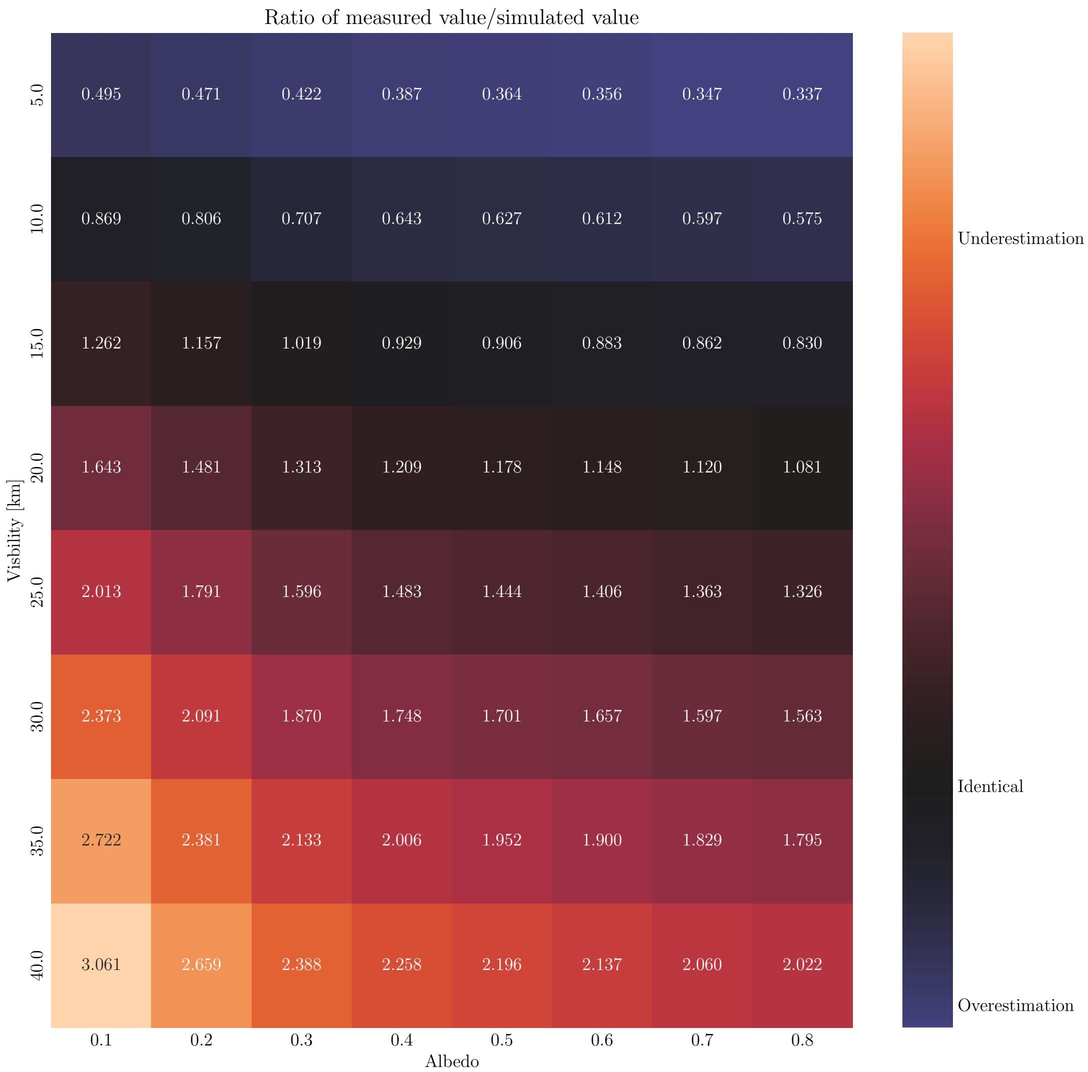

Figure 9.5: Median ratio between measured and simulated radiances for the 45° daytime measurement series under different albedo and visibility settings. Each block represents a median of all ratios across the different zenith angles. For this measurement series, the outlier at a zenith angle of 40° was excluded in these simulations. Values larger than unity describe and underestimation of the measured radiances, whereas values greater describe and overestimation.

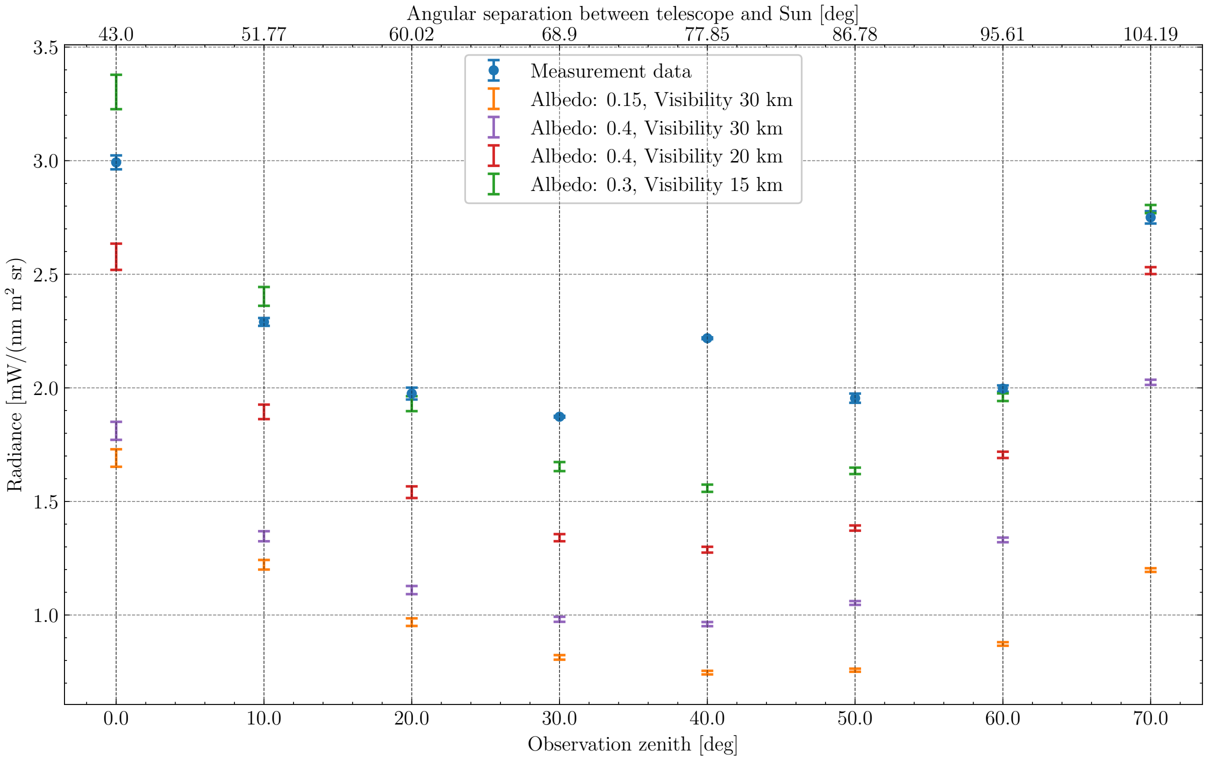

Figure 9.6: Multiple simulation results with varying settings for the measurement series at a 45° azimuth viewing direction. An increase in the visibility shifts the simulated radiances across the entire zenith range within a similar order of magnitude, while an albedo change affects the radiances close to the surface by a larger margin than at smaller zenith angles.

08.08.2025, measurement azimuth 135° The measurement series for an azimuth angle of 135° was performed between 17:43 and 19:01 local time and is depicted in Figure 9.7. In this direction, another campus building is located in close proximity at a height slightly below the OGS. The measured radiances close to the surface at zenith angles of 60° and 70° are larger than those observed in the prior measurement (see Figure 9.4), even though the angular separation between telescope position and the Sun is larger and the Sun is at a higher zenith angle. In addition, the simulated radiances underestimate the measured radiances by an even larger margin than observer in the previous measurement series, with discrepancies ranging from 2.3 for the zenith to 4.2 for a zenith angle of 70°. Even if the albedo is varied within a reasonable range up to 0.4, the deviation at high zenith angles of 60° and 70° is only reduced to 3.4 and 3.2 respectively. Furthermore, contrary to the previous measurement series in Figure 9.4, the measurement and the simulation do not depict similar trends. At zenith angles below 20°, the measured radiances decrease slightly, while the simulated radiances continuously increase for zenith angles smaller than 30°. However, when the telescope is moved close to the zenith, the telescope itself might block some parts of the scattered radiation, which could explain the observed decrease. Overall, the daytime simulations cannot be matched with the measured radiances for either of the two presented measurement series. While some qualitative sources for these deviations can be highlighted, they require further analysis and verification.

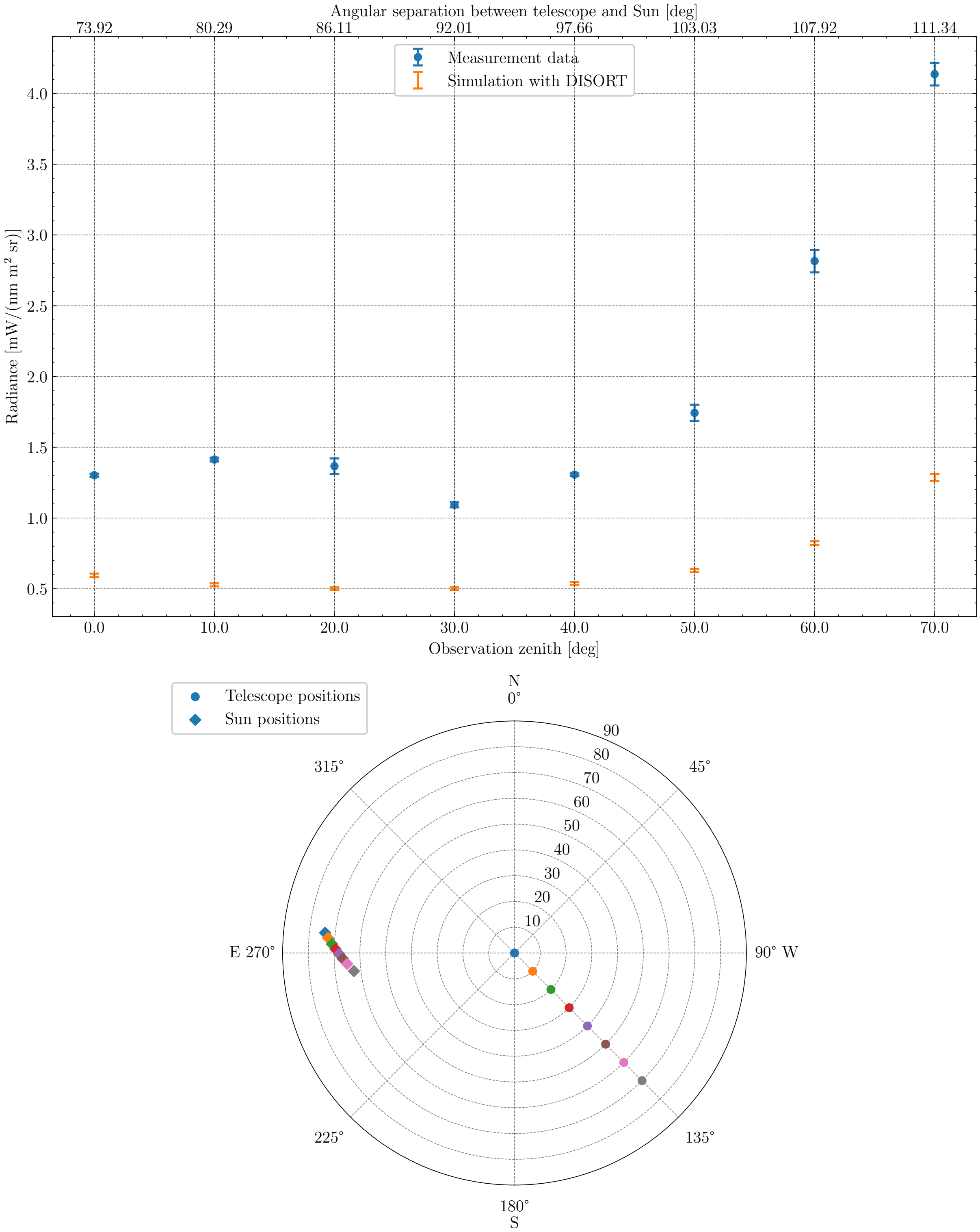

Figure 9.7: Results of the daytime measurement series at a 135° azimuth viewing direction on the 08.08.2025. At the top, the measured radiances are depicted with error bars representing the standard deviation. The simulated radiances are displayed as error bars to visualize the range of the simulation results for each measurement (settings can be found in Section C.6). An additional x-axis at the top indicates the angular separation from the Sun. At the bottom, the positions of the telescope and the Sun are shown, where matching colors represent the same measurement.

9.3.2 Sunset measurement

To measure the BGL during the sunset, the telescope was pointed toward the zenith and a long term measurement was performed on the 08.08.2025 from approximately 17:00 to 22:20 local time. Figure 9.8 depicts the results of this measurement, showing the measured radiance alongside simulations featuring both DISORT and MYSTIC as solvers (for detailed settings refer to Section C.6). The secondary x-axis at the top represents the solar zenith angle, replacing the angular separation used in the previous graphical representations. Until approximately 19:20 the sky radiance increases before starting to gradually decrease. Once the Sun reaches a zenith angle of 87°, the measured sky radiance drops sharply from $0.978\,\mathrm{mW\,nm^{-1}\,m^{-2}\,sr^{-1}}$ at 20:15: to $0.158\,\mathrm{mW\,nm^{-1}\,m^{-2}\,sr^{-1}}$ at 20:35:48 with a corresponding solar zenith angle of 90.2°. At around 21:00 local time the measured radiances drop below $3\times10^{-3}\,\mathrm{mW\,nm^{-1}\,m^{-2}\,sr^{-1}}$, reaching almost near zero values. Hence, the time axis was cut at 21:15, as no further changes in radiance were observed.

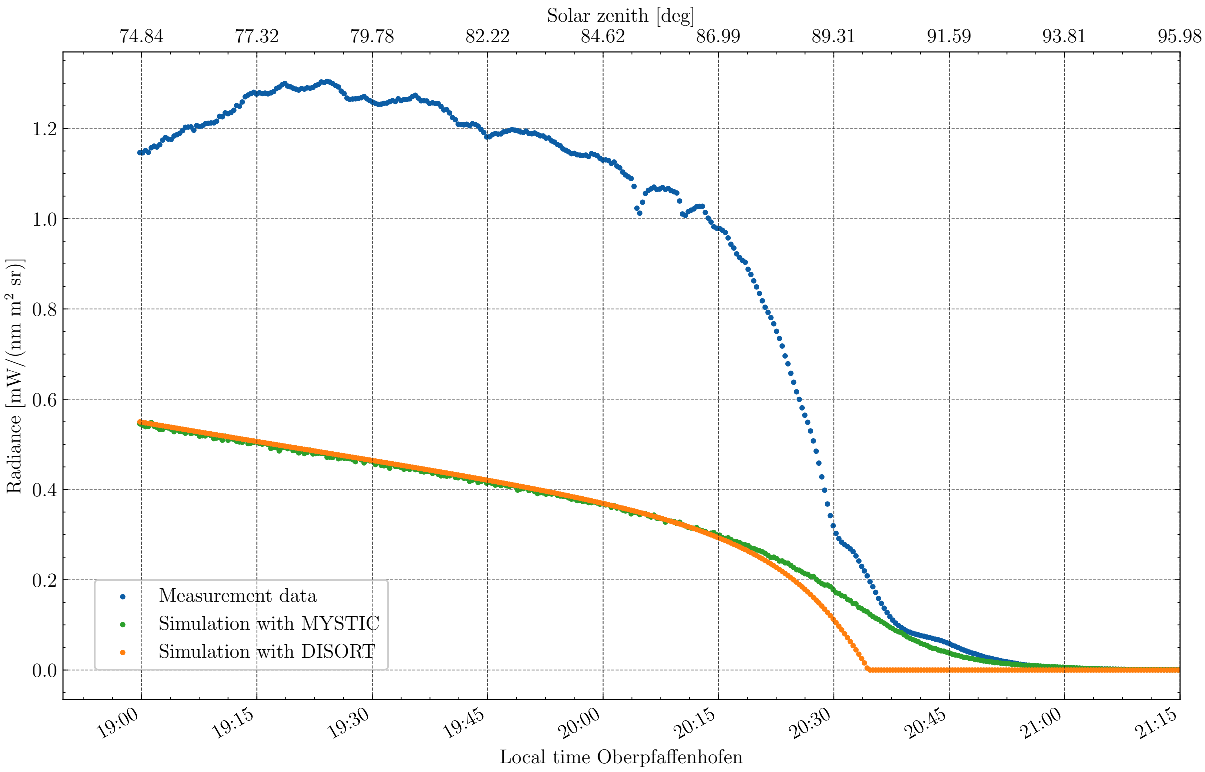

Figure 9.8: Results of the long term sunset measurement on the 08.08.2025 at the zenith position. Simulated radiances are displayed for the MYSTIC and DISORT solver. The settings can be found in Section C.6.

Both solvers underestimate the measured radiances by a significant margin, with DISORT showing a worse performance due to the use of its standard 1D plan-parallel atmosphere. However, these results align with the prior measurement in Waterloo (see Figure 9.9) utilizing the collimator setup. Even though a direct comparison is constrained by the different optical setups and observation positions, both measurements hint at limited simulation capabilities during sunset scenarios. As the setup in Waterloo was only characterized based on the manufacturer specifications, and the analysis in 9.3.1 hints at an inaccurate characterization of the setup, further measurements with a completely characterized BGL measurement device are necessary, to verify the capabilities of simulations during sunset.

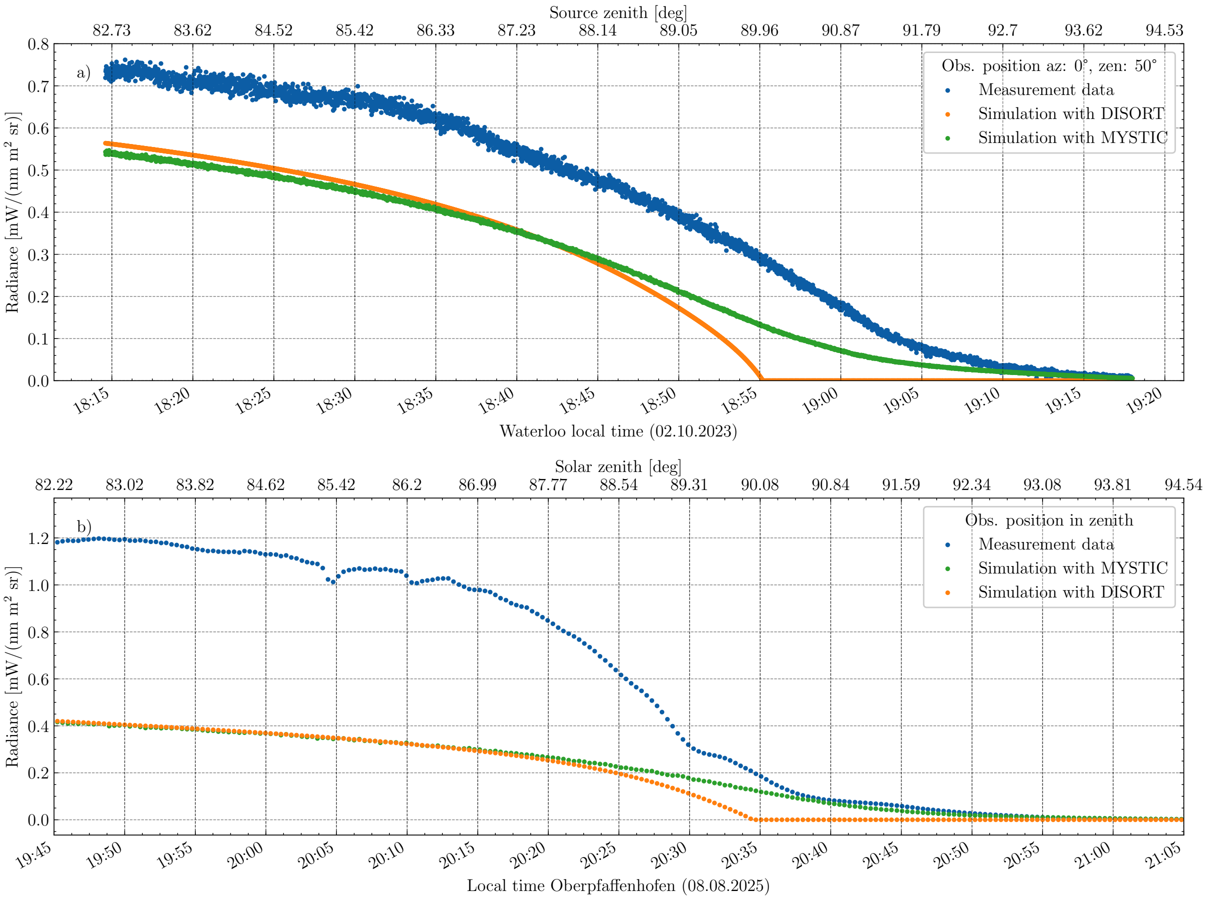

Figure 9.9: a) Results of the long term sunset measurement in Waterloo on the 02.10.2023 from [29] at a 0° azimuth and a 50° zenith angle. b) Results of the long term sunset measurement on the 08.08.2025 at zenith position. For both, simulated radiances are displayed for the MYSTIC and DISORT solver. The settings can be found in Section C.6.

9.3.3 Nighttime measurements

08.08.2025, measurement azimuth 75° Figure 9.10 depicts the results of the first night measurement, which was performed between 22:26 and 00:11 local time when the telescope was pointed towards Munich. The highest radiance of $0.000\,24\,\mathrm{nW\,nm^{-1}\,m^{-2}\,sr^{-1}}$ was observed at an zenith angle of 80°, the measurement closest to the surface. Similarly to the daytime measurements, the observed radiances decrease towards the zenith, though a sharper drop is visible after 70°. This drop is also not predicted by the simulations, which instead predict a gradual decrease.

Close to the surface, anthropogenic light generated by the campus buildings and the construction site in the immediate surroundings of the OGS should account for this behaviour. As the telescope points further from the surface, the impact of anthropogenic light decreases. Because the simulations only include the Moon as the sole BGL source, this behaviour cannot be predicted accurately. Comparing the measured radiances close to the surface with the simulations results reveal that only $\sim 6\%$ of the measured radiance at an zenith angle of 80° and $\sim 4\%$ at 70° should be attributed to the Moon. Overall, the simulations only attribute for only $\sim 4\%$ to $\sim 5\%$ of the measured radiances across all other zenith angles. In addition, the simulations predict a monotonic decrease that is not reflected by the measured radiances. The slow decay in the measured radiances is expected to be caused by the light pollution from the city of Munich, which was clearly visible on the day of measurement despite the city center being approximately 22 km from the OGSOP.

Due to the complexity of BGL during the night, mainly driven by anthropogenic light, an underestimation by simulations only incorporating the lunar radiance was expected. Nevertheless, the impact of different albedo and visibility combinations on the deviations was analyzed and visualized in Figure 9.11. These results further support the hypothesis that BGL during the night is more complex than during the day, as no major improvements can be achieved by simply adjusting the albedo and visibility parameters. Another distinct observation during this measurement series is the larger standard deviation of the measured radiances across all measurement angles. Contrary to the daytime measurements, where the standard deviations typically remain on the order of 1% or less, the minimum standard deviations during this nighttime measurement series was reached close to the surface at a zenith angle of 70° and 80° with approximately 14%. For smaller zenith angles, the standard deviation reached values of up to 44%.

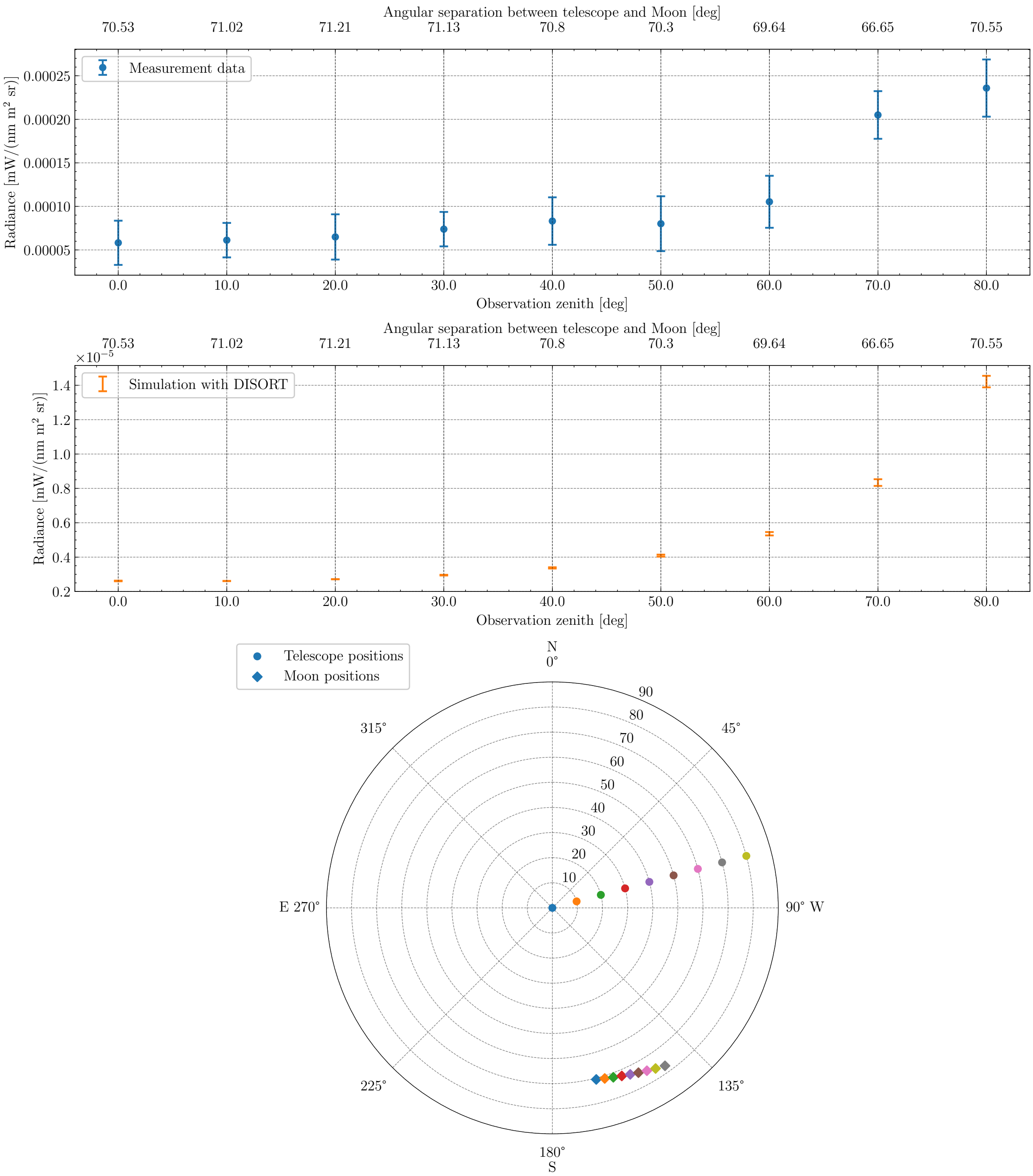

Figure 9.10: Results of the nighttime measurement series at a 75° azimuth viewing direction on the 08.08.2025. At the top, the measured radiances are depicted with error bars representing the standard deviation. The simulated radiances are displayed as error bars to visualize the range of the simulation results for each measurement (settings can be found in Section C.6). An additional x-axis at the top indicates the angular separation from the Moon. At the bottom, the positions of the telescope and the Moon are shown, where matching colors represent the same measurement.

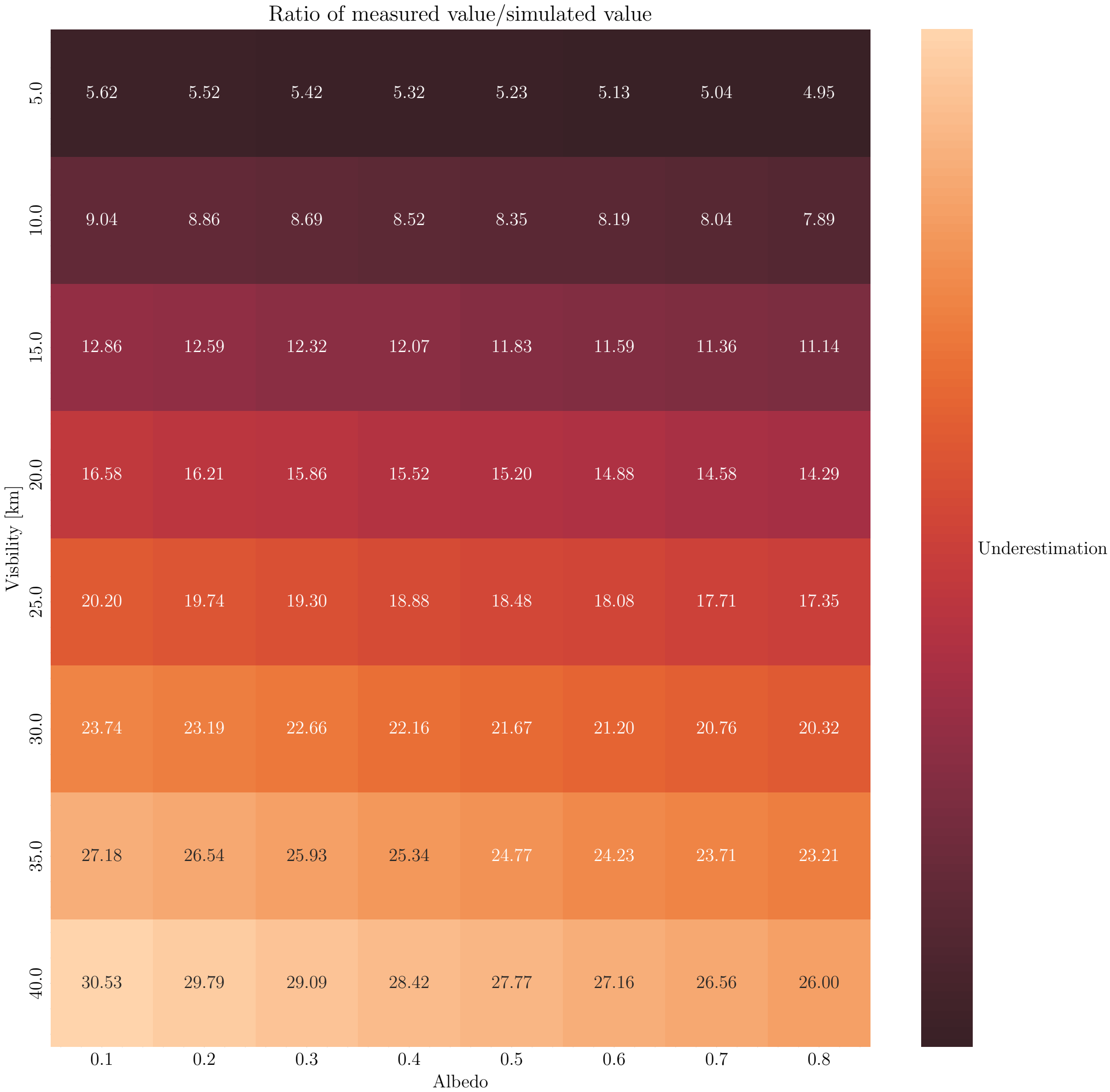

Figure 9.11: Median ratio between measured and simulated radiances for the 75° night-time measurement series under different albedo and visibility settings. Each block represents a median of all ratios across the different zenith angles. Values larger than unity describe an underestimation of the measured radiances.

Due to these elevated fluctuations, the measured signal count rate was compared with the measured DCR in Figure 9.12. Despite the high standard deviations, an overlap between the signal count rate and the DCR is rare and only observed close to the zenith. However, the faint BGL becomes challenging to distinguish from the DCR and is only possible reliably achieved due to the implementation of the optical switch into the measurement setup, enabling the estimation of the current DCR (see Section 7.1).

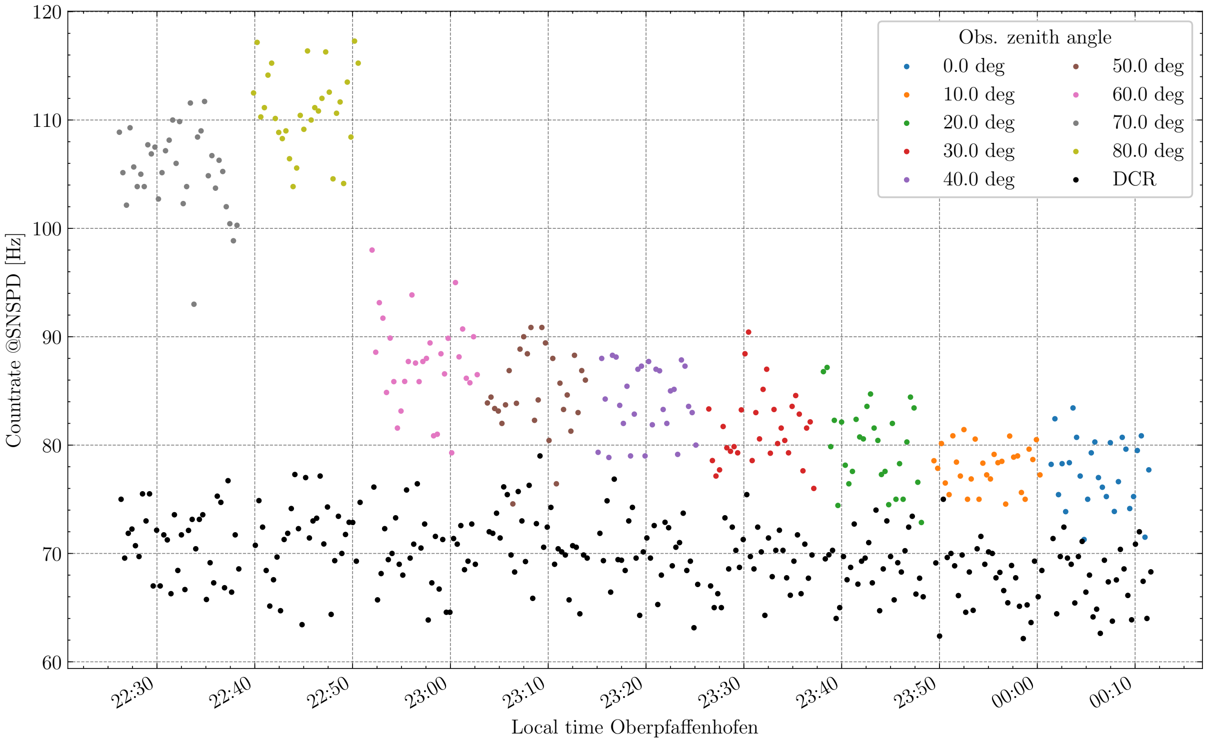

Figure 9.12: Measured countrates at the SNSPD for the nighttime measurement series at a 75° azimuth viewing direction. For each zenith angle, the DCR (in black) and count rates including signal and DCR (colored) are displayed over the measurement time.

04.11.2025, measurement azimuth 150° While the angular separation between the Moon and telescope remained close to 70° for the measurement series with an azimuth viewing direction of 70° (see Figure 9.10), the angular separation for the measurement series at an azimuth angle of 150° (see Figure 9.13) exhibits a larger variance. At zeniths angles of 24° and 36°, the separation was particularly small, reaching values of 12.6° and 13.9° respectively. Comparing these values, with the radar plot in Figure 9.13, it is apparent that for a zenith angle of 24° the separation is mainly driven by a difference in azimuth angle, whereas for 36° the separation is caused by a major difference in azimuth position.

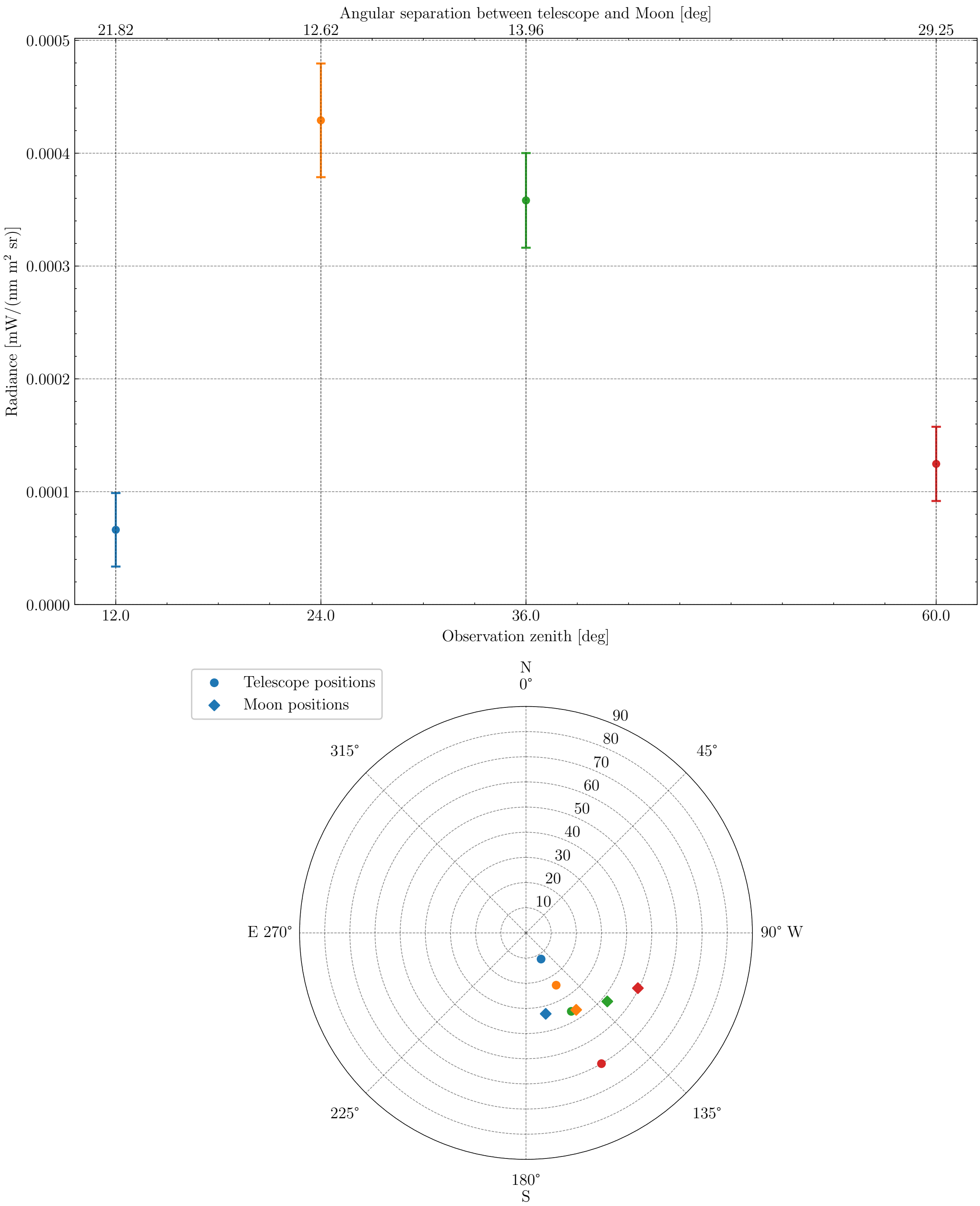

Figure 9.13: Results of the nighttime BGL measurement series at a 150° azimuth viewing direction on the 04.11.2025. At the top, the measured radiances are depicted with error bars representing the standard deviation. An additional x-axis at the top indicates the angular separation from the Moon. At the bottom, the positions of the telescope and the Moon are shown, where matching colors represent the same measurement.

For both observation positions, a severely elevated radiances are measured. The measured radiances exceed the results in the 75° measurement series (visualized in Figure 9.14), reaching values of up to 0.0043 $\mathrm{mW\,nm^{-1}\,m^{-2}\,sr^{-1}}$ compared to the previously observed 0.00024 $\mathrm{mW\,nm^{-1}\,m^{-2}\,sr^{-1}}$, even though no anthropogenic light or major sources of light pollution was present in the 150° azimuth viewing direction. Due to the proximity of the telescope pointing direction to the full Moon, this increase in measured radiances is fully attributed to lunar radiance. Nonetheless, when conducting simulations with the settings outlined in Section C.6[4], only $\sim 7.8\%$ of the measured radiance at a zenith angle of 24° and $\sim 9.9\%$ at a zenith angle of 36° are predicted. While potential errors stemming from the characterization of the measurement setup were discussed in Sections 9.3.1 and 9.3.2, these most likely do not explain the large deviations observed in this measurement.
To validate the simulation approach implemented for nighttime measurements, further measurements with similar angular separations are required. During the measurement campaign on the 04.11.2025, with a measured system efficiency of 0.214, tests confirmed that the telescope can track the Moon without exceeding the maximum count rate of the SNSPD. Consequently, a direct scan of the Moon would be possible to confirm the simulation approach, assuming the setup characterization is refined.

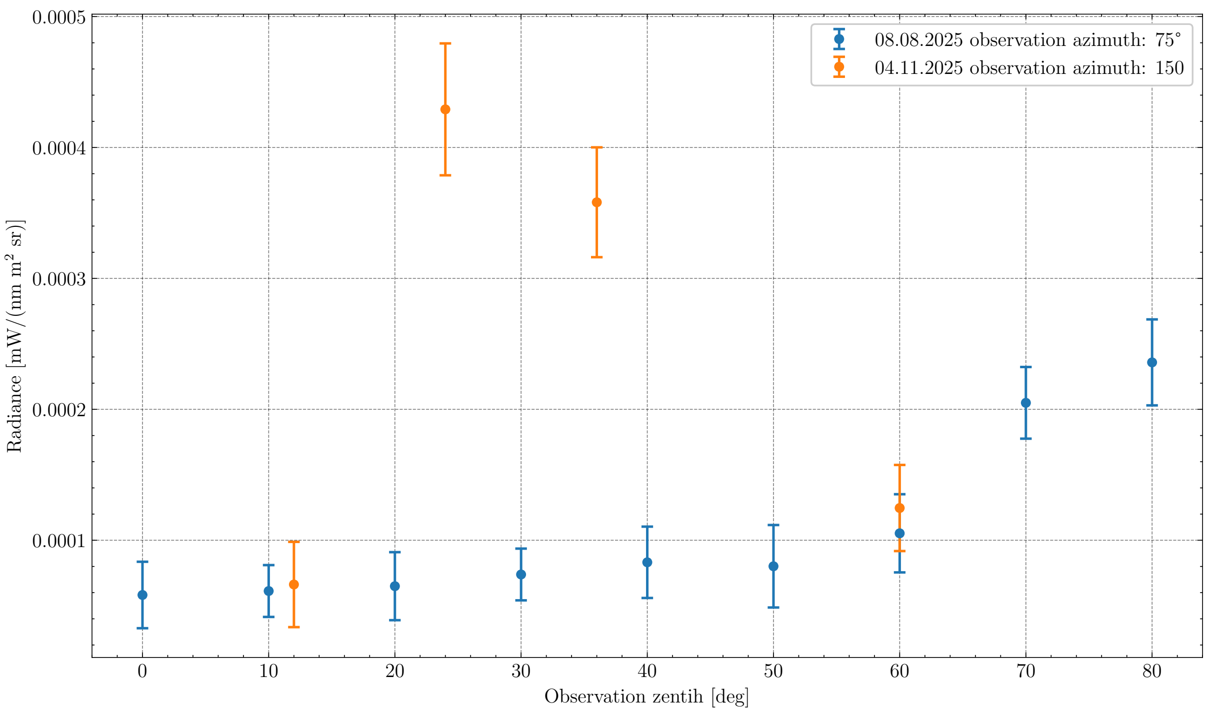

Figure 9.14: Comparison between the measured radiances at the 75° and 150° azimuth viewing directions.

[4]The settings applied for this measurement series are identical to the settings for Figure 9.10.

04.11.2025, measurement azimuth 0° Contrary to the measurement series for an azimuth viewing direction of 75° and 150°, the measurement series in 0° viewing direction does not feature any major BGL apart from the campus buildings and the construction site close to the surface. In Figure 9.15, the influence of the anthropogenic light remains slightly visible at an observation zenith angle of 60°, with radiances reaching a similar order of magnitude as in the measurement series for 75°. Because the immediate surroundings and sources of anthropogenic light in both azimuth viewing directions are very similar (see Table 7.2), this was to be expected.

However, at smaller zenith angles (12° and 24°), the standard deviations of the measured radiances indicate that certain data points take negative values. The underlying reason is clarified in Figure 9.16, where the measured signal count rates are compared with the DCR. For most zenith positions, a substantial overlap between these count rates is visible. Because the viewing direction is dominated by agricultural fields, there are no major BGL sources. In addition, the Moon was at the opposite site of telescope pointing direction (see radar plot in Figure 9.15), reducing its contributions via scattering events, even though the angular separation is smaller than in the measurement series at an azimuth viewing angle of 75°.

Based on these observations, it is reasonable to conclude that the noise contributions of BGL for the OGSOP is dominated by the DCR if no prominent light source is present in the viewing direction or in close vicinity of it. Such sources include anthropogenic light from campus buildings, substantial light pollution from major urban areas like Munich, or direct and reflected contributions from the Moon. Furthermore, this measurement has validated the integration of the optical switch, as without a momentarily precise DCR estimation, distinguishing low levels of BGL from the DCR is significantly more complex which could lead to a loss of data.

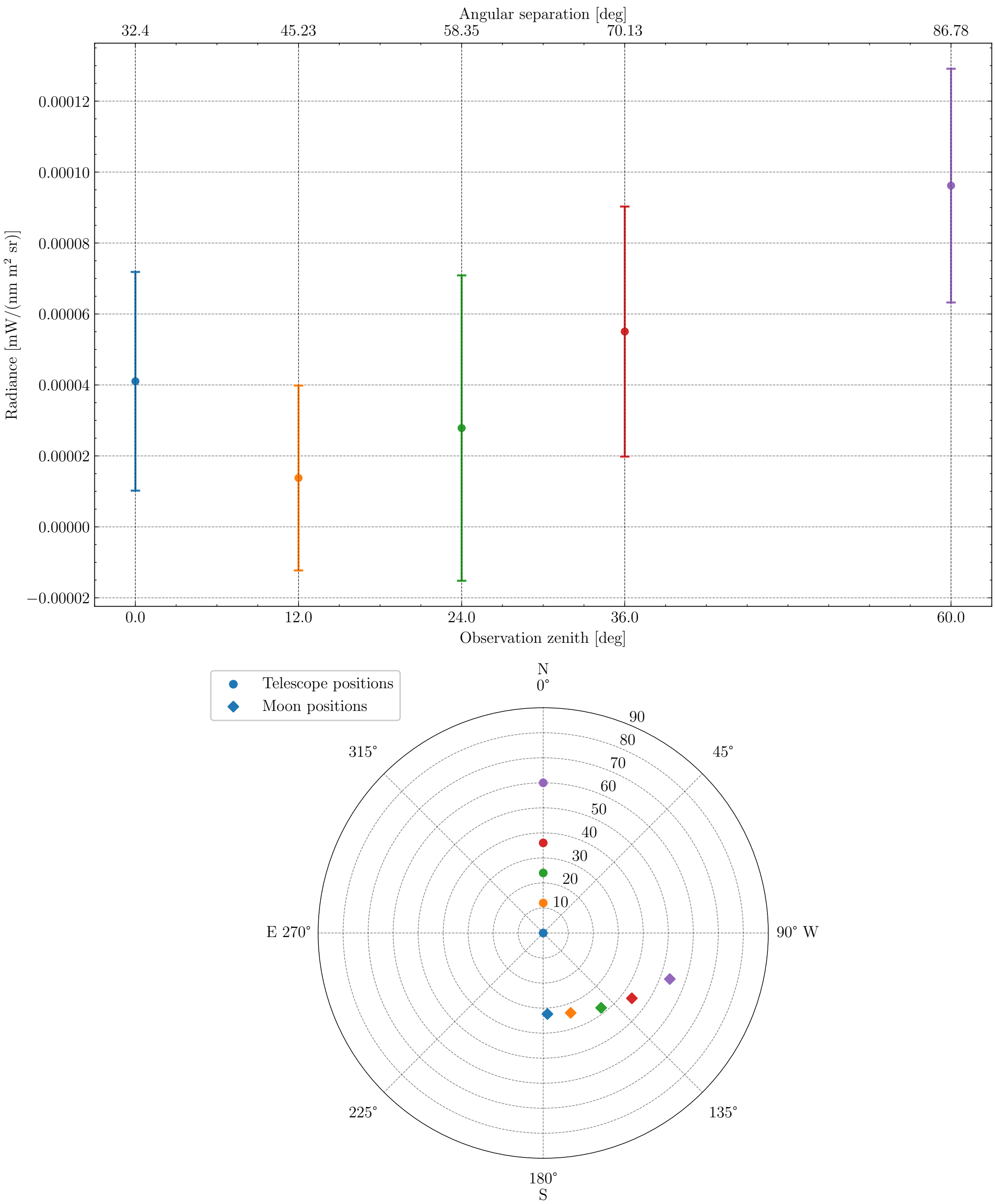

Figure 9.15: Results of the nighttime measurement series at a 0° azimuth angle on the 04.11.2025. At the top, the measured radiances are depicted with error bars representing the standard deviation. An additional x-axis at the top indicates the angular separation from the Moon. At the bottom, the positions of the telescope and the Moon are shown, where matching colors represent the same measurement.

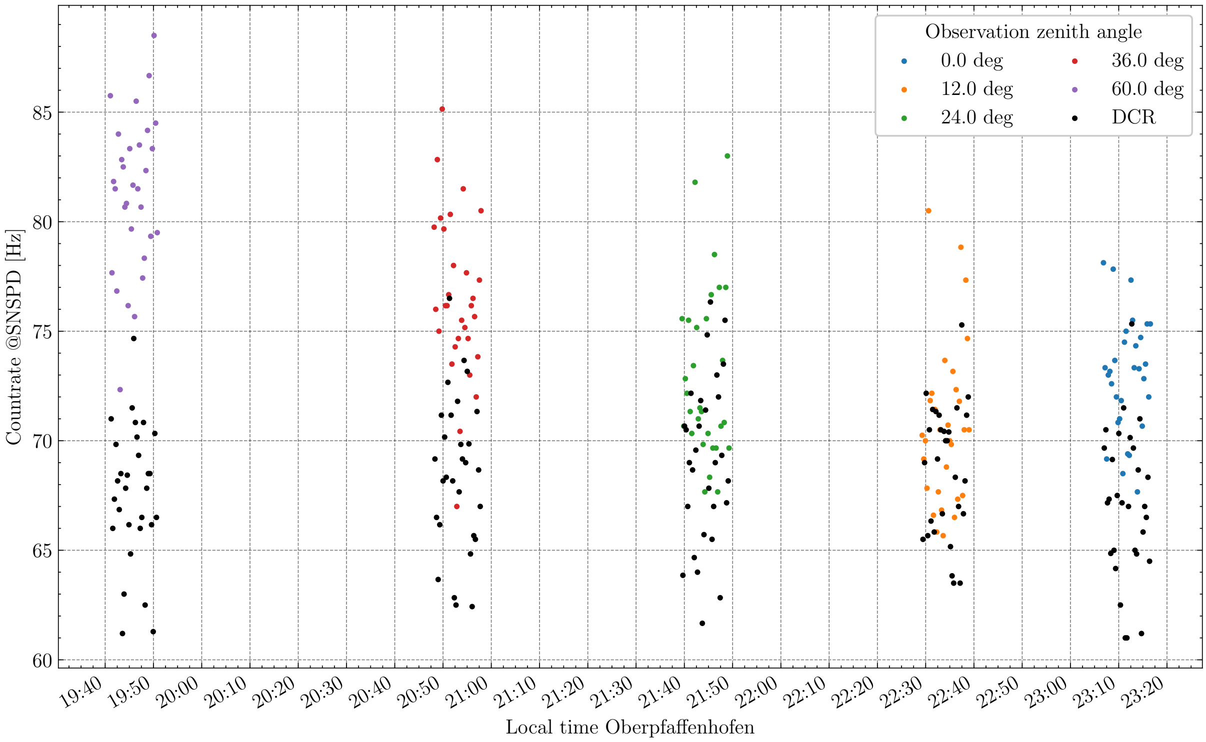

Figure 9.16: Measured countrates at the SNSPD for the nighttime measurement series at a 0° azimuth angle. For each zenith angle, the DCR (in black) and countrates including signal and DCR (colored) are displayed over the measurement time.

Chapter 10

Conclusion and outlook

In the framework of this thesis, the OGSOP, which was designed to enable QKD downlinks, was utilized characterize BGL in a realistic QKD setup and compare it with simulation tools. Because the optical setup of the OGSOP enables SMF coupling, a SNSPD system was deployed for the detection of BGL.

The fully recovered system detection efficiency of the SNSPD system was determined by designing and building a parallel power measurement setup utilizing a calibrated reference sensor (see Section 8.1). A formalism and routine were established, to derive the efficiency from the measured count rate of the SNSPD and power of the reference sensor (see Section 8.2). To apply the formalism, the conversion ratio between the power measured at the SNSPD and the reference sensor was determined in a separate experiment (see Section 9.2.1). Subsequently, a full Poincaré sphere scan was conducted (see Section 9.2.2) to determine the maximum and minimum efficiency of the polarization-dependent detector utilizing a web interface developed for the automation of the calibration procedure.

The results of the calibration measurement, $\eta_{\text{sde,0,min}} = 0.407$ and $\eta_{\text{sde,0,max}} = 0.270$ at a different polarization, deviated from the provided value $\eta_{\text{sde,0}} = 0.85$ (see Section 9.2.2). After thorough analysis and discussion, two main reasons were identified: first, the calibration measurement was most likely conducted using a non optimized bias current, and second, the high calibration power complicated the derivation of $\eta_{\text{sde,0}}$ such that the a correction formalism (see Equation 5.3) had to be included. To verify the correction formalism and the presented measurement results, the developed setup and routine should be employed in the next iteration of the calibration measurement to optimize the bias current using lower calibration powers.

For the BGL measurements, a setup incorporating an optical switch for consecutive signal and DCR measurements was built and a measurement routine was established (see Chapter 7). This routine includes the characterization of the transmission loss and verification of fiber alignment (see Section 7.2) conducted prior to each measurement. With the automated data acquisition (see Section 7.3), multiple measurement campaigns were conducted under clear-sky conditions during the day, sunset and night, and the results were compared with simulations and prior measurements utilizing a collimator setup (see Section 7.3.3 and 3.2.4). Previous works focused on a proof of concept utilizing the standard setup of libRadtran to compare BGL measurement data with simulations for daytime measurements. As part of this work, to compare the measurement results with the simulation for all conducted campaigns, the simulation approach was extended to incorporate the Moon as a BGL source by calculating the spectrum of the Moon for the performed measurements using LIME.

Analysis of the daytime BGL measurements showed radiances between $1.09\,\mathrm{mW\,nm^{-1}\,m^{-2}\,sr^{-1}}$ and $4.17\,\mathrm{mW\,nm^{-1}\,m^{-2}\,sr^{-1}}$, which were heavily dependent on the separation between the Sun and the telescope and thus the measurement time, and likely the telescope architecture when measuring close to the zenith due to presumably vignetting (see Section 9.3.1). A comparison of the measured radiances with simulations and prior measurement indicates potential inaccuracies regarding the transmission loss characterization, which partially relied on previous works (see Sections 7.2 and 9.1), as the simulation results could not be matched to the measured radiances like in prior observations using a collimator setup. Similar observations were made for the sunset measurement. However, the observation that simulation tools cannot accurately predict BGL during sunset measurements aligned with previous observations, thereby reinforcing the hypotheses (see Figure 9.9).

The nighttime measurements (see Section 9.3.3) provided great insight into the impact of BGL. Across all measurements, the influence of anthropogenic light at observation zenith angles greater than 60° was identified. Furthermore, it was demonstrated that the light pollution of Munich is observable with the OGSOP (see Figure 9.10). The BGL contributions of the Moon were identified for angular separations between the telescope and the Moon of less than 14° reaching radiances of up to $0.0043\,\mathrm{mW\,nm^{-1}\,m^{-2}\,sr^{-1}}$. Compared to the observed $0.00023\,\mathrm{mW\,nm^{-1}\,m^{-2}\,sr^{-1}}$ close to the surface at a zenith angle of 10°, these results highlight the importance of the Moon as a BGL source when the telescope is positioned near to the Moon's position (see Figures 9.14 and 9.13). If the OGSOP was pointing opposite of the Moon and no other major anthropogenic light sources were in the the viewing direction of the telescope, it was shown that the DCR and signal count rates were more difficult to distinguish demonstrating that the DCR partially dominates the BGL as a noise source under these conditions (see Figures 9.15 and 9.16). This result in particular verified that integrating the optical switch into a BGL measurement setup is of essential, to clearly distinguish BGL and DCR at low levels of BGL. Comparing the results with the simulation incorporating the Moon as a BGL source showed a severe underestimation, which partially can be attributed to the variety of BGL sources playing a major role during nighttime as well as the characterization issues of the complex optical setup of the OGSOP.

With the OGSOP now capable to be used for BGL measurements for QKD scenarios, key insights on the necessary calibration methods and key parameters for such a setup were gained to efficiently measure BGL with an OGS. The performed measurements provided the first BGL measurement data in the C-band during the day and night for an OGS utilizing SMF coupling. Quantitative and qualitative comparisons of the measurement data with simulations and the collimator setup utilized in previous works showed that for a comparison setup, collimator setups are preferred. To further analyze the impact of BGL, additional measurement data must be collected over longer time periods and at different locations, as planned in the ESA project BLAM. Overall, the experiments presented in this thesis aid the analysis of BGL in QKD scenarios to enable accurate system designs with regard to spectral, temporal and spatial filtering techniques in space and on the ground.

Appendix A

Optical and electrical components

Table A.1: Summary of all and optical components

Component	**Manufacturer**	**Specifications**
Time Tagger	Swabian Instruments	Time Tagger Ultra
Optical Switch	Agiltron	FFSM-126C01332 series switch module 1×2 configuration Polarization maintaining
SNSPD	ID Quantique an IonQ company	ID 281 SNSPD system fully recovered SDE ($\eta_{sde,0}$): 0.85 Recovery time: 73.132 ns see Section 8.2.1 Max. detection rate: 30×10^6 cps Operating temperature: 0.8 K Cooling: cryogenic, condensation cycle

Table A.1: Summary of all and optical components

Component	Manufacturer	Specifications
Photodiodes	Thorlabs	S154C used at the tap port of the beamsplitter S122C used at the signal port of the beamsplitter Power range S122C: 50 nW - 40 mW Power range S154C: 100 pW - 3 mW
Beamsplitter	Thorlabs	Coupling ratio: 99.9:0.1 Center wavelength: 1550 nm Bandwidth: 15 nm Single mode
Laser	ID Photonics	CoBrite tunable Laser (Sc type) Minimum power: 7.6 mW Polarization maintaining output
Polarization controller	Luna Innovation	Polarization Synthesizer/Analyzer PSY-201 Minimum power: 318.2 nW

Appendix B

Conversion parameters

Table B.1: Summary of all parameters used for radiance conversions according to Equation 5.9.

Parameter	**Value**	**Origin**
Centner Wavelength λ	1565 nm	Center wavelength of the dichroic mirror.
Effective bandwidth λ_{eff}	34.9 nm	Calculated based on provided data.
Receiver diameter $\mathrm{D_{rx}}$	80 cm	Fixed by the telescope.
Effective focus length $\mathrm{f_{OGS}}$	3865 nm	Calculated for the optical setup by a colleague.
Mode field diameter MFD	10.4 µm	Taken from datasheet.
Optical system efficiency η_{sys} 08.08.2025 η_{sys} 04.11.2025	 0.251 0.214	MEasured and calculated according to the methodology outlined in Section 7.2

Table B.1: Summary of all parameters used for radiance conversions according to Equation 5.9.

Parameter	**Value**	**Origin**
SDE of the SNSPD η_{sde}	-	Calculated for each measurement according to Equation 5.3 with the parameters below.
Fully recovered SDE $\eta_{sde,0}$	0.85	Provided by ID Quantique.
Fitting parameter τ_*	12.767 ns	Determined as described in Section 8.2.1.
Recovery time at 50% $\tau_{\text{rec},50}$	73.132 ns	Determined as described in Section 8.2.1.

Appendix C

Simulation settings

In this chapter, all input parameters for BGL simulations and lunar spectra calculations using LIME[1] are summarized in their order of appearance. For all simulations the *TSIS-1 HSRS spectrum* is utilized as the solar spectrum and the wavelength of 1565 nm is selected[2]. The source position is calculated based on the geographic coordinates of the OGSOP (altitude: 650 m, longitude: 11.277 98°E, latitude: 48.084 76°N) and the middle timestamp of the BGL measurement (see Sections 6.2 and 6.3) or the provided local time. To calculate both source positions with the same tools, the *zenith* tool of libRadtran is not utilized, but instead, the *Astropy* package with the DE440 ephemerides data [52] is utilized.

C.1 Simulation settings for Figure 3.7

For the simulation across the whole solar spectrum the DISORT solver was employed with the following fixed parameters:

Observation				Aerosol		
Azimuth	Zenith	Visibility	Albedo	Haze	Season	Local time
42°	38°	30 km	0.15	urban	fall/winter	23.12.2025 14:00

Table C.1: Settings for the simulations depicted in Figure 3.7.

[1]For LIME, the most recent coefficients at the time of writing this thesis have been employed (*20251010_v1*).

[2]This wavelength is equal to the center wavelength of the dichroic mirror implemented in the BGL measurement setup.

C.2 Simulation settings for Figure 3.10 a

Solar simulations were conducted using MYSTIC tracing 10^6 photons for a fixed solar position with each built-in aerosol composition of libRadtran (rural, urban, tropospheric and maritime). The local time was selected to reflect the solar position at its highest reached elevation (∼65°) on the 13.06.2026. A grid was generated to simulate radiances for the entire hemisphere. Therefore the azimuth and zenith angles were varied between 0° to 360° and 0° to 90° respectively in 5° steps. As libRadtran cannot handle observation zenith angles of 90° (see Section 6.1), 89° is substituted as an approximation.

Observation				Aerosol		
Azimuths	Zeniths	Visibility	Albedo	Haze	Season	Local time
0° to 360°	0° to 90°	30 km	0.15	varies	spring/summer	13.06.2026 13:11

Table C.2: Settings for the simulations depicted in Figure 3.10 a).

C.3 Simulation settings for Figure 3.10 b

To compare the radiances for varying solar positions, four solar positions were chosen. These positions include the Sun at zenith (zenith 0°), the Sun at sunset (zenith 89° and azimuth 270°) and two intermediate positions at the same azimuth angle and zenith angles of 60° and 30°. A grid was generated to simulate radiances for the whole hemisphere. Therefore the azimuth and elevations angles were varied between 0° to 360° and 0° to 90° respectively in 5° steps. As libRadtran cannot handle observation zenith angles of 90° (see Section 6.1), 89° is substituted as an approximation.

Observation				Aerosol		
Azimuths	Zeniths	Visibility	Albedo	Haze	Season	Local time
0° to 360°	0° to 90°	30 km	0.15	rural	spring/summer	-

Table C.3: Settings for the simulations depicted in Figure 3.10 b).

C.4 Simulation settings for Figures 6.1 and 6.2

For each observer position in Figure 6.1, simulations were conducted every five minutes between 01.07.2026 05:30 to 01.07.2026 21:00 with spring/summer season settings and 01.12.2026 08:00 to 01.12.2026 16:00 with fall/winter season settings. MYSTIC was employed as the solver tracing 10^6 photons. Otherwise the settings remained identical for each observer position.

Observation Azimuths	Observation Zeniths	Visibility	Albedo	Aerosol Haze	Aerosol Season & Local time
0°, 90°, 180° and 270°	20° and 0° once	30 km	0.15	rural	varies

Table C.4: Settings for the simulations depicted in Figure 6.1.

For Figure 6.2, the observer position at an azimuth angle of 180° azimuth and zenith angle of 20° was chosen to repeat simulations on a smaller timescale using varying temporal resolutions (5 min, 1 min, 30 s and 15 s) between 01.07.2026 11:30 to 01.07.2026 11:40 with spring/summer season settings. In addition, to calculate a data point at 11:30, simulations had to be conducted at 11:25/11:29/11:29:30 and 11:29:45.MYSTIC was employed as the solver tracing 10^6 photons.

Observation				Aerosol		
Azimuth	Zenith	Visibility	Albedo	Haze	Season	Local time
180°	20°	30 km	0.15	rural	spring/summer	varies

Table C.5: Settings for the simulations depicted in Figure 6.2.

C.5 Simulation settings for Figures 6.6 and 6.7

For each observer position in Figure 6.6, simulations were conducted every five minutes between 30.06.2026 22:25 to 01.07.2026 06:00 local time with spring/summer season settings and 22.12.2026 14:40 to 23.12.2026 07:25 local time with fall/winter season settings. MYSTIC was employed as the solver tracing 10^6 photons. Otherwise the settings remained identical for each observer position.
The lunar spectra were calculated with LIME such that the maximum temporal difference between a simulation time and the time for which the lunar spectrum has been calculated does not exceed five minutes.

Observation				Aerosol	Aerosol Season &
Azimuths	Zeniths	Visibility	Albedo	Haze	Local time
0°, 90°, 180° and 270°	20° and 0° once	30 km	0.15	rural	varies

Table C.6: Settings for the simulations depicted in Figure 6.6.

For Figure 6.7, the observer position at an azimuth angle of 180° azimuth and zenith angle of 20° was chosen to repeat simulations on a smaller timescale using varying temporal resolutions (5 min, 1 min, 30 s and 15 s) between 22.12.2026 21:00 to 22.12.2026 21:10 with fall/winter season settings. In addition, to calculate a data point at 21:00, simulations had to be conducted at 20:55/20:59/20:59:30 and 20:59:45.MYSTIC was employed as the solver tracing 10^6 photons. As the depicted time period covers ten minutes, the lunar spectrum was calculated at 22:12:2026 21:05 local time and was employed for all simulations ensuring the same temporal difference criteria as above was met.

Observation				Aerosol		
Azimuth	Zenith	Visibility	Albedo	Haze	Season	Local time
180°	20°	30 km	0.15	rural	fall/winter	varies

Table C.7: Settings for the simulations depicted in Figure 6.7.

C.6 Simulation settings for background light analysis

In the following paragraphs, the simulations setting for each figure in the results chapter are summarized. Parameters not explicitly provided for each measurement include:

1. Wavelength → Fixed to 1565 nm due to the the dichroic in the measurement setup (see Section 7.1).

2. Exact timestamp used for the lunar spectra calculation → Middle timestamps for each observation position. Refer to section 6.3 for the procedure.

3. Exact timestamp used for the source position calculation → Refer to section 6.2 for the procedure.

4. Aerosols → Fixed to rural for all simulations based on the results from measurements in Oberpfaffenhofen with the collimator setup [28].

,

Table C.8: Simulation settings for all BGL measurements presented in Chapter 6.

Figure	**Settings**
Figure 9.4	**Observation azimuth angle:** 45° **Observation zenith angles:** 0° - 70° (10° steps) **Season:** spring/summer **Albedo:** 0.15 **Visibility:** 30 km **Solver:** DISORT
Figure 9.5	**Observation azimuth angle:** 45° **Observation zenith angles:** 0° - 70° (10° steps) **Season:** spring/summer **Albedo:** 0.1 - 0.8 (0.1 steps) **Visibility:** 5 km - 40 km (5 km steps) **Solver:** DISORT **Note:** Simulations are performed for each observation position with each visibility and albedo combination.
Figure 9.6	**Observation azimuth angle:** 45° **Observation zenith angles:** 0° - 70° (10° steps) **Season:** spring/summer **Albedo & visibility combinations:** 0.15 & 30 km, 0.4 & 30 km, 0.4 & 20 km, 0.3 & 15 km **Solver:** DISORT **Note:** Simulations are conducted for each albedo and visibility pair.

Table C.8: Simulation settings for all BGL measurements presented in Chapter 6.

Figure	**Settings**
Figure 9.7	**Observation azimuth angle:** 135° **Observation zenith angles:** 0° - 70° (10° steps) **Season:** spring/summer **Albedo:** 0.15 **Visibility:** 30 km **Solver:** DISORT
Figure 9.8 & 9.9	**Observation azimuth angle:** - **Observation zenith angle:** 0° (pointing directly at the zenith) **Season:** spring/summer **Albedo:** 0.15 **Visibility:** 30 km **Solver:** DISORT & MYSTIC **Photon number for MYSTIC:** 10^6 **Note:** DISORT was employed without pseudospherical corrections. The settings for the Waterloo measurement can be found in [29].
Figure 9.10	**Observation azimuth angle:** 75° **Observation zenith angles:** 0° - 80° (10° steps) **Season:** spring/summer **Albedo:** 0.15 **Visibility:** 30 km **Solver:** DISORT **Note:** Lunar spectra are calculated according to the procedure outlined in Section 6.3.

Table C.8: Simulation settings for all BGL measurements presented in Chapter 6.

Figure	**Settings**
Figure 9.11	**Observation azimuth angle:** 75° **Observation zenith angles:** 0° - 80° (10° steps) **Season:** spring/summer **Albedo:** 0.1 - 0.8 (0.1 steps) **Visibility:** 5 km - 40 km (5 km steps) **Solver:** DISORT **Note:** Simulations are performed for each observation position with each visibility and albedo combination. Lunar spectra are calculated according to the procedure outlined in Section 6.3.

Appendix D

Experiment control software

Multiple Python web interfaces were developed utilizing the *bokeh* package. The fundamental capabilities of these interfaces are outlined in the following sections. Experiment control and data acquisition was achieved through the interfaces for the following measurement:

1. BGL measurements with or without the optical switch. Refer to Chapter 7 for the measurement setup and procedures, Figure D.1 for a visual illustration and Table D.1 for a comprehensive list of input parameters.

2. SNSPD calibration measurements with various options for polarization control. Refer to Chapter 8 for the measurement setup and procedures, Figure D.2 for a visual illustration and Table D.2 for a comprehensive list of input parameters.

3. Determination of the γ-factor used on the SNSPD efficiency calculation. Refer to Section 8.2.2 for the measurement setup and procedures, Figure D.3 for a visual illustration and Table D.3 for a comprehensive list of input parameters.

D.1 BGL experiment software

The web interface developed for the BGL measurements deals with the data acquisition, component control and real time solar simulations. A feature incorporating lunar simulations was not implemented due to the additional computational burden introduced by the computation of accurate lunar spectra. The interface prohibits the user from initiating a measurement until all necessary inputs are given for a successful execution of the measurement. A summary of all input parameters and their respective impacts is given in Table D.1.

The measured count rates, which are returned by the time tagger integrated over the set bin width, can be monitored in real time. This aids in testing the setup prior to actual measurements and identifying potential unexpected behaviour before the data analysis. To address the latter, a failsafe was implemented to prevent high photon fluxes from reaching the SNSPD for a prolonged time, which would heat up the detector. Therefore, the returned count rates are constantly compared to used defined input *Countrate exceeds* threshold. If the threshold is exceeded, the measurement is shut down by changing the optical switch channel to direct all incoming light toward the light trap. It is crucial to ensure that the optical switch channels are connected correctly for this feature to function properly, because the channels are hardcoded in the backend of the web interface (1 $\rightarrow$ SNSPD, 2 $\rightarrow$ light trap). Both channels are labeled on their respective optical fibers.
For a more streamlined measurement procedure, an autosave feature was implemented to prevent data loss, which was later expanded to an automatic measurement feature[1]. Both options can be activated in the interface by toggling the corresponding switch[2]. To use the automatic measurement feature a duration and delay time must be entered. Once started, the measurement is initiated after the specified delay and data is acquired for the defined duration. The data is saved automatically once the duration is reached. All measurements can be conducted with or without the optical switch . When toggling the *Deactivate switch usage?* switch, the channel of the optical switch is fixed to channel one. If enabled, the failsafe remains active, monitoring the count rates and shutting down the measurement if necessary.
The data is saved to *.txt* files, containing a preamble that includes nearly all input parameters and the five columns of data comprising: time in seconds, timestamps in UTC, count rates in Hz, parallel conducted simulations in radiance and the tag indicating the active optical switch channel. These files form the backbone of the BGL analysis. In addition to the measurement files, log files are saved on the PC running the interface, monitoring all changes made since the startup of the software.

[1] The expansion happened after the first presented measurement campaign on the 08.08.2025.
[2] Once the automatic measurement feature is chosen, the autosave option is enabled automatically.

Table D.1: Overview of BGL web interface input parameters. The abbreviations describe how the parameters are used: S = used in the simulation input, E = used for the system efficiency calculation , C = used for the conversion of count rates to radiances, P = used for the calculation of the Sun's position.

Input name	**Default Value**	**Description**	**Used for**
`Channel`	1	Sets the used time tagger channel. Must match channel connected to the SNSPD.	
`Trigger Level [V]`	−0.325 V	Sets the trigger level of the time tagger. Voltage level based on measurement of voltage pulses sent by SNSPD.	
`Dead time [ns]`	12 ns	Sets the dead time of the time tagger.	
`Min datapoints before activation`	10	Limit of how many count rates have to be queried until the active switch channel changes.	
`COM port`	COM3	COM port address under which the switch can be found.	
λ `[nm]`	1565 nm	Center wavelength of the center dichroic mirror.	**S**,**C**
`Beff [nm]`	34.9 nm	Effective bandwidth of the dichroic mirror.	**C**
`Binwidth [ms]`	1000 ms	Defines the integration time of the time tagger. Additionally used as time input for the periodic callbacks for simulation and measurement updates.	

Table D.1: Overview of BGL web interface input parameters.

Input name	Default Value	Description	Used for
`Detector` η	0.85	Fully recovered system detection efficiency provided by the ID Quantique.	**C**
`Receiver ∅ [cm]`	80 cm	Diameter of the receiving aperture of the OGSOP.	**C**
`MFD fiber [`μ`m]`	10.4 µm	Mode field diameter of the optical fiber.	**C**
`EFL [mm]`	3865 mm	Effective focal length of the Coudé bench.	**C**
`Efficiency w/o coupling`	-	System efficiency calculated based on Tele/Coudé train, Coudé table and Fiber to SNSPD.	**C**
`Tele/Coude train [dB]`	−3.8 dB	Losses accumulated from the top of the telescope to the Coudé table. Values taken from previous works [2].	**E**
`SMF coupling [dB]`	-	Measured coupling loss after fiber alignment.	
`Coude table [dB]`	-	Losses up until the fiber coupling as measured during preparations.	**E**
`Fiber to SNSPD [dB]`	-	Losses after fiber coupling until SNSPD input. Measured during preparations.	**E**
`Latitude °N`	48.084 76°	Latitude coordinates of the OGSOP.	**P**

Table D.1: Overview of BGL web interface input parameters.

Input name	**Default Value**	**Description**	**Used for**
`Longitude °N`	11.277 98°	Longitude coordinates of the OGSOP.	**P**
`Altitude [m]`	650 m	Altitude of the OGSOP.	**S**
`Azimuth [°N]`	-	Azimuth pointing angle of the telescope.	**S**
`Elevation [°]`	-	Elevation pointing angle of the telescope.	**S**
`Ground albedo`	0.15	Default based on previous observations in [28].	**S**
`Visibility [km]`	30 km	Visibility changed depending on measurement conditions. Default based on previous observations in [28].	**S**
`Season conditions`	-	Set according to current season. Adjusts the aerosol composition applied in *uvspec*.	**S**
`Haze conditions`	rural	Defines the aerosol composition applied in *uvspec*. Default based on previous observations in [28].	**S**
`Duration [s]`	600 s	Defines the measurement duration after which the software automatically stops. Only active if automatic measurement is used.	
`Data directory`	Custom path	Directory to which log and data files are saved.	

Table D.1: Overview of BGL web interface input parameters.

Input name	Default Value	Description	Used for
`Countrate exceeds [MHz]`	15 MHz	Condition for the measurement to automatically shut down. Prohibits the SNSPD from heating up if too much light is detected.	

Figure D.1: BGL measurement web interface overlay.

D.2 SNSPD calibration software

The web interface developed for the SNSPD calibration manages the data acquisition from both the SNSPD and the power meter, while simultaneously controlling the optical switch and the polarization controller. For the polarization controller and power meter, a backend was developed based on SCPI to control the data readout and configuration of the power meter, as well as the polarization state via the polarization controller. To establish a connection with with the power meter, the drivers must be changed to be compatible with NI-VISA, otherwise, the connection with the power meter cannot be established.
The polarization controller can be operated in three modes via the web interface to adjust the polarization state before or during a calibration measurement. These modes include:

1. Discrete polarization scramble
2. (Partial) Poincaré sphere scan
3. Specific polarization state tracking

The discrete polarization scramble mode utilizes the identical named feature of the employed PSY201 polarization controller. Through rapid changes in the fiber squeezer voltages, the polarization state is changed in a random manner, covering the whole Poincaré Sphere, effectively creating unpolarized light [38]. In the second mode, the interface generates a grid, that either covers the entirety or specific regions of the Poincaré sphere as illustrated in Figure 8.8. The shape of the grid is controlled by the input parameters *Min*,*Max* and *Steps* for polar and azimuth angles respectively. Option three can be utilized to track individual polarization states, which are defined by the three normalized Stokes parameters Q, U and V.
Similarly to the BGL web interface, queried powers and count rates can be monitored in real time to detect irregularities. This web interface executes calibration measurements, either a Poincaré scan or single polarization state measurements, fully automatically. Single polarization state measurements can be repeated with the same settings by activating the *Repeat measurement?* option. The duration of a single measurement depends on the data acquisition rate, which additionally serves as the integration time of the time tagger, the amount of samples for the fully recovered SDE that can be calculated from the data and the amount of data points that is waited before the active optical switch channel is changed. If the Poincaré scan option is enabled, each polarization state is scanned sequentially for the duration specified for a single measurement.
Independent of the measurement configuration, the data is saved in a *.txt* format, containing a preamble that includes all input parameters and the data consisting of four columns:

time in seconds, count rate in Hz, power meter readings in watts and the identifier for the active switch channel. In addition to the data files, log files are saved to a dedicated folder on the PC running the interface recording all modifications to the software since start up.
At the time of the submission of this thesis, the interface automatically calculates the fully recovered SDE using a legacy formula which since has been substituted by the procedure outlined in Section 8.2.

Table D.2: Overview of SNSPD calibration web interface input parameters.

Input name	**Default Value**	**Description**
`Channel`	1	Sets the used time tagger channel. Must match channel connected to the SNSPD.
`Trigger Level [V]`	$-0.325\,\mathrm{V}$	Sets the trigger level of the time tagger. Voltage level based on measurement of voltage pulses sent by SNSPD.
`Dead time [ns]`	$12\,\mathrm{ns}$	Sets the dead time of the time tagger.
`Min datapoints before activation`	10	Limit of how many count rates have to be queried until the active switch channel changes.
`COM port`	COM3	COM port address under which the switch can be found.
`Serial number`	-	Serial number of the connected power meter console. Necessary to automatically connect to the device.
`Path to visa64 dll`	Custom path	Path leading to the visa.dll which is necessary to control the power meter console with the *PyVISA* package.

Table D.2: Overview of SNSPD calibration web interface input parameters.

Input name	Default Value	Description
`Mean & Stdv pwm [nW]`	190 nW & 10 nW	Only active in debug mode. Define the mean and standard deviation values used for a random power draw following a normal distribution.
`Repetition amount`	-	Only active if the repeat measurement switch is enabled. Defines how often a measurement with the current settings is repeated.
`Duration [unit]`	-	Only enabled if the Poincare sphere scan option is enabled. Based on the grid, the data acquisition rate and the amount of samples, the total time for the scan is calculated and depicted in the unit of time chosen in the drop down menu to the right of it.
`Min, Max and Steps`	-	All options are used to generate the grid that is used to scan the (partial) Poincare sphere. The maximum is always included in the grid. For the azimuth angle the values can be varied between 0° to 360° and for the polar angle between 0° to 90°. All values must be given as integer's.

Table D.2: Overview of SNSPD calibration web interface input parameters.

Input name	Default Value	Description
`Shift`	0	Modifies the original grid by subtracting the shift value from each azimuth angle. This enables scans using azimuth angles such as e.g. 350°, 355°, 0°, 5° and 10° by first creating a grid with azimuth angles 0°, 5°, 10°, 15° and 20° and then shifting each angle by 10° afterwards.
`Stokes Q,U,V`	-	Normalized Stokes parameters, used to set an individual polarization state. The chosen stated is tracked continuously once set.
`Data acquisition rate [ms]`	1000 ms	Defines the integration time of the time tagger. Additionally used as time input for the periodic callback of the data acquisition function.
`Amount of samples`	20	Sets the amount of $\eta_{sde,0}$ values that can be calculated from the acquired dataset.
`Measurement time [unit]`	400 s	Output of the measurement time for one polarization state / one repetition for the current settings. Dependent on the amount of samples and data acquisition rate. The time unit is selected via the drop down menu to the right of it.
`Bias voltage [V]`	4.5487	Current bias voltage set for the SNSPD.

Table D.2: Overview of SNSPD calibration web interface input parameters.

Input name	**Default Value**	**Description**
`Wavelength [nm]`	1565 nm	Calibration wavelength, equal to the center wavelength of the BGL measurements. Important for the configuration of the power meter console.
`Beamsplitter relation` γ	-	Factor classifying the relation between the two beamsplitter ports. Measured beforehand in a separate measurement.
`Gamma type`	-	Defines how the γ-factor has been calculated. Either by dividing tap (0.1% port) by signal (99.9% port) or the either way around. Adjusts the formula used in the backend which automatically calculated the η value for the current polarization state at the end of the measurement.
`Data directory`	Custom path	Directory to which log and data files are saved.

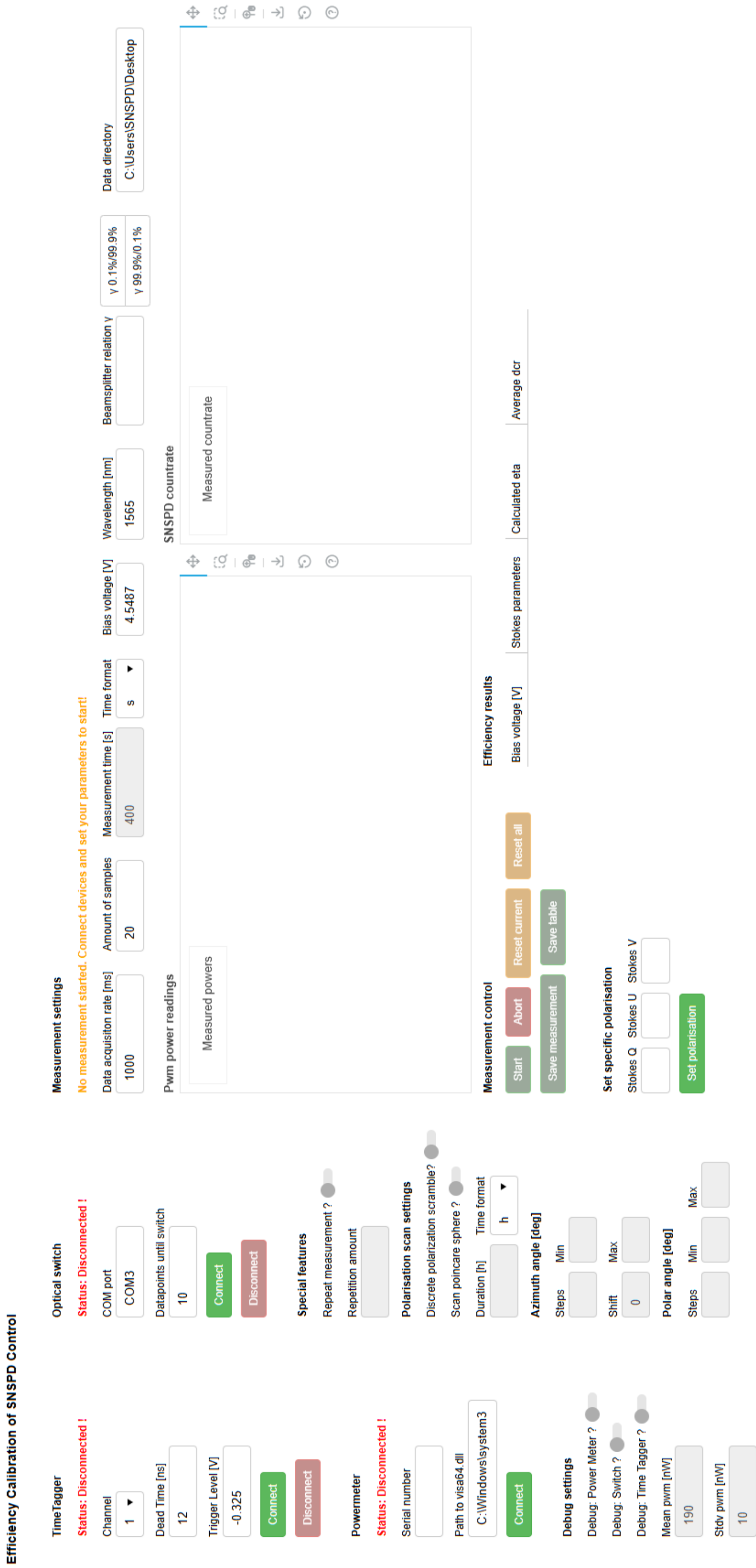

Figure D.2: SNSPD calibration web interface overlay.

D.3 Gamma measurement software

For the calibration of the SNSPD the power relation between the beamsplitter tap and signal ports (γ-factor) must be characterized. Unlike the web interfaces developed for the SNSPD calibration and BGL measurements, this interface is less intricate. To measure the γ-factor, the optical power from two power meters is queried for a set duration. The duration depends on the desired number of samples for γ and the data acquisition rate. The measurement can be repeated automatically if the *Repeat measurement?* option is enabled, which also activates the autosave option. As with the other web interfaces, the data can be monitored in real time, because both the power at both sensors and the calculated γ-factor are streamed directly to the interface.

In principle this interface could be employed for any two-channel setup, where the relative loss between the two optical paths is of interest. Consequently, additional components could be introduced into either optical path as for example necessary for the next iteration of the calibration measurement outlined in Chapter 10. While the software saves all information regarding the used power meters and sensors in the preamble, additional component information must be added manually. The saved data consists of four columns: time in seconds, the power at channel one and channel two in watts and the relation (γ-factor) expressed as the ratio between channel one and channel two. The channels can be distinguished between as the tap and signal ports based on the information entered in the *Channel BS %* inputs of the interface, which is saved in the preamble.

Table D.3: Overview of beamsplitter relation web interface input parameters.

Input name	Default Value	Description
`Repetition amount`	-	Only active if the repeat measurement switch is enabled. Defines how often a measurement with the current settings is repeated.
`Data directory`	Custom path	Directory to which log and data files are saved.

Table D.3: Overview of beamsplitter relation web interface input parameters.

Input name	**Default Value**	**Description**
`Data acquisition rate [ms]`	1000 ms	Defines the integration time of the time tagger. Additionally used as time input for the periodic callback of the data acquisition function.
`Amount of samples`	3600	Sets the amount of γ values that can be calculated from the acquired dataset. Each pair of power values yields one γ value.
`Measurement time [unit]`	3600 s	Output of the measurement time for one repetition for the current settings. Dependent on the amount of samples and data acquisition rate.
`Wavelength [nm]`	1565 nm	Calibration wavelength, equal to the center wavelength of the BGL measurements. Important for the configuration of both power meter consoles.
`Path to visa64 dll`	Custom path	Path leading to the visa.dll which is necessary to control the power meter consoles with the *PyVISA* package.
`Serial number`	-	Serial numbers of the connected power meter consoles. Necessary to automatically connect to the devices.

Table D.3: Overview of beamsplitter relation web interface input parameters.

Input name	**Default Value**	**Description**
`Channel BS %`	-	Defines which power meter is connected to which beamsplitter port. Used for calculation of the overall attenuation in the respective channel.
`Laser power [dBm]`	8.82 dB m	Set laser power. Default value is the minimum power of the used laser. Utilized in the calculation of the overall attenuation in both channels.
`Mean & Stdv pwm [nW]`	-	Only active in debug mode. Define the mean and standard deviation values used for a random power draws following a normal distributions. Individual for both channels.

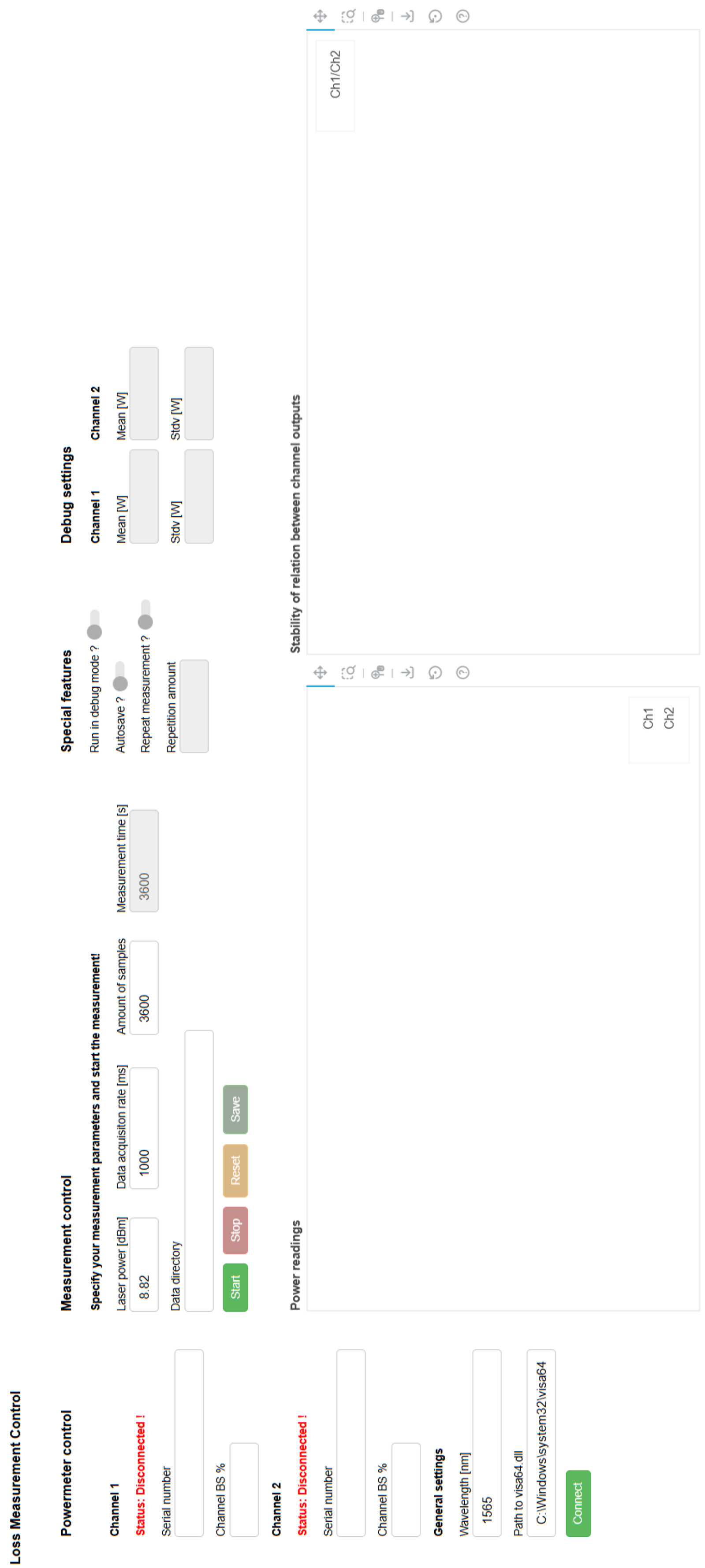

Figure D.3: γ-factor measurement web interface overlay.

Acknowledgments

When I came to Munich in April of 2024 to take a position as a working student at the DLR, I did not expect to stay for two years and finish my master studies here by completing this thesis. I am very grateful for the opportunity to have spent my time researching and working at the DLR.
In no particular order, or in other words in alphabetical order, I want to thank Alex, Amita, Anne-Laure, Davide, Enzo, Joana, Johannes, Jonas and Leonard for being such wonderful colleagues. Everybody supported me in one or another way and some spent some very long nights at the DLR with me, conducting and failing measurements and cursing the weather. At some point I lost count how many hours I spend in the Coudé laboratory and on the roof of the institute to finally reach this point in time where I am writing these lines and the analysis is finished.
A special thanks goes out to Steffi, who was as good of a supervisor someone could wish for. I do not know how I would have finished this thesis without your consistent guidance throughout the whole time at the DLR and your continuous feedback, especially in the last couple of weeks during this thesis. Till this day I never understood how you could keep up with my tremendous amount of talking in Meetings and my special skill to find some “totally necessary„detours regarding my work.
Of course, a special thanks also goes out to those whom need to read through this very short thesis of mine: Florian Moll and Michèle Heurs. I am very grateful that they took on the task of grading this work and my presentation even though Florian is not from my university and Michèle is from a different research background. Thanks for all the great input whenever questions came up. Although I did not seek out advice often, I always felt comfortable doing so.
Persönliche Worte an die Freunde und Familie zu richten ist einfacher in der Muttersprache daher nun einmal der kurze Wechsel. Erstmal muss ich mich bei all meinen Freunden bedanken. Ihr habt alle soviel Hilfe angeboten und habt an meiner Seite gestanden, auch wenn ich euch sehr häfuig geghostet habe, weil mir Hilfe annehmen noch nie leicht fiel und ich diese letzte Hürde des Studiums alleine stemmen wollte.
Ein ganz besonderer Dank geht an meine Eltern, die diese Zeit mit mir durchgestanden haben und sich das ein oder andere mal um mich gesorgt haben, da Ich tagein und tagaus alle Zeit die ich hatte in diese Arbeit gesteckt habe. Ihr habt alle Höhen und Tiefen der letzten Monate mit mir durchlebt und wart mir immer eine emotional Stütze ohne die ich hier nicht so ruhig sitzen und diese Worte verfassen würde.
To everyone from the DLR: Man sieht sich immer zweimal im Leben and I might be back sooner or later. To my parents and friends: All the love in the world.

Literature

[1] Gail P Anderson et al. *AFGL atmospheric constituent profiles (0.120 km)*. Tech. rep. AFGL-TR-86-0110. Air Force Geophys. Lab., Hanscom Air Force Base, Bedford, Mass., 1986.

[2] Tim Bals. “Development and installation of a transmittance monitoring system for the telescope of the optical ground stations Oberpfaffenhofen.” Bachelor Thesis. Munich University of Applied Sciences, Aug. 2025.

[3] John Bardeen et al. “Theory of superconductivity.” In: *Physical review* 108.5 (1957), p. 1175.

[4] G. Bebrov. “On the (relation between) efficiency and secret key rate of QKD.” In: *Scientific Reports* 14.1 (Feb. 2024), p. 3638.

[5] Robert Bedington et al. “Progress in satellite quantum key distribution.” In: *npj Quantum Information* 3.1 (2017), p. 30.

[6] Charles H Bennett and Gilles Brassard. “Experimental quantum cryptography: the dawn of a new era for quantum cryptography: the experimental prototype is working.” In: *ACM Sigact News* 20.4 (1989), pp. 78–80.

[7] Charles H Bennett et al. “Quantum cryptography.” In: *Scientific American* 267.4 (1992), pp. 50–57.

[8] Charles H. Bennett and Gilles Brassard. “Quantum cryptography: Public key distribution and coin tossing.” In: *Theoretical Computer Science* 560 (Dec. 2014), pp. 7–11.

[9] Alexander Berk et al. *Band model method for modeling atmospheric propagation at arbitrarily fine spectral resolution*. US Patent 7,433,806. Oct. 2008.

[10] Alexander Berk et al. “MODTRAN6: a major upgrade of the MODTRAN radiative transfer code.” In: *Algorithms and Technologies for Multispectral, Hyperspectral, and Ultraspectral Imagery XX*. Ed. by Miguel Velez-Reyes and Fred A. Kruse. Vol. 9088. International Society for Optics and Photonics. SPIE, 2014, 90880H.

[11] C Bonato et al. “Feasibility of satellite quantum key distribution.” In: *New Journal of Physics* 11.4 (Apr. 2009), p. 045017.

[12] Thomas Brougham and Daniel K L Oi. “Modelling efficient BB84 with applications for medium-range, terrestrial free-space QKD.” In: *New Journal of Physics* 24.7 (Aug. 2022), p. 075002.

[13] Gabriela Calistro-Rivera et al. *Building Europe’s first space-based Quantum Key Distribution system – The German Aerospace Center’s role in the EAGLE-1 mission.* 2024.

[14] Joseph W Chamberlain. *Physics of the Aurora and Airglow: International Geophysics Series, Vol. 2.* Vol. 2. Elsevier, 2016.

[15] O. M. Coddington et al. “Version 2 of the TSIS-1 Hybrid Solar Reference Spectrum and Extension to the Full Spectrum.” In: *Earth and Space Science* 10.5 (May 2023), e2022EA002637.

[16] T. Lange D. Bernstein. “Post-quantum cryptography.” In: *Nature* 549 (2017), pp. 188–194.

[17] Miloslav Dušek et al. “Quantum cryptography.” In: *Progress in Optics*. Elsevier, 2006, pp. 381–454.

[18] Artur K. Ekert. “Quantum cryptography based on Bell’s theorem.” In: *Phys. Rev. Lett.* 67 (6 Aug. 1991), pp. 661–663.

[19] Hans Elsässer. “The zodiacal light.” In: *Planetary and Space Science* 11.9 (1963), pp. 1015–1033.

[20] C. Emde et al. “The libRadtran software package for radiative transfer calculations (version 2.0.1).” In: *Geoscientific Model Development* 9.5 (2016), pp. 1647–1672.

[21] J Gasteiger et al. “Representative wavelengths absorption parameterization applied to satellite channels and spectral bands.” In: *Journal of Quantitative Spectroscopy and Radiative Transfer* 148 (2014), pp. 99–115.

[22] Dirk Giggenbach and Amita Shrestha. “Atmospheric absorption and scattering impact on optical satellite-ground links.” In: *International Journal of Satellite Communications and Networking* 40.2 (2022), pp. 157–176.

[23] Nicolas Gisin et al. “Quantum cryptography.” In: *Reviews of Modern Physics* 74.1 (Mar. 2002), pp. 145–195.

[24] Lov K Grover. “A fast quantum mechanical algorithm for database search.” In: *Proceedings of the twenty-eighth annual ACM symposium on Theory of computing.* 1996, pp. 212–219.

[25] Mark T. Gruneisen et al. "Adaptive spatial filtering for daytime satellite quantum key distribution." In: *Emerging Technologies in Security and Defence II; and Quantum-Physics-based Information Security III.* Ed. by Keith L. Lewis et al. Vol. 9254. International Society for Optics and Photonics. SPIE, 2014, p. 925404.

[26] Stefanie Häusler et al. *Conversion from photon rate to radiance in SMF coupling systems.* Internal, available to the DLR. Institute of Communciations and Navigations, German Aerospace Center (DLR).

[27] Stefanie Häusler et al. "Evaluation of integration concepts of Optical Ground Stations for satellite-based Quantum Key Distribution into a quantum network." In: *2023 IEEE International Conference on Space Optical Systems and Applications (ICSOS).* 2023, pp. 209–216.

[28] Stefanie Häusler et al. "Measurement-based characterization of atmospheric background light in satellite-to-ground quantum key distribution scenarios." In: *Optical Engineering* 63.4 (2024), p. 041211.

[29] Stefanie Häusler et al. "Measurements of atmospheric background light in the urban area Waterloo and its impact on satellite QKD system performance." In: *Environmental Effects on Light Propagation and Adaptive Systems VII.* Ed. by Karin Stein and Szymon Gladysz. Vol. 13194. International Society for Optics and Photonics. SPIE, 2024, 131940R.

[30] Hugh H Kieffer and Thomas C Stone. "The spectral irradiance of the Moon." In: *The Astronomical Journal* 129.6 (2005), pp. 2887–2901.

[31] Neal Koblitz and Alfred J. Menezes. "A Survey of Public-Key Cryptosystems." In: *SIAM Review* 46.4 (2004), pp. 599–634.

[32] B. Korzh et al. "Provably secure and practical quantum key distribution over 307 km of optical fibre." In: *Nature Photonics* 9.3 (Mar. 2015), pp. 163–168.

[33] Suzanne Lacroix et al. "Modeling of symmetric 2×2 fused-fiber couplers." In: *Appl. Opt.* 33.36 (Dec. 1994), pp. 8361–8369.

[34] Fabian Laudenbach et al. "Continuous-Variable Quantum Key Distribution with Gaussian Modulation—The Theory of Practical Implementations." In: *Advanced Quantum Technologies* 1.1 (2018), p. 1800011.

[35] Yu Li et al. "Microsatellite-based real-time quantum key distribution." In: *Nature* 640.8034 (Apr. 2025), pp. 47–54.

[36] Hoi-Kwong Lo et al. "Decoy State Quantum Key Distribution." In: *Phys. Rev. Lett.* 94 (23 June 2005), p. 230504.

[37] Miao Er-long et al. “Background noise of satellite-to-ground quantum key distribution.” In: *New Journal of Physics* 7.1 (Oct. 2005), p. 215.

[38] Luna Innovations. *PSY-201 User Guide*. Version 1.1. Originally General Photonics, now Luna Innovations. Sept. 9, 2015.

[39] Xiongfeng Ma et al. “Practical decoy state for quantum key distribution.” In: *Phys. Rev. A* 72 (1 July 2005), p. 012326.

[40] B. Mayer and A. Kylling. “Technical note: The libRadtran software package for radiative transfer calculations - description and examples of use.” In: *Atmospheric Chemistry and Physics* 5.7 (2005), pp. 1855–1877.

[41] Bernhard Mayer. “I3RC phase 1 results from the MYSTIC Monte Carlo model.” In: *Intercomparison of three-dimensional radiation codes: Abstracts of the first and second international workshops*. 1999, pp. 49–54.

[42] Bernhard Mayer et al. “libRadtran user’s guide.” In: *Edition for libRadtran version* 2.0.6 (Feb. 2025).

[43] Mayer, B. “Radiative transfer in the cloudy atmosphere.” In: *EPJ Web of Conferences* 1 (2009), pp. 75–99.

[44] Susan K. Meerdink et al. “The ECOSTRESS spectral library version 1.0.” In: *Remote Sensing of Environment* 230 (2019), p. 111196.

[45] Michael I Mishchenko. “Maxwell’s equations, radiative transfer, and coherent backscattering: A general perspective.” In: *Journal of Quantitative Spectroscopy and Radiative Transfer* 101.3 (2006), pp. 540–555.

[46] Michael I Mishchenko. “Multiple scattering, radiative transfer, and weak localization in discrete random media: unified microphysical approach.” In: *Reviews of Geophysics* 46.2 (2008).

[47] Michael I Mishchenko et al. *Scattering, absorption, and emission of light by small particles*. Cambridge university press, 2002.

[48] Katsumi Morishita and Kazunori Yamazaki. “Wavelength and polarization dependences of fused fiber couplers.” In: *Journal of lightwave technology* 29.3 (2010), pp. 330–334.

[49] Chandra M Natarajan et al. “Superconducting nanowire single-photon detectors: physics and applications.” In: *Superconductor Science and Technology* 25.6 (Apr. 2012), p. 063001.

[50] National Institute of Standards and Technology. *Advanced Encryption Standard2 (AES)*. Federal Information Processing Standards Publication FIPS PUB 197. Updated May 9, 2023. U.S. Department of Commerce, 2001.

[51] National Institute of Standards and Technology. *Data Encryption Standard (DES)*. Federal Information Processing Standards Publication FIPS PUB 46-3. Archived. U.S. Department of Commerce, 1999.

[52] Ryan S Park et al. "The JPL planetary and lunar ephemerides DE440 and DE441." In: *The Astronomical Journal* 161.3 (2021), p. 105.

[53] S. Pirandola et al. "Advances in quantum cryptography." In: *Adv. Opt. Photon.* 12.4 (Dec. 2020), pp. 1012–1236.

[54] Johannes Prell et al. "Optical Ground Station Oberpfaffenhofen Next Generation: first satellite link tests with 80 cm telescope and AO system." In: *2023 IEEE International Conference on Space Optical Systems and Applications (ICSOS)*. 2023, pp. 42–48.

[55] Johannes Prell et al. "Preliminary results of optical downlink between QUBE satellite to the upgraded Optical Ground Station Oberpfaffenhofen - experiments towards quantum key distribution." In: *2025 IEEE International Conference on Space Optical Systems and Applications (ICSOS)*. 2025, pp. 1–9.

[56] Timothy M Rambo et al. "Investigating the impact of fast count rates on timing jitter in SNSPDs." In: *Quantum Optics and Photon Counting 2023*. Vol. 12570. SPIE. 2023, pp. 53–58.

[57] R. L. Rivest et al. "A method for obtaining digital signatures and public-key cryptosystems." In: *Commun. ACM* 21.2 (Feb. 1978), pp. 120–126.

[58] G. Roccetti et al. "HAMSTER: Hyperspectral Albedo Maps dataset with high Spatial and TEmporal Resolution." In: *Atmospheric Measurement Techniques* 17.20 (2024), pp. 6025–6046.

[59] Edoardo Rossi et al. *Intermodal quantum key distribution over an 18 km free-space channel with adaptive optics and room-temperature detectors*. 2026.

[60] Lisa Saalbach et al. "Recent advances in single-photon detection towards the short-wave infrared spectral region." In: *Advances in Physics: X* 11.1 (2026), p. 2611978.

[61] Valerio Scarani et al. "The security of practical quantum key distribution." In: *Rev. Mod. Phys.* 81 (3 Sept. 2009), pp. 1301–1350.

[62] Alessia Scriminich et al. “Optimal design and performance evaluation of free-space quantum key distribution systems.” In: *Quantum Science and Technology* 7.4 (Sept. 2022), p. 045029.

[63] Eric Shettle. “Models of aerosols, clouds, and precipitation for atmospheric propagation studies.” In: *AGARD Conf. Proce.* (Feb. 1990).

[64] P.W. Shor. “Algorithms for quantum computation: discrete logarithms and factoring.” In: *Proceedings 35th Annual Symposium on Foundations of Computer Science.* 1994, pp. 124–134.

[65] Valéria L. da Silva et al. “Continuous vs. Discrete Variables in QKD.” In: *2025 SBMO/IEEE MTT-S International Microwave and Optoelectronics Conference (IMOC).* 2025, pp. 372–376.

[66] C. Liu SK. Liao HL. Yong. “Long-distance free-space quantum key distribution in daylight towards inter-satellite communication.” In: *Nature Photon* 11 (2017), pp. 509–513.

[67] Knut Stamnes et al. *DISORT, a general-purpose Fortran program for discrete-ordinate-method radiative transfer in scattering and emitting layered media: documentation of methodology.* Tech. rep., Dept. of Physics and Engineering Physics, Stevens Institute of Technology, Hoboken, 2000.

[68] Knut Stamnes et al. “Numerically stable algorithm for discrete-ordinate-method radiative transfer in multiple scattering and emitting layered media.” In: *Applied optics* 27.12 (1988), pp. 2502–2509.

[69] Knut Stamnes et al. *Radiative Transfer in the Atmosphere and Ocean.* 2nd ed. Cambridge University Press, 2017.

[70] Lorenzo Stasi et al. “Enhanced detection rate and high photon-number efficiencies with a scalable parallel SNSPD.” In: *ACS Photonics* 12.1 (2024), pp. 320–329.

[71] LR Testardi. “Destruction of superconductivity by laser light.” In: *Physical Review B* 4.7 (1971), p. 2189.

[72] C. Toledano et al. “LIME: Lunar Irradiance Model of ESA, a new tool for absolute radiometric calibration using the Moon.” In: *Atmospheric Chemistry and Physics* 24.6 (2024), pp. 3649–3671.

[73] Leung Tsang and Jin Au Kong. *Scattering of electromagnetic waves: advanced topics.* John Wiley & Sons, 2001.

[74] Leonard Vollmann. *Interleaved SNSPD performance in background light measurement systems*. Internal, available to the DLR. Institute of Communciations and Navigations, German Aerospace Center (DLR).

[75] Shuang Wang et al. "Twin-field quantum key distribution over 830-km fibre." In: *Nature Photonics* 16.2 (Feb. 2022), pp. 154–161.

[76] Xiang-Bin Wang. "Beating the Photon-Number-Splitting Attack in Practical Quantum Cryptography." In: *Phys. Rev. Lett.* 94 (23 June 2005), p. 230503.

[77] Manfred Wendisch and Ping Yang. *Theory of atmospheric radiative transfer: a comprehensive introduction*. John Wiley & Sons, 2012.

[78] Martin E. Hellman Whitfield Diffie. "New Directions in Cryptography." In: *IEEE Transactions on Information Theory* 22.6 (1976).

[79] Zurek W. Wootters W. "A single quantum cannot be cloned." In: *Nature* 299 (1982), pp. 802–803.

[80] J. Zhang et al. "Advances in InGaAs/InP single-photon detector systems for quantum communication." In: *Light: Science & Applications* 4.5 (May 2015), e286.